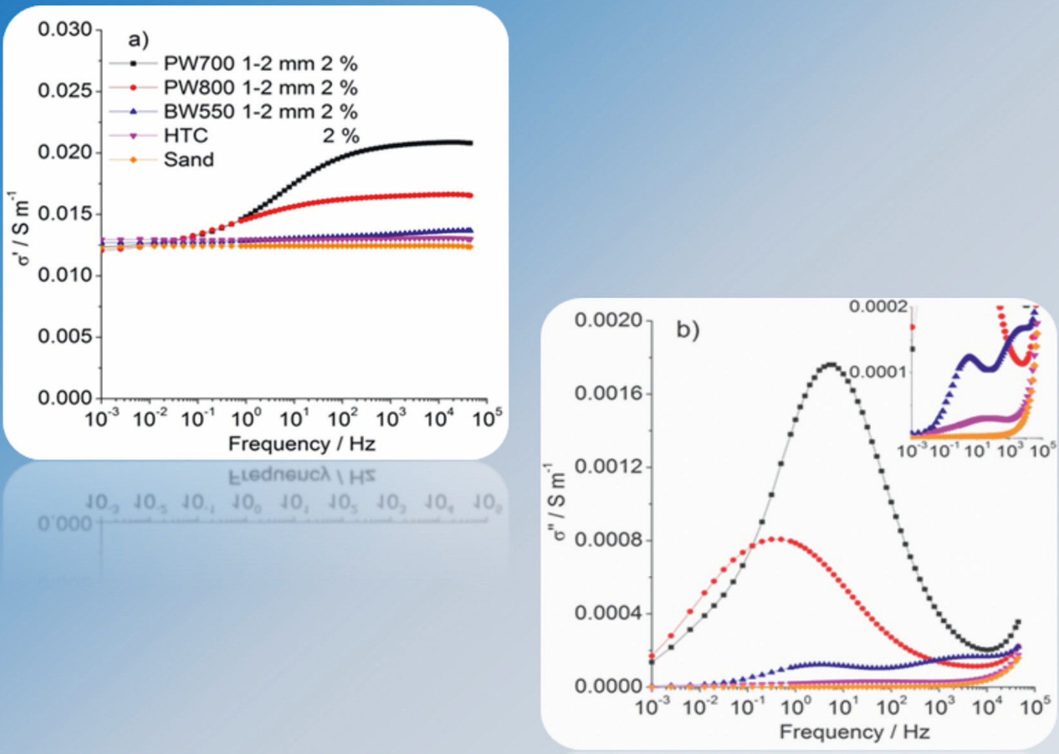

Spectral Induced Polarization of Biochar in Soil

Zhan Gao

Energie & Umwelt / Energy & Environment
Band / Volume 593
ISBN 978-3-95806-662-5

Mitglied der Helmholtz-Gemeinschaft

JÜLICH
Forschungszentrum

Schriften des Forschungszentrums Jülich
Reihe Energie & Umwelt / Energy & Environment   Band / Volume 593

Forschungszentrum Jülich GmbH
Institut für Bio- und Geowissenschaften
Agrosphäre (IBG-3)

Spectral Induced Polarization of Biochar in Soil

Zhan Gao

Schriften des Forschungszentrums Jülich
Reihe Energie & Umwelt / Energy & Environment Band / Volume 593

ISSN 1866-1793 ISBN 978-3-95806-662-5

Bibliografische Information der Deutschen Nationalbibliothek.
Die Deutsche Nationalbibliothek verzeichnet diese Publikation in der
Deutschen Nationalbibliografie; detaillierte Bibliografische Daten
sind im Internet über http://dnb.d-nb.de abrufbar.

Herausgeber und Vertrieb:	Forschungszentrum Jülich GmbH Zentralbibliothek, Verlag 52425 Jülich Tel.: +49 2461 61-5368 Fax: +49 2461 61-6103 zb-publikation@fz-juelich.de www.fz-juelich.de/zb
Umschlaggestaltung:	Grafische Medien, Forschungszentrum Jülich GmbH
Druck:	Grafische Medien, Forschungszentrum Jülich GmbH
Copyright:	Forschungszentrum Jülich 2022

Schriften des Forschungszentrums Jülich
Reihe Energie & Umwelt / Energy & Environment, Band / Volume 593

D 93 (Diss. Stuttgart, Univ., 2022)

ISSN 1866-1793
ISBN 978-3-95806-662-5

Vollständig frei verfügbar über das Publikationsportal des Forschungszentrums Jülich (JuSER)
unter www.fz-juelich.de/zb/openaccess.

Eigenständigkeitserklärung

Hiermit erkläre ich, dass diese Arbeit nur meine Originalarbeit umfasst und dass ich die vorliegende Dissertation "Spectral induced polarization of biochar in soil" unabhängig geschrieben habe. Alle anderen verwendeten Quellen und Materialien wurden im Text entsprechend anerkannt.

Declaration of independent work

I hereby declare that this thesis comprises only my original work and that I have independently written the present dissertation “Spectral induced polarization of biochar in soil”. Due acknowledgement has been made in the text to all the other works and materials that were used.

Zhan Gao

Zhan Gao

Acknowledgements

This PhD work was funded by the China Scholarship Council (CSC) through the program “National construction of high-level university public graduate project”. This project gave me the opportunity to work in the Agrosphere institute (IBG 3) of the Forschungszentrum Jülich as a host institute and at the University of Stuttgart, as the unit granting doctorates.

First, I would like to express my sincere gratitude to my supervisors, Prof. Dr. Johan Alexander (Sander) Huisman and Dr. Franz-Hubert Haegel. Sander has never hesitated to help me with my project and thesis warmly and responsibly. He also helped me to arrange the courses to fulfil the requirements of my doctorate. Sander is very quick-wittedness and has strong knowledge of geophysics and SIP. He always quickly gave me key guidance and advice for my research. Franz helped me a lot with my work and life. He gave the specific guidance for experiments and data analysis, and supported me with his rigorous scholarship, great patience, and solid knowledge of SIP and electrochemistry. He never hesitated to spend time to help me improve and revise the writing of reports, papers, and the thesis. Franz also gave me a lot of private help when I first arrived in Germany, and spent almost every Friday afternoon discussing with me about my work. Both Sander and Franz always encouraged and supported me to overcome problems and to complete this thesis, which was especially challenging towards the end due to COVID-19. This thesis would never have been accomplished without their support.

My sincere gratitude also goes to all members in our research group. I especially thank Odilia Esser who helped me with the experiments for years and Dr. Egon Zimmermann who built the SIP measurement setup and help me a lot to understand the experimental results and the required data analysis. The weekly “SIP meeting” was an important experience in my PhD career. I would also like to thank Prof. Dr. Harry Vereecken who supported me as the director of IBG-3. Harry gave me many valuable suggestions

during the PhD report meetings and in the PhD seminars. With his help and support, many Chinese and overseas students were able to have good working conditions and smooth lives while working at the Forschungszentrum Jülich.

I would like to thank all the people at the Forschungszentrum Jülich and the RWTH Aachen who provided access to additional laboratory equipment to support the characterization of biochar. Carbon Terra GmbH, Pyreg GmbH, Santanu Mukherjee (Forschungszentrum Jülich), Nicolai D. Jablonowski (Forschungszentrum Jülich), Nils Borchard (University of Bonn), and Lutz Breuer (University of Gießen) are thanked for supplying the investigated biochars.

Last but not least, I would like to thank my family and friends for their support and encouragement for all these years.

My father and grandma, may they rest in eternal peace.

Abstract

The use of biochar as a soil amendment attracts increasing research interest. However, the lack of methods to detect and monitor biochar in situ limits the validation of field-scale applications of biochar. Spectral induced polarization (SIP) is a potential tool to characterize biochar in soil. The aim of this thesis is to investigate how the SIP response of soil with biochar depends on both biochar and soil properties using systematic experiments as well as available mechanistic models.

In a first step, the sensitivity of SIP to the presence of biochar in saturated soil was determined. For this, SIP measurements were conducted on four types of biochar (PW700, PW800, BW550 and HTC) in saturated sandy media under various conditions, including the amount and size of biochar as well as different electrolyte properties. The measured SIP data were interpreted by Debye decomposition to obtain values for the peak relaxation time, τ_{peak}, total chargeability, M, and normalised total chargeability, M_n. SIP showed clear and differentiated responses to the presence of all four types of biochars. Biochar PW700 and PW800 showed significantly stronger polarization. M was found to be proportional to the mass fraction of biochars, although relationships varied for each type of biochars. τ_{peak} of samples with biochar increased with increasing biochar particle size. Furthermore, increased electrolyte concentration enhanced M_n for all biochars, although again, the specific response was different for each biochar. In addition, higher electrolyte concentrations decreased τ_{peak} for biochars derived from wood through pyrolysis but did not affect τ_{peak} of biochar derived from miscanthus through hydrothermal carbonisation. It was concluded that the spectral induced polarization response of pyrolytic biochars resembled that of conductors or semiconductors, whereas the SIP response of biochar obtain from hydrothermal carbonisation more closely resembled that of clay.

In a next step, the mechanism of the induced polarization of samples with biochar was investigated using available mechanistic models to describe polarization of samples with electrically conductive inclusions. For this, SIP measurements on sand-biochar mixtures with PW700 and PW800 were considered, and additional measurements with different types of electrolyte considering possible redox reactions at the biochar surface were conducted for PW700. Two mechanistic models were used to describe the SIP response of saturated sand-biochar mixtures. The first model was an electrochemical model considering perfectly conducting particles and the resulting electrical double layer polarization and possible redox reactions at the surface (Wong model). The Wong model was able to provide an adequate fit for samples with biochar PW700, which showed a stronger polarization that was attributed to a presumably larger electrical conductivity of the biochar. A slight influence of redox reactions on the SIP spectra was observed, and these changes were described to some extent by the Wong model. The second model used the paramaters of a fitted Cole-Cole model to describe the effective complex electrical conductivity of samples considering the transport of charge carriers inside semiconductive particles (Revil model), which was able to provide reasonable predictions of the volume fraction of biochar in sand-biochar mixtures and the diffusion coefficient of the charge carriers inside the biochar particles. It was concluded that both models were partially able to describe the SIP response of samples with biochar, which suggests that the polarization mechanism of biochars with strong polarization is similar to the electrode polarization of conductive or semi-conductive particles, but more complicated due to the complex physical and chemical properties of biochar.

In a third and final step, it was investigated how the SIP response of soil with biochar depends on saturation. Both pressure drainage using an multistep-outflow (MSO) approach and evaporative drying were used to desaturate sand-biochar mixtures while making SIP measurements. For the combined SIP-MSO measurements on a sand sample with PW800 biochar, the measured SIP spectra as a function of saturation were interpreted by fitting a Cole-Cole model to obtain M, τ_0 and the Cole-Cole exponent c_{cc}. It was found that the relationship between bulk electrical conductivity and water saturation was nonlinear in a log-log representation. M also showed a nonlinear decrease with desaturation. τ_0 increased and the c_{cc} decreased with decreasing saturation. For the experiments using evaporative drying, a biochar made from pyrolysis of paper mill sludge (PS) was used. Samples with different initial water saturation were prepared and allowed to evaporate while making time-lapse SIP measurements. It was found that the dependence of the real part of the electrical conductivity, $\sigma'(\omega)$ on water saturation was consistent with Archie's law, although the fitted model parameters had an apparent nature only because of changes in the pore water electrical conductivity due to evaporation. The dependence of the imaginary part $\sigma''(\omega)$ on water saturation was roughly linear. The results suggested that the electrical conductivity and the porous nature of biochar play key roles for polarization of biochar under partially saturated conditions. The difference between the SIP response of sand and sand-biochar mixtures in the investigated range of saturation was high enough to inspire confidence that detecting and monitoring biochar amendments in variably saturated field conditions is feasible.

Overall, this thesis provides three key findings that advance the use of the SIP method to investigate soil with biochar amendments. First, the sensitivity of SIP to the presence of disseminated biochar particles in both saturated and unsatureated soil was verified. Second, the available mechanistic SIP models are partially able to describe the SIP response of biochar for a range of conditions. Third, the physical and chemical properties of biochar were essential to understand the SIP response of biochar. Future research should focus on additional laboratory experiments that better represent field applications of biochar to actual soil, as well as field SIP measurements. To make further progress, improved characterization of biochar properties and improved mechanistic models considering the porous nature of conductive particles are required.

Zusammenfassung

Die Verwendung von Biokohle als Bodenverbesserungsmittel stößt auf zunehmendes Forschungsinteresse. Das Fehlen von Methoden zum Nachweis und zum Monotoring von Biokohle in situ schränkt jedoch die Validierung von Anwendungen von Biokohle im Feld ein. Die spektral induzierte Polarisation (SIP) ist ein potenzielles Instrument zur Charakterisierung von Biokohle im Boden. In dieser Arbeit soll untersucht werden, wie die SIP-Antwort von Böden mit Biokohle sowohl von den Biokohle- als auch von den Bodeneigenschaften abhängt, wobei sowohl systematische Experimente als auch verfügbare mechanistische Modelle verwendet werden.

In einem ersten Schritt wurde die Empfindlichkeit des SIP auf das Vorhandensein von Biokohle im gesättigten Boden bestimmt. Zu diesem Zweck wurden SIP-Messungen an vier Arten von Biokohle (PW700, PW800, BW550 und HTC) in gesättigten sandigen Medien unter verschiedenen Bedingungen durchgeführt, einschließlich der Menge und Größe der Biokohle sowie verschiedener Elektrolyteigenschaften. Die gemessenen SIP-Daten wurden durch Debye-Zerlegung interpretiert, um Werte für die Relaxationszeit τ_{peak}, die Gesamtaufladbarkeit M, und die normalisierte Gesamtaufladbarkeit M_n zu erhalten. SIP zeigte klare und differenzierte Antworten auf das Vorhandensein aller vier Arten von Biokohle. Biokohle PW700 und PW800 zeigten eine deutlich stärkere Polarisierung. Es wurde festgestellt, dass sich M proportional zum Massenanteil der Biokohle verhält, obwohl die Beziehungen zwischen den einzelnen Biokohletypen variierten. Der τ_{peak} der Proben mit Biokohle stieg mit zunehmender Partikelgröße der Biokohle. Darüber hinaus führte eine höhere Elektrolytkonzentration bei allen Biokohlen zu einem Anstieg von M_n, obwohl auch

hier die spezifische Reaktion für jede Biokohle unterschiedlich war. Darüber hinaus verringerte eine höhere Elektrolytkonzentration den τ_{peak} von Biokohle, die durch Pyrolyse aus Holz gewonnen wurde, hatte jedoch keinen Einfluss auf den τ_{peak} von Biokohle, die durch hydrothermale Karbonisierung aus Miscanthus gewonnen wurde. Daraus wurde geschlossen, dass die spektral induzierte Polarisationsantwort von pyrolytischen Biokohlen der von Leitern oder Halbleitern ähnelt, während die SIP-Antwort von Biokohle, die durch hydrothermale Karbonisierung gewonnen wurde, eher der von Ton ähnelt.

In einem nächsten Schritt wurde der Mechanismus der induzierten Polarisierung von Proben mit Biokohle unter Verwendung verfügbarer mechanistischer Modelle zur Beschreibung der Polarisierung von Proben mit elektrisch leitenden Einschlüssen untersucht. Dazu wurden SIP-Messungen an Sand-Biokohle-Gemischen mit PW700 und PW800 betrachtet. Für PW700 wurden zusätzliche Messungen mit verschiedenen Arten von Elektrolyten unter Berücksichtigung möglicher Redoxreaktionen an der Biokohleoberfläche durchgeführt. Zwei mechanistische Modelle wurden verwendet, um die SIP-Antwort von gesättigten Sand-Biokohle-Gemischen zu beschreiben. Das erste Modell war ein elektrochemisches Modell, das perfekt leitende Partikel und die daraus resultierende elektrische Doppelschichtpolarisation sowie mögliche Redoxreaktionen an der Oberfläche berücksichtigt (Wong-Modell). Das Wong-Modell war in der Lage, eine adäquate Anpassung für Proben mit Biokohle PW700 zu liefern, die eine stärkere Polarisierung zeigten, was auf eine vermutlich größere elektrische Leitfähigkeit der Biokohle zurückgeführt wurde. Es wurde ein leichter Einfluss von Redoxreaktionen auf die SIP-Spektren beobachtet, und diese Veränderungen wurden bis zu einem gewissen Grad durch das Wong-Modell beschrieben. Das zweite Modell verwendete die Parameter eines angepassten Cole-Cole-Modells zur Beschreibung der effektiven komplexen elektrischen Leitfähigkeit von Proben unter Berücksichtigung des Transports von Ladungsträgern innerhalb halbleitender Partikel (Revil-Modell).

Dieses Modell war in die Lage angemessene Vorhersagen über den Volumenanteil von Biokohle in Sand-Biokohle-Gemischen und den Diffusionskoeffizienten der Ladungsträger innerhalb der Biokohlepartikel zu liefern. Es wurde festgestellt, dass beide Modelle teilweise in der Lage waren, die SIP-Antwort von Proben mit Biokohle zu beschreiben, was darauf hindeutet, dass der Polarisationsmechanismus von Biokohle mit starker Polarisation der Elektrodenpolarisation von leitenden oder halbleitenden Teilchen ähnlich ist, aber aufgrund der komplexen physikalischen und chemischen Eigenschaften von Biokohle komplizierter ist.

In einem dritten und letzten Schritt wurde untersucht, wie die SIP-Antwort von Böden mit Biokohle von der Sättigung abhängt. Zur Entsättigung von Sand-Biokohle-Gemischen während der SIP-Messungen wurden sowohl die Druckentwässerung mit einem Multistep-Outflow-Ansatz (MSO) als auch Trocknung durch Verdunstung verwendet. Für die kombinierten SIP-MSO-Messungen an einer Sandprobe mit PW800-Biokohle wurden die gemessenen SIP-Spektren als Funktion der Sättigung durch Anpassung eines Cole-Cole-Modells interpretiert, um M, τ_0 und den Cole-Cole-Exponenten c_{cc} zu erhalten. Es wurde festgestellt, dass die Beziehung zwischen der elektrischen leitfähigkeit und der Wassersättigung in einer log-logarithmischen Darstellung nichtlinear war. M zeigte ebenfalls eine nichtlineare Abnahme mit der Sättigung. τ_0 nahm zu und der c_{cc} nahm mit abnehmender Sättigung ab. Für die Verdunstungsexperimente wurde eine Biokohle aus der Pyrolyse von Papierfabrikschlamm (PS) verwendet. Es wurden Proben mit unterschiedlicher anfänglicher Wassersättigung hergestellt und verdunsten gelassen, während SIP-Messungen durchgeführt wurden. Es wurde festgestellt, dass die Abhängigkeit der Gesamtleitfähigkeit $\sigma'(\omega)$ von der Wassersättigung mit dem Archie'schen Gesetz übereinstimmt, obwohl die angepassten Modellparameter aufgrund von Änderungen der elektrischen Leitfähigkeit des Porenwassers infolge der Verdunstung einen scheinbaren Charakter hatten. Die Abhängigkeit des Imaginärteils der elektrischen

Leitfähigkeit σ"(ω) von der Wassersättigung war linear. Die Ergebnisse deuten darauf hin, dass die elektrische Leitfähigkeit und die poröse Beschaffenheit von Biokohle eine Schlüsselrolle für die Polarisierung von Biokohle unter ungesättigten Bedingungen spielen. Der Unterschied zwischen der SIP-Antwort von Sand und Sand-Biokohle-Gemischen im untersuchten Sättigungsbereich war groß genug, um die Zuversicht zu wecken, dass der Nachweis und das Monitoring von Biokohlezusätzen unter variabel gesättigten Feldbedingungen machbar ist.

Insgesamt liefert diese Arbeit drei wichtige Erkenntnisse, die den Einsatz der SIP-Methode zur Untersuchung von Böden mit Biokohlezusätzen fördern. Erstens wurde die Empfindlichkeit des SIP auf das Vorhandensein von Biokohlepartikeln sowohl in gesättigten als auch in ungesättigten Böden bestätigt. Zweitens sind die verfügbaren mechanistischen SIP-Modelle teilweise in der Lage, die SIP-Antwort von Biokohle für eine Reihe von Bedingungen zu beschreiben. Drittens waren die physikalischen und chemischen Eigenschaften von Biokohle entscheidend für das Verständnis der SIP-Antwort von Böden mit Biokohle. Künftige Forschungsarbeiten sollten sich auf zusätzliche Laborexperimente konzentrieren, die die Anwendung von Biokohle im Feld besser darstellen, sowie auf SIP-Messungen im Feld. Um weitere Fortschritte zu erzielen, sind eine verbesserte Charakterisierung der Biokohleeigenschaften und verbesserte mechanistische Modelle erforderlich, die die poröse Natur der leitfähigen Partikel berücksichtigen.

Contents

List of figures

List of tables

List of abbreviations

IP	induced polarization
SIP	spectral induced polarization
DC	direct current
AC	alternating current
EDL	electrical double layer
RTD	relaxation time distribution
PNP	Poisson-Nernst-Planck
DD	Debye decomposition
PPIP	perfectly-polarized-interfacial-polarization
PMMA	polymethyl methacrylate
MSO	multi-step-outflow

Chapter 1. Introduction

1.1 General motivation

Biochar has received increased research interest since the beginning of the 21st century due to its great potential value for agricultural and environmental purposes, such as improving soil quality and crop performance and reducing the greenhouse gas emission (Agegnehu et al., 2017; Amoakwah et al., 2017; Arthur and Ahmed, 2017; Bikbulatova et al., 2018; Butnan et al., 2015; Dong et al., 2013; Gaskin et al., 2008; Głąb et al., 2016; Lehmann et al., 2006; Mohammadi et al., 2016; Nemati et al., 2015; Okimori et al., 2003; Sanroman et al., 2017; Tryon, 1948; Woolf et al., 2010; Zhang et al., 2015). The number of publications on the characterization and application of biochar is rapidly growing. However, there still is a lack of methods for in-situ detection and monitoring of biochar amount and quality, especially at the field scale.

The spectral induced polarization (SIP) method provides a promising way to address the in-situ characterization of biochar. SIP has been widely used in mining exploration in the past decades (Kemna et al., 2012; Nelson and Van Voorhis, 1983; Seigel et al., 2007), and is also increasingly applied in environmental and hydrogeological investigations (Aal et al., 2017; Attwa and Guenther, 2013; Breede et al., 2011; Kemna et al., 2012; Maineult et al., 2018; Placencia-Gomez et al., 2015; Revil et al., 2012a). Haegel et al. (2012) reported that SIP was able to detect the presence of biochar in sand. In this thesis, it will be investigated whether it is possible to use SIP for determining the properties of biochar (e.g. amount, type, physical and chemical parameters) in soil using appropriate models.

1.2 Biochar

1.2.1 What is biochar?

Biochar is a fine-grained or lumpy porous carbon compound, similar in its appearance to charcoal, produced by artificial or natural burning of biomass under oxygen-limited conditions (Sohi, 2009). The interest in biochar was originally sparked by the observation of large amounts of black carbon in numerous soil profiles in the Amazon region. These so called ‘Terra Preta’ soils are dark in color and more fertile than adjacent areas. Terra Preta soils are a product of intentional or accidental burning activities of indigenous people (Sombroek, 1966). Nowadays, modern industrial manufacturing provides several methods to create biochar, including pyrolysis (slow pyrolysis and fast pyrolysis), gasification and hydrothermal decomposition of biomass from a wide variety of sources such as wood (Cheng et al., 2014), green waste (Chan et al., 2007), poultry litter (Chan et al., 2008), agricultural residues (Demirbas et al., 2006) and sewage sludge (Mendez et al., 2012). Although widely used, biochar is a relatively new term and remains ill-defined as it shares the basic physical and chemical properties of charcoals or so-called ‘black carbon’ materials. To differentiate biochar from traditional charcoal or other carbon materials, the International Biochar Initiative (IBI) has emphasized the need for an agricultural or environmental use in the definition of biochar.

The physical and chemical properties of biochar are mainly determined by the source material, i.e., the feedstock (Ippolito et al., 2020). Singh et al. (2010) investigated farm-oriented biochar from five types of feedstock (wood, leaves, papermill sludge, poultry litter, and cow manure) by pyrolysis with temperatures between 400°C and 550°C. The pH values varied from neutral to alkaline for these types of biochar. Biochar derived from wood had a higher total carbon and lower nitrogen and phosphorus content compared with the other types of biochar. Jindo et al. (2014)

reported that biochar obtained from woody materials (apple tree and oak tree) showed relatively higher carbon content and adsorption capacity compared to biochar obtained from rice residues (husk and straw), which in turn showed a higher fraction of SiO_2. In addition, the content of volatiles, hydrogen and oxygen varied considerably for the biochars from different feedstocks in both studies. When considering biochar from a given feedstock, processing conditions such as temperature and residence time are known to affect the elemental composition and the structure of the biochar strongly. An increase in pyrolysis temperature increased the total C content (Jindo et al., 2014; Singh et al., 2010), ash content (Singh et al., 2010), pH (Vithanage et al., 2014), and surface basicity (Singh et al., 2010). Jindo et al. (2014) also suggested that a high pyrolysis temperature yields biochar with better adsorption properties due to the higher surface area and porosity and the more recalcitrant chemical character. However, the amount of biochar from pyrolysis will decrease with increasing temperature due to the increasing loss of mass (Jindo et al., 2014; Kim et al., 2012). Considering these factors affecting biochar properties, Ippolito et al. (2020) suggested that wood-based feedstocks in combination with a high pyrolysis temperature provide biochars with the highest specific surface area and total pore volume.

1.2.2 Applications of biochar

The high porosity and adsorption capacity as well as the relatively recalcitrant nature of most biochars make them potentially valuable soil amendments for improving agricultural production and addressing environmental issues. The use of biochar as a soil amendment is not a new concept. There is a long history of using rice husk charcoal or wood ash to improve agricultural soils (Ogawa and Okimori, 2010). The application of biochar in a farmland system is often expected to increase crop yield. Field studies in both tropical and temperate climates often showed an increase in yield or plant growth after biochar application was used to improve the physical and chemical properties of cropland (Hunt et al., 2010; Xu et al., 2012). Some studies relating biochar application and yield or biomass increase are summarized in Tab. 1-1.

Table 1-1. Effects of biochar application on crop yield (Xu et al., 2012)

Biochar rate (t ha^{-1})	Crop	Soil type	Fertilizer rate (kg ha^{-1})	Yield/biomass increase over control (%)
0.5	Moong	Dehli soil	-	+22
100	Radish	Alfisol	N(100)	+266
15	Maize	Sandy soil	N(60), P(26), K(50)	+150
30	Rice	Inceptisol	-	+294
88	Rice	Oxisol	N(40), P(20), K(20)	-21
40	Rice	Paddy soil	-	+14
40	Rice	Paddy soil	N(300)	+19
20	Maize	Oxisol	N(156-170), P(30-43), K(84-138)	+28 (1st year) +30 (2nd year) +140 (4th year)
20% (w/w)	Lettuce	Volcanic soil	-	-73
20% (w/w)	Corn	Volcanic soil	-	-39

By reviewing a considerable number of papers, Sohi et al (2009) summarized three main mechanisms how the application of biochar can provide agronomic benefits: i) direct modification of soil chemistry through intrinsic elemental and compositional makeup of biochar; (ii) providing chemically active surfaces that modify the dynamics of soil nutrients or otherwise catalyze beneficial soil reactions; (iii) modifying the physical character of the soil in a way that benefits root growth or improves nutrient and water retention and acquisition. In addition, biochar can be beneficial to soil microbiology by providing refugia for mycorrhizal fungi and other micro-organisms, which may improve the availability of nutritional cations and anions for plants (Lehmann et al., 2011).

Besides agronomical benefits, biochar may also be used for environmental purposes, such as greenhouse gas mitigation and pollution prevention. Because of its stabilized recalcitrant aromatic structure, biochar seems to be a promising option for long-term sequestration of carbon to offset anthropogenic CO_2 emissions (Dong et al., 2013;

Mohammadi et al., 2016). Research on Terra Preta soils in the Amazon Basin and naturally occurring biochar from forest and grassland fires suggest that biochar can persist for millennia with very little decay (Sombroek, 1966). Because of their highly porous structure, biochar is also able to absorb other greenhouse gasses, such as methane and nitrous oxide (Woolf et al., 2010). Finally, the addition of biochar may also enhance the accumulation of natural soil organic carbon (Borchard et al., 2014). Thus, the use of biochar can produce a net benefit in terms of mitigating global warming. Another benefit of biochar is its ability to adsorb and thus immobilize toxic substances in soil, such as antibiotics (Vithanage et al., 2014), pesticide residues (Deng et al., 2014), organic contaminants (Ogbonnaya and Semple, 2013), and heavy metals (Inyang et al., 2015).

1.2.3 Limitations and potential solutions

Although the positive effects of utilizing biochar were often observed, negative effects of biochar amendments have also been reported. Application of biochar has occasionally resulted in the reduction of crop yield (Liu et al., 2017; Van Zwieten et al., 2010; Xu et al., 2012) or has led to environmental pollution attributed to the physical and chemical properties of specific types of biochar (Kuppusamy et al., 2016). For example, Borchard et al. (2014) found that biochar often has an initially high pH (alkalinity) which is beneficial for the improvement of acidic degraded soils. However, plants may suffer from nutrient deficiencies if soil pH becomes too alkaline. A negative effect of wood biochar application for plant uptake of P and N was also observed and attributed to possible phytotoxic effects (Liu et al., 2017). Since biochar cannot easily be removed from soil once applied, it is necessary to carefully assess its sustainable impacts on soil properties, water quality, plant growth, etc. Clearly, the potential long-term environmental risks of biochar application are still being discussed (Lehmann et al., 2011; Ogbonnaya and Semple, 2013).

Unfortunately, the systematic evaluation of biochar is constrained by limited experimental data, especially for large-scale in-situ measurements and quantitative investigations on the level of stability or rates of degradation of biochar in soil. Previous studies usually focused on a relatively small scale (laboratory or greenhouse), or typically described the effects of a single addition of biochar in the field. Because of the inherently unreactive nature of black carbon, monitoring and characterizing biochar in a straightforward way through classical physico-chemical methods is difficult. Clearly, an effective strategy for monitoring biochar at the field scale in a non-invasive and repeatable manner is urgently required. Ideally, the method should be able to characterize the key parameters of biochar (i.e., type, amount, particle size) and perhaps even interactions between biochar and soil. This would address the demand for improved evaluation of the long-term or temporary performance of biochar in soil. The SIP method shows potential to address this issue.

1.3 Spectra induced polarization (SIP)

1.3.1 Development of the induced polarization method

The induced polarization (IP) method has a long history that extends back to Schlumberger (1915), who reported a possible relationship between subsurface structural information and measured “provoked voltage” during electrical measurements. Schlumberger (1920) later proposed an electrical prospecting method based on the “slow decay phenomenon”, which describes the voltage decay after an injected direct current (DC) passing the subsurface was shut off. Following the patent filed by Schlumberger (1915), the IP method was investigated extensively in USSR between 1920 and 1940 as a tool for geophysical exploration. After the wartime, rapid progress was made in the application of the IP method worldwide, primarily as an exploration tool for mineral deposits of porphyry copper, lead-zinc, sulphide-related gold and others (Seigel, et al. 2007). IP became popular and flourished in the 1950s to

1970s as a tool for mineral exploration. In the past two decades, it has been widely investigated further for near-surface applications, often in an environmental context (Kemna et al., 2012).

The IP method extends the traditional DC method by making an additional measurement of the chargeability of the subsurface. In their influential recommendation for the method, Ward et al. (1995) introduced a framework for the IP method, including information on applicable earth materials, environmental issues, data acquisition and processing, modeling and field demonstrations. The IP method is based on the IP phenomenon which is caused by charge transport and accumulation in near-surface soils and rocks. In geoelectrical practice, IP can be studied in two ways. The measurement of the decaying potential difference as a function of time after current injection is known as time domain IP (TDIP). Alternatively, the effect of alternating currents on the amplitude and phase shift of the resulting potential can be determined, which is referred to as frequency domain IP (FDIP). If a wide range of frequencies is used for FDIP measurements, this is commonly referred to as the spectra induced polarization (SIP) method. Derived from the variable-frequency IP method can be considered as the prototype of spectral IP, the SIP measurement is interesting because of the observed frequency-dependency of the apparent complex conductivity/resistivity of rock materials, which can be very pronounced for mineralized porous media (Wait, 1959). SIP measurements can also be made in the field (Luo and Zhang, 1998). In the past two decades, the equipment for making measurements at multiple frequencies has strongly improved, which spurred the wider use of the SIP method (Kemna et al., 2012). Nowadays, measurements with a high spectral resolution are made in the mHz to kHz frequency range instead of at a single or a limited number of frequencies. More details about the historical development of the IP method can be obtained from Seigel et al. (2007), who provide an overview of the influential researchers and their achievements in the early stages of the IP method.

Kemna et al. (2012) later reviewed recent theoretical research and practical applications of SIP.

1.3.2 SIP for biochar investigations

The potential of SIP for detecting and monitoring biochar in soil was shown by previous studies presenting SIP and TDIP measurements on biochar or other porous black carbon materials. For example, Haegel et al. (2012) observed that the SIP response of sand with additions of different pyrolytic biochars or active carbon depended on the feed material and the pyrolysis process. Gurin et al. (2015) made TDIP measurements on disseminated particles of porous artificial graphite and other electronically conductive minerals in sand. In addition, SIP is known to be sensitive to soil hydrological properties, soil microorganism and soil chemistry (Breede et al., 2011; Personna et al., 2008). Therefore, SIP may provide a way to monitor the applied biochar in soil as well as the associated short-lived and long-term effects on soil properties. To achieve this goal, systematic experimental investigations of different types of biochar in a soil matrix are required. In addition, the understanding of the induced polarization of biochar and the relationship between the SIP response and specific biochar properties needs to be improved.

1.4 Aims and structure of this thesis

The overall aim of this thesis is to investigate how the SIP response of soil with biochar depends on both biochar and soil properties using systematic experiments as well as available mechanistic models. To this end, three specific sub-objectives are defined: (1) determine the sensitivity of SIP to the presence of different types of disseminated biochar in saturated sand under various conditions, including the amount and size of biochar as well as different electrolyte properties; (2) to investigate whether available mechanistic models of induced polarization can be used to understand the relationship between biochar properties and the SIP response; and (3) to investigate how the SIP response of soil with biochar depends on saturation.

The remainder of this thesis is organized as follows. Chapter 2 will review the theory of SIP with a focus on the available modeling methods for conductive particles in a non-conductive background. First, the SIP measurement principles and theory of the electrical double layer (EDL) will be introduced. Thereafter, a comprehensive review of models for IP and SIP including empirical, semi-empirical and mechanistic models will be provided. Potentially suitable models for characterizing the induced polarization of biochar in conductive media will be discussed. Chapter 3 will introduce the investigated biochars and the experimental methods and set-ups that will be used throughout the thesis, including sample holder design, sample preparation, and SIP data acquisition and processing. Chapter 4 will address the first sub-objective. For this, SIP measurements using four types of biochar disseminated in saturated sand as a host media will be performed. It will be investigated and discussed how the SIP response depends on the mass fraction and particle size of biochar, as well as the electrical conductivity of the electrolyte. The results will be compared with other well-investigated materials including conductive, semi-conductive and non-conductive materials to elucidate the mechanism of the polarization of biochar. Chapter 5 will address the second sub-objective and investigate the mechanisms behind the polarization of biochar in soil to better understand the relationship between the physico-chemical properties of biochar and the resulting SIP response using the measurements presented in Chapter 4 and the models concepts presented in Chapter 2. Additional SIP measurements will also be conducted to elaborate possible effects of redox reactions at the surface of biochar. Chapter 6 will address the third sub-objective and investigate the ability of the SIP method for the non-invasive detection of biochar in unsaturated soil, which is a prerequisite for field application of SIP measurements. For this, sand-biochar mixtures will be desaturated using both pressure drainage and evaporative drying while making regular SIP measurements. In addition, the influence of biochar on the hydraulic properties of samples will be investigated. The measured SIP response as a function of saturation will be discussed for selected types of biochar. Finally, Chapter 7 summarizes the main outcomes of this thesis and proposes possible future research directions with a focus on achieving field applications of SIP to investigate biochar.

Chapter 2. Theory and models of spectral induced polarization

2.1 Introduction

In this chapter, a basic introduction into spectral induced polarization measurements will be provided first. After this, available models to describe induced polarization will be reviewed. This will include both semi-empirical and mechanistic models for describing the complex electrical conductivity of porous media with and without conductive materials.

2.2 The basics of SIP measurements

The SIP response of a specific material can be expressed by a complex electrical conductivity σ^* (or resistivity ρ^*):

$$\sigma^*(\omega) = 1/\rho^* = \sigma'(\omega) + j\sigma''(\omega) = |\sigma^*|e^{j\varphi} \qquad (2—1)$$

where $\omega = 2\pi f$ (rad s^{-1}) is the angular frequency, f (Hz) is the frequency, $j = \sqrt{-1}$ indicates the imaginary number, σ' and σ'' are the real and imaginary part of the complex electrical conductivity, $|\sigma^*|$ is the magnitude, and $\varphi(\omega)$ (rad) is the phase, which is related to the real and imaginary part of the electrical conductivity according to $\varphi(\omega) = \arctan[\sigma''(\omega) / \sigma'(\omega)]$. These two ways to represent the complex conductivity both have merit and are thus both used in this thesis. In physical terms, σ' represents ohmic conduction and σ'' is a measure for the polarization.

The SIP response of soils can be obtained from in-situ or laboratory measurements of the frequency-dependent apparent complex impedance $Z^*(\omega)$ (Ω) of a material, which can be obtained by applying an alternating current $I^*(\omega)$ (A) while measuring the resulting potentials $V^*(\omega)$ (V) at various points (Wait, 1959) using:

$$Z^*(\omega) = V^*(\omega)/I^*(\omega) \qquad (2—2)$$

A suitable electrode array is required for such impedance measurements. The four-point electrode configuration with two electrodes for current injection and two other electrodes for potential measurements is usually applied to make laboratory and field measurements more efficient and data interpretation easier (Beck, 1981). Two widely used in-situ four-point arrays of electrodes are denoted as the Wenner and the Schlumberger array (Beck, 1981), which are illustrated in Fig. 2-1.

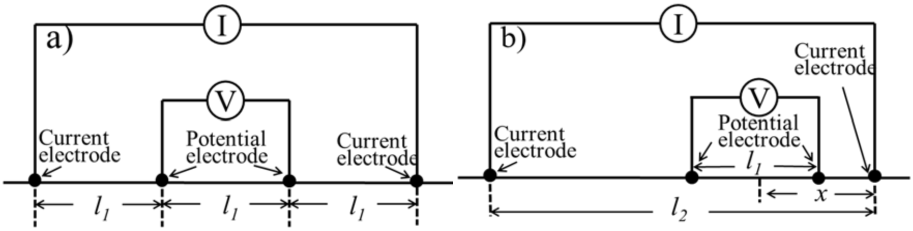

Figure 2-1. Two types of four-point electrode array for SIP measurements: a) Wenner array; l_1 is spacing between each pair of adjacent electrodes. b) Schlumberger array; l_1 and l_2 are the spacing between two potential electrodes and two current electrodes, respectively. x is the distance between one current electrode and the middle point of two potential electrodes.

The Wenner array (Fig. 2-1a) is an assembly of four collinear electrodes with equal spacing l_1 (m). The two outer electrodes are used for injecting the excitation current and the two inner potential electrodes are used for voltage measurements. For this electrode configuration, the apparent complex conductivity $\sigma^*(\omega)$ (S m^{-1}) of a homogeneous subsurface is given by:

$$\sigma^*(\omega) = \frac{1}{2\pi l_1 Z^*(\omega)} \qquad (2—3)$$

The Schlumberger array (Fig. 2-1b) also relies on four collinear electrodes, but variable electrode spacing is used in this electrode configuration. Again, the two outer electrodes are used as current electrodes with a spacing l_2. The two potential electrodes are positioned between the two current electrodes, typically with a considerably smaller spacing l_1. If x is the distance between one current electrode and the middle point of two potential electrodes, the apparent complex conductivity $\sigma^*(\omega)$ for a homogeneous subsurface is given by:

$$\sigma^*(\omega) = \frac{2}{\pi l_1 \, Z^*(\omega)\left[\frac{1}{4(l_2-x)^2 - l_1^2} + \frac{1}{4x^2 - l_1^2}\right]} \qquad (2\text{—}4)$$

Laboratory SIP measurements are important to establish databases relating SIP measurements to subsurface properties, as well as to improve the understanding of the mechanism causing IP phenomena. Vanhala and Soininen (1995) suggested that a laboratory SIP system should have a sufficiently high signal-to-noise ratio in a broad frequency range (usually from 0.01 Hz to 10 kHz). At the same time, the SIP measurements measured in the laboratory should also represent the in-situ properties of the bulk material at the sampling site, which may require large sample sizes. Laboratory SIP measurements are commonly made using prepared samples that are installed and measured in appropriately designed sample holders to obtain the complex electrical conductivity or resistivity.

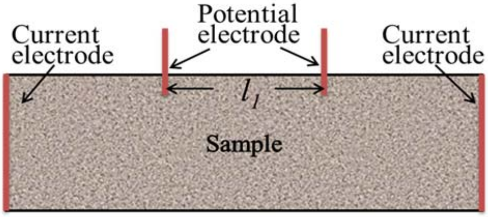

Figure 2-2. Four point laboratorial system. l_1 is the spacing between two potential electrodes

A common four-point laboratory set-up is shown in Fig. 2-2. The two outer electrodes are used to inject the excitation current I^* and the two inner potential electrodes are used to measure the associated voltages V^*. The impedance Z^* can be obtained by Eq. 2-1. For this set-up, the measured complex impedance can be converted to the complex electrical conductivity σ^* by using the appropriate geometrical factor k of the four-point electrode arrangement:

$$\sigma^* = k\frac{1}{Z^*} = \frac{l_1}{A}\cdot\frac{1}{Z^*} \qquad (2—5)$$

where l_1 (m) is the distance between the two potential electrodes, and A (m^2) is the cross-sectional area of the sample.

2.3 The electrical double layer and sources of induced polarization

2.3.1 Electrical double layer (EDL)

The mechanism of the IP phenomenon is closely related to the electrochemical properties of the electrical double layer (EDL). Therefore, a short overview of the theoretical development of EDL descriptions is provided first. Helmholtz (1853) presented pioneering work on the EDL. He reported that a charged electrode immersed in an electrolyte solution attracts a layer of counterions (Helmholtz layer) to its surface by electrostatic force. A wide range of models have been proposed to describe the structure of the EDL. Two important models in the context of IP are the Gouy-Chapman (Gouy, 1910, 1917) and the Stern model (Stern, 1924). The Gouy-Chapman model highlights the diffusive nature of the ionic layer at the electrolyte side and allows predicting the potential distribution over this diffuse layer. Therefore, this diffuse ionic layer is sometimes referred to as Gouy-Chapman diffuse layer. The Stern model divides the EDL into a compact internal layer (Stern layer) of counterions adhering to the electrode surface and an outer diffuse layer. More details about the dynamics and kinetics of ions in the EDL and the possible faradaic charge transfer between electrodes and electrolyte will be discussed in the next section dealing with different types of polarization processes in porous media.

2.3.2 Sources of induced polarization

The IP phenomenon of near-surface porous materials is generally attributed to charge transport and accumulation in micro-heterogeneous structures in an external electric field (Kemna et al., 2012). Although there is considerable debate about the interpretation of IP measurements, researchers commonly attribute the polarization of different porous materials to one or more of five potential sources that are partly related to existing EDL theories, including Stern layer polarization, diffuse layer polarization, membrane polarization, Maxwell-Wagner polarization and electrode polarization.

Stern layer and diffuse layer polarization refer to the deformation and relaxation of the stationary EDL around particles after application of an external electrical field. A colloidal particle immersed in water will develop a charged surface. This charged surface will be associated with a Stern layer of counterions that partially counterbalances the net surface charge density and a diffuse layer of decreasing concentration of counterions and increasing concentration of co-ions towards the electroneutral bulk water. The diffuse layer compensates the surface charge of the particle not compensated by the Stern layer (Leroy et al., 2017). The Stern layer is treated as a monolayer structure of counterions fixed on the surface. It is assumed that the counterions of the Stern layer can only move tangentially along the surface after applying an external field, which induces an electric dipole moment around the particle (Fig. 2-3) (Leroy et al., 2008; Schurr, 1964; Schwarz, 1962). The polarization of the diffuse layer is connected with the relaxation of the electrolyte. The difference in the mobility of co-ions and counterions in the diffuse part of EDL results in concentration gradients at both sides of the particle that lead to polarization(Leroy and Revil, 2009). This process is in accordance with the concept of membrane polarization, which will be elaborated in detail next.

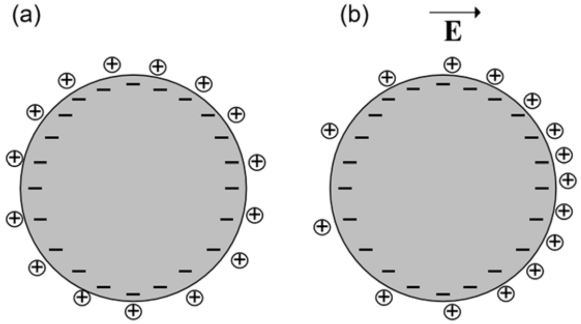

Figure 2-3. Illustration of the (a) static Stern layer and (b) polarized Stern layer under an applied electrical field.

As shown in Fig. 2-4, the double layer around two particles can partially overlap in narrow throats (pores). In the presence of an external electric field from left to right, counterions transport from the left to the right side of the pore is promoted by the high concentration of positive ions because there are mainly counterions (+) in the throat. On the contrary, co-ion transport in the reverse direction is impeded due to the Coulombic repulsion from the surface charge of the particles. Because of the continuity of current, the flow of counterions entering/leaving the domain is the same as the flow of co-ions leaving/entering this side. Since the transfer efficiency of the counterions and co-ions is different in the pore, there is a depletion of counterions on the left side of the pore and an accumulation of co-ions on the right side of the pore. This concentration gradient will drive a back-diffusion through the pore space to partially mitigate the difference in concentration. This process is usually referred to as membrane polarization (Leroy and Revil, 2009; Marshall and Madden, 1959; Revil and Florsch, 2010; Titov et al., 2002; Vinegar and Waxman, 1984).

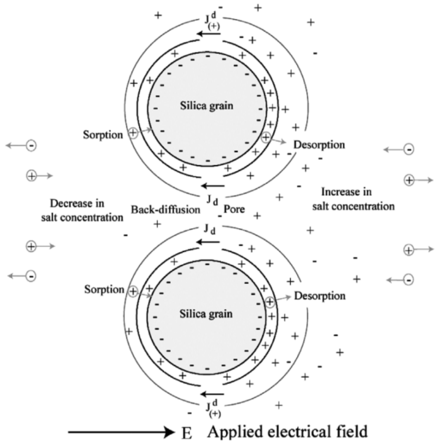

Figure 2-4. Illustration of membrane polarization (Revil and Cosenza, 2010; Revil and Florsch, 2010)

Stern layer polarization, diffuse layer polarization and membrane polarization usually coexist but make different relative contributions to the total polarization in a soil or rock system. Qualitative discussions often highlight three distinct cases depending on the connectivity of the solid phase (Fig. 2-5). In the case of colloidal particles (Fig. 2-5a), Stern layer and diffuse layer polarization are assumed to be the dominant sources of polarization. In granular porous material with a small grain-to-grain contiguity like sandy media (Fig. 2-5b), the overlapping of the electrical diffuse layer at the grain-to-grain contacts (Leroy et al., 2008) results in a so called “continuous diffuse layer” (Revil and Cosenza, 2010), which may reduce the importance of diffuse layer polarization. Instead, Stern layer and membrane polarization are expected to play a more important role. In the case of consolidated rocks with a continuous solid phase without distinct particles (Fig. 2-5c), it is assumed that membrane polarization dominates.

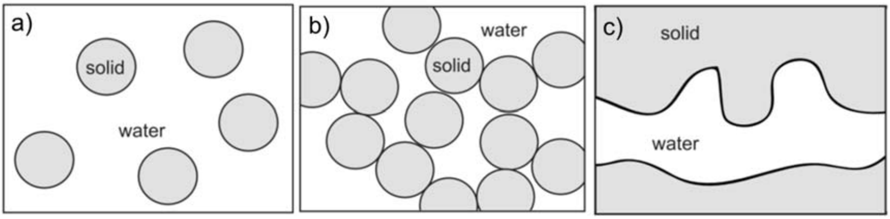

Figure 2-5. Three types of porous materials characterized by different polarization mechanisms. a) Suspended colloidal particle. b) Granular porous medium. c) Porous continuous solid phase (Revil and Cosenza, 2010).

Another source of polarization is Maxwell-Wagner polarization. This source of polarization was first recognized by Maxwell (1873) and further investigated by Wagner (1914), who found that a two-phase system consisting of a homogeneous insulating host material and disseminated conductive spherical particles has a dielectric relaxation spectrum with a single relaxation time. Maxwell-Wagner polarization happens when a current flows across the interface of two media with different electrical conductivity or dielectric permittivity. The charge builds up between the different phases due to the discontinuity of displacement currents. This polarization mechanism can for example can be modeled by the differential effective medium theory at the scale of a representative elementary volume (Bruggeman, 1935; Hanai, 1960; Sen et al., 1981). The importance of this interfacial polarization is highly related to the physical properties of the individual phases and their interface (e.g. roughness, effective shape) and also influenced by the polarization of the Stern and diffuse layer (de Lima and Sharma, 1992; Leroy et al., 2008), while it is independent of particle size and pore size (Lesmes and Morgan, 2001; Wagner, 1914). Maxwell-Wagner polarization is mainly significant in the high frequency range (typically above 1 kHz) and plays a role in the composite mechanistic models for induced polarization of multiphase systems that will be discussed later (Alvarez, 1973; de Lima and Sharma, 1992; Lesmes and Morgan, 2001; Zhdanov, 2008).

For IP measurements in the presence of metal-bearing geomaterials exhibiting high electrical conductivity (e.g. metalliferous ores), the observed relatively strong polarization is often attributed to so-called “electrode polarization”. Although this polarization phenomenon has been extensively and effectively used in exploration geophysics for nearly a century (Haldar, 2018; Kemna et al., 2012; Seigel et al., 2007), studies dealing with the mechanism and modeling of electrode polarization were scarce until 10 years ago. The situation changed with the increased use of SIP and the higher measurement accuracy as well as the increase of computing power (Abdulsamad et al., 2017; Bücker et al., 2018; Gurin et al., 2015; Placencia-Gomez and Slater, 2014; Revil et al., 2015b). It should be emphasized that the “Electrode Polarization” phenomenon discussed in this thesis refers to interfacial polarization of the solid-liquid interface between highly conductive particles (e.g. metallic particle) and the surrounding electrolyte, rather than the net polarization associated with the electrode reactions between the samples and the potential and current electrodes used to make SIP measurements. In fact, the contribution caused by such electrode effects usually needs to be eliminated by the use of four-electrode arrangements, non-polarizing electrodes and model-based corrections (Huisman et al., 2014; Schwan and Ferris, 1968).

The mechanism leading to polarization of a conductive particle is illustrated in Fig. 2-6. Under the influence of an external electric field, charge carriers inside a perfectly conductive particle instantaneously cancel out the electrical field (i.e. no potential difference across the particle). Outside of the particle, the induced charged particle surface affects the ion distribution, which in turn leads to migration currents through the bulk electrolyte. This situation corresponds to an AC excitation or to early times after switching on a constant external field. At sufficiently low frequencies, a new quasi-equilibrium Gouy-Chapman diffuse layer at the particle surface is established. Electrode polarization is usually explained by the semi-infinite diffusion problem over a plane-parallel capacitor. For instance, Wong (1979) described electrode polarization of a conductive particle as a charge-discharge process of a plate capacitor formed by the space charges at each side of the interface.

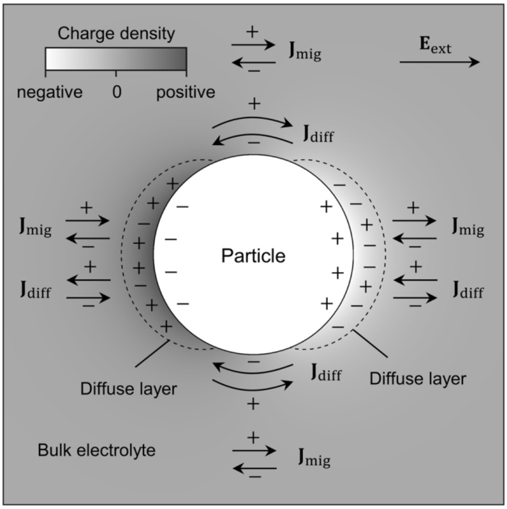

Figure 2-6. Illustration of electrode polarization of a suspended conductive particle in electrolyte (Bücker et al., 2018).

Electrode polarization can be further complicated by possible electrochemical (redox) reactions taking place at the particle interface. For highly conductive materials, such as sulfide ore, redox reactions may occur at the particle surface when in contact with water. These redox reactions create a net exchange current through the interface that counteracts charge accumulation at the interface. Wong (1979) considered this charge transfer as a “leakage current” that makes electrode polarization imperfect, which in turn largely affects the polarization response in both amplitude and phase (Bücker et al., 2018; Placencia-Gomez and Slater, 2014; Wong, 1979).

2.4 Models of induced polarization

The increasing availability of SIP measurements on a wide range of materials and the improved experimental facilities require the development of theoretical models for data interpretation (Kemna et al., 2012). Semi-empirical and mechanistic models have been developed to interpret SIP measurements in a wide range of frequencies using the improved understanding of the dynamics and kinetics of polarizing processes described in the previous sections. They allow extracting useful information of soil properties regarding the type of components, particle size distribution, and other properties from SIP data (Börner et al., 1996; Hördt et al., 2009; Leroy et al., 2008; Lesmes et al., 2000; Slater and Glaser, 2003; Titov et al., 2002; Weller et al., 2011; Weller et al., 2010).

Some widely accepted model approaches to describe the (S)IP response of porous media with conductive particles will be extensively introduced in this section because they are in the focus of this thesis. After this, model concepts to describe the SIP response of porous media without conductive particles will be briefly reviewed for the sake of completeness.

2.4.1 Empirical and semi-empirical models - equivalent circuit approaches

Electrode polarization at the interface of a conductive particle and liquid can be described by an induced semi-infinite diffusion process over a planar electrode as in the case of the Gouy-Chapman model (Bücker et al., 2018; Wong, 1979). Early studies (Gouy, 1910, 1917) showed that the potential decreases as an exponential function of distance from the interface in the diffuse layer with a characteristic length λ_D given by the Debye-Hückel expression (Debye and Hückel, 1923). For a 1:1 electrolyte, this characteristic length is given by:

$$\lambda_D = \sqrt{\varepsilon_r \varepsilon_0 k_B T / 2e^2 \sum n_j} \qquad (2—6)$$

where ε_r and ε_0 are the relative permittivity of the medium and the vaccuum permittivity, k_B is Boltzmann's constant, T is the temperature, e is the fundamental unit of charge and $\sum n_j$ is the particle number concentration of free ions. Because the EDL can be seen as an electrical capacitance associated with the interface, electrode polarization has been described by a combination of resistances and capacitances (sometimes arranged in a rather arbitrary way) in earlier studies (e.g. Macdonald and Johnson, 1987). Based on the idea of a 'polarization capacitance' by Kohlrausch (1873), Warburg (1899) proposed that the impedance of the diffusion layer in response to an alternating electric field $V_0(i\omega)$ can be described as a bulk resistance in series with a frequency-dependent capacitance. The frequency-dependent part of the Warburg model is commonly referred to as the'Warburg impedance element', and is described by:

$$Z(j\omega) = \frac{V(j\omega)}{I(j\omega)} = \frac{V_0}{zFAD^{\frac{1}{2}}c_{ec}}(j\omega)^{-\frac{1}{2}} \qquad (2—7)$$

where V_0 is the effective voltage, z is valency of the ions, F is the Faraday constant, A is the electrode area, c_{ec} is the electrolyte concentration and D is the diffusion coefficient of the ions in the electrolyte. Warburg (1899) argued that this impedance is solely determined by ionic diffusion based on the assumption that charge transfer at the interface (i.e. electrode reactions) is much faster than the electro-migration of the charge carriers to the interface in the electrolyte, so that the impedance could be presented as a constant phase element with an angle of 45°. The Warburg model consisting of a bulk resistance in series with a frequency-dependent capacitance can be expressed as a complex electrical resistivity or conductivity:

$$\rho^*(\omega) = \rho_\infty + \frac{\rho_0 - \rho_\infty}{(j\omega\tau)^{\frac{1}{2}} + 1} \qquad (2—8)$$

$$\sigma^*(\omega) = \sigma_\infty \left(1 - \frac{\sigma_\infty - \sigma_0}{\sigma_\infty} \frac{1}{1 + (j\omega\tau)^{\frac{1}{2}}} \right) \qquad (2—9)$$

where ρ_∞ (σ_∞) and ρ_0 (σ_0) are the asymptotes of resistivity (conductivity) at high and low frequency, respectively, and τ is the relaxation time.

Warburg's work inspired the development of more advanced models to represent EDL polarization with equivalent circuits, such as the Debye model and several variants of modified Warburg-type and Debye-type models in the electrochemistry community. It also prompted more complicated semi-empirical representations of the electrode-electrolyte interface, such as the Cole-Cole model and the Havrilak-Negami model (Ben Ishai et al., 2013). The Debye model was originally proposed for liquids, and describes a dielectric relaxation response of an ideal, noninteracting population of dipoles to an alternating external electric field (Debye, 1929; Debye and Hückel, 1923). The formulations for resistivity and conductivity are given by:

$$\rho^*(\omega) = \rho_\infty + \frac{\rho_0 - \rho_\infty}{j\omega\tau + 1} \tag{2—10}$$

$$\sigma^*(\omega) = \sigma_\infty\left(1 - \frac{\sigma_\infty - \sigma_0}{\sigma_\infty}\frac{1}{1 + j\omega\tau}\right) \tag{2—11}$$

Both Warburg and Debye models are often used in the literature to evaluate SIP measurements. They are special cases of the Cole-Cole model (Cole and Cole, 1941). The formulations for resistivity, conductivity and phase are not equivalent concerning the relaxation time, but yield similar quantities that can be related with each other (Tarasov and Titov, 2013).

The Cole-Cole type model has been found to be a powerful tool to support the interpretation of laboratory and field SIP measurements because it can fit the broadband electrical response of porous media with relatively few parameters. The original formulation of the Cole-Cole model was obtained by empirically fitting a dielectric response function (Cole and Cole, 1941). The formulation for conductivity can be derived from the complex dielectric model as:

$$\sigma^*(\omega) = \sigma_\infty\left(1 - \frac{M_{cc}}{1 + (j\omega\tau_0)^{c_{cc}}}\right) = \sigma_0\left(1 + \frac{M_{cc}}{1 - M_{cc}}\left(1 - \frac{1}{1 + (j\omega\tau_0)^{c_{cc}}}\right)\right) \tag{2—12}$$

where M_{cc} is the total chargeability characterizing the magnitude of polarization given by $M_{cc} = (\sigma_\infty - \sigma_0) / \sigma_\infty$, and c_{cc} is the Cole-Cole exponent which is related to the width of the relaxation time distribution. As shown by Tarasov and Titov (2013), the Cole-Cole model can also be expressed as an equivalent circuit with two conductances and one capacitance in the case of the conductivity formulation (Fig. 2-7).

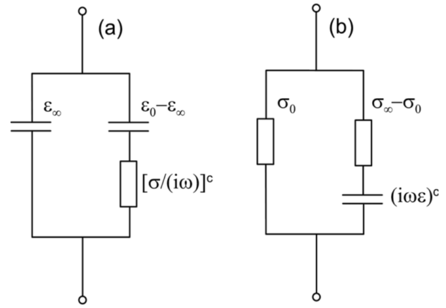

Figure 2-7. Equivalent electrical circuit model for the Cole–Cole equation formulated with (a) dielectric permittivity and (b) electrical conductivity (Tarasov and Titov, 2013).

The Cole-Cole model is commonly considered to be a semi-empirical rather than a purely empirical model because connections have been made between Cole-Cole type spectra and mechanistic models (Tarasov and Titov, 2013) or micro-geometrical or surface chemical properties of the porous media (Lesmes et al., 2000; Revil and Florsch, 2010). When $c_{cc} = 1$, a Debye response is obtained, which corresponds to the Stern layer polarization of a spherical grain with a frequency-dependent surface conductivity (Schwarz, 1962). In the case of $c_{cc} = 0.5$, a Warburg-type spectrum is obtained from the Cole-Cole model. The Cole-Cole parameter τ has been related to the mean and variance of the grain size distribution, and the chargeability *M* has been related to a weighted product of surface area and surface charge density (Lesmes et al., 2000; Weller et al., 2011).

Although many empirical models and equivalent circuits have been proposed and applied to interpret measured SIP data, the limitations of these empirical and semi-empirical methods are obvious. As pointed out by Ben Ishai et al. (2013) and MacDonald (1986), a good fit of the experimental SIP data does not necessarily imply that the fitted relaxation time distribution is the true one because of the equivalence between different formulations of the relaxation distribution with respect to the final SIP response. These limitations of the empirical methods and the increasing need to understand the dynamics and kinetics of polarizing processes in a wide range of frequencies have pushed the development of mechanistic models in the past two decades.

2.4.2 Relaxation time distribution methods

To improve the fitting quality and the flexibility of using empirical and semi-empirical models regarding different shapes of spectra, recent studies have commonly considered a relaxation time distribution (RTD). In these RTD approaches, a SIP spectrum is described by a superposition of a number of individual polarization terms described by a kernel function (i.e. Debye model, Cole-Cole model). Typically, the relaxation time is discretized in regular intervals along the data frequency range. Inversion is then used to obtain the weight of each of the individual kernel functions, which results in a relaxation time distribution (Nordsiek and Weller, 2008; Weigand and Kemna, 2016a; Weigand and Kemna, 2016b; Zisser et al., 2010). In practice, researchers often chose to only fit the real or imaginary part or the phase angle to describe the complex response since the Kramers-Kronig relationships connect the real and imaginary parts of the complex response (Kramers, 1927; Kronig, 1926).

Although the RTD approach typically results in a perfect fit of the SIP measurements, the inversion results and the interpretation of the fitted parameters can be ambiguous because of the dependence on the type of the kernel function (Gurin et al., 2015; Weigand and Kemna, 2016b; Weller et al., 2015a). In addition, the problems of ill-posedness and non-uniqueness of the inversion still require a better assessment of the uncertainty of the inversion results (Weigand and Kemna, 2016a).

2.4.3 Poisson-Nernst-Planck (PNP) theory for perfectly conductive particles

The Poisson-Nernst-Planck (PNP) theory is an applicable theoretical approach to model the electrode polarization process in a conductive media in the presence of metallic particles. In this approach, Poisson's equation describes the mean-field electrostatic potential which is responsible for the electro-migration currents (Schiesser, 2017; Zheng and Wei, 2011), the Nernst-Planck equation is used to describe the electro-diffusion in terms of ion concentration through the whole media without distinguishing between the double layer and the neutral bulk solution. The coupled PNP equations allow to predict both the electric potential profile around a conductive particle and the concentration profiles of each ion species (Abdulsamad et al., 2017; Bücker et al., 2018; Misra et al., 2016; Wong, 1979). Although this approach holds a lot of promise for future work, the solution of the PNP equations for multiple ion species is computationally expensive, which makes it challenging to apply this concept at larger scales with multiple particles (i.e., upscaling). In addition, the definition of appropriate boundary conditions is not straightforward.

2.4.4 The Wong model for perfectly conductive particles

Wong (1979) established an elaborate electrochemical model in combination with electrical potential theory to describe the IP response of porous media with disseminated sulfide ores (referred to as the "Wong model" in this thesis). Based on the Gouy-Chapman model, the Wong model describes the dynamic charging of the field-induced diffuse layer around the surface of a spherical particle associated with the faradaic current through the interface. It also considers the effect of reaction currents at the interface (Angoran, 1977; Klein and Shuey, 1978). Wong and Strangway (1981) later extended the model to consider the effect of a shape factor for non-spherical particles. Bücker et al. (2018) recently reviewed the Wong model based on the full analytical solutions of the PNP equations for a conductive particle.

Three assumptions were used to derive the Wong model. First, the electronically conductive particles (consistently referred to as "metal" particles in Wong (1979)) are assumed to be spherical. Second, the electronically conductive particles are assumed to be randomly dispersed and well separated in the host media so that mutual interactions between the induced dipole moments can be neglected. For this reason, the model is only valid for a volume fraction ν below 0.16. Third, electrical conduction in the non-polarized host media is assumed to be electrolytic and continuous. After an external electric field E is applied, a dipole moment is induced in the electronically conductive particle (see Fig. 2-6). Electrode polarization arises through the reformation of the EDL around the particles. The ions of the electrolyte are divided into two types in the framework of the Wong model: a majority of unreactive (or inactive) species and a minority of active species. Inactive ions (e.g., Na^+, K^+, Cl^-) are not able to be reduced or oxidized at the particle surface. They will be accumulated and depleted at the particle-electrolyte interface under the influence of the alternating electrical field. In contrast, a small quantity of active species (indicated as a metal atom Me and a metal ion Me^+) can participate in the charge transfer across the metal-electrolyte interface if they are reduced or oxidized at the surface. The associated redox reaction can be written as:

$$\mathrm{Me}^{+} + \mathrm{e}^{-} \leftrightarrow \mathrm{Me}_{(\mathrm{ads})} \tag{2—13}$$

This reaction indicates that a metallic ion Me^{+} in the electrolyte accepts an electron e^{-} and becomes a metal atom adsorbed at the metal surface. Obviously, the reverse reaction is also possible. These redox reactions on the surface create a net exchange current density through the interface (faradaic current), which is considered as a leakage current that interferes with the full EDL polarization (Wong, 1979).

The Wong model directly relates the microscopic frequency-dependent induced polarization around a single spherical particle to the macroscopic response by using a mixing model proposed by Maxwell (1873) to obtain the effective complex electrical conductivity σ_e of the conductive porous media containing a volume fraction v_i of disseminated electronically conductive particles. Following Wong (1979), σ_e is given by:

$$\frac{\sigma_e\,(\omega)}{\sigma_0} = \frac{1 + 2\sum v_i\, f(\omega; R_i)}{1 - \sum v_i\, f(\omega; R_i)} \qquad (2—14)$$

where the reflection coefficient $f(\omega)$ is given by:

$$f(j\omega) = 1 + \frac{3\left(1 + \frac{\beta R}{D} f_3\right) + \frac{3c_2}{c_2 - 2c_0}\left(\frac{\alpha}{\mu} - 1\right)}{\frac{c_2}{c_2 - 2c_0}\left[f_1 + \frac{\alpha}{\mu}(f_2 - 2) + \frac{\beta R \lambda_1^2}{D 2\chi^2} + 2\right] - (2 + f_1)\left(1 + \frac{\beta R}{D} f_3\right)}$$

$$(2—15a)$$

with:

$$f_1 = \frac{\lambda_1^2 R^2 + 2\lambda_1 R + 2}{(\lambda_1 R + 1) 2\chi^2} j\omega / D \qquad (2—15b)$$

$$f_2 = \frac{\lambda_1^2 R^2 + 2\lambda_1 R + 2}{(\lambda_1 R + 1)} \qquad (2—15c)$$

$$f_3 = \frac{\lambda_2 R + 1}{\lambda_2^2 R^2 + 2\lambda_2 R + 2} \qquad (2—15d)$$

$$\lambda_1^2 = 2\chi^2 + \frac{j\omega}{D} \qquad (2—15e)$$

$$\lambda_2^2 = \frac{j\omega}{D} \qquad (2-15f)$$

$$2\chi^2 = \sigma_w/(\varepsilon D) \qquad (2-15g)$$

$$\lambda_D = (\sqrt{2}\chi)^{-1} \qquad (2-15\mathrm{h})$$

The key parameters of the Wong model are summarized in Tab. 2-1. In contrast to Wong (1979) where units are based on particle numbers, it is preferred to use units on a molar basis in this thesis.

To illustrate the effect of redox reactions on the predicted SIP spectra, the complex electrical conductivity with and without reactions predicted by the Wong model is shown in Fig. 2-8. The presented simulations consider a porous medium with 8 % volume fraction of conductive particles with a particle size of 2 mm and a moderate electrochemical reaction intensity (c_r = 0.003). It can be seen that the predicted SIP response becomes more dispersive and shows a shift of the phase peak to lower frequency when redox reactions at the particle interface are considered due to the additional leakage currents (Wong, 1979; Placencia-Gomez and Slater, 2014). Wong (1979) also indicated that the predicted SIP response has a Debye type spectrum when there is no reaction taking place, while a Warburg-like spectrum is obtained when considering redox reactions.

Table 2-1. Key parameters of the Wong model

Symbol	Description	Unit
α	electrochemical reaction parameter associated with the migration of active ions under the influence of an extra electric field	A s^2 kg $^{-1}$ mol^{-1}
β	electrochemical reaction parameter associated with the diffusive perturbation of the concentration of active ions	m mol^{-1} s^{-1}
c_2	concentrations of active ions	mol m^{-3}
c_0	total concentration of ions	mol m^{-3}
c_r	ratio of c_2/c_0, represents the fraction of active ions	
D	diffusivity of ions	m^2 s^{-1}
ε	dielectric permittivity	F m^{-1}
ω	angular frequency	
R	particle radius	m
R_i	particle radius related to fraction i of a distribution	m
v_i	volume fraction of conductive particles with radius a_i	
v_w	volume fraction of conductive particles (= $\sum v_i$)	
σ_e	complex electrical conductivity of the sample	S m^{-1}
σ_w	electrical conductivity of the electrolyte	S m^{-1}
σ_0	DC electrical conductivity of the electrolytic medium	S m^{-1}
μ	mobility of ions	m^2 V^{-1} s^{-1}
λ_D	Debye screening length	m
i_0	equilibrium exchange current density	A m^{-2}

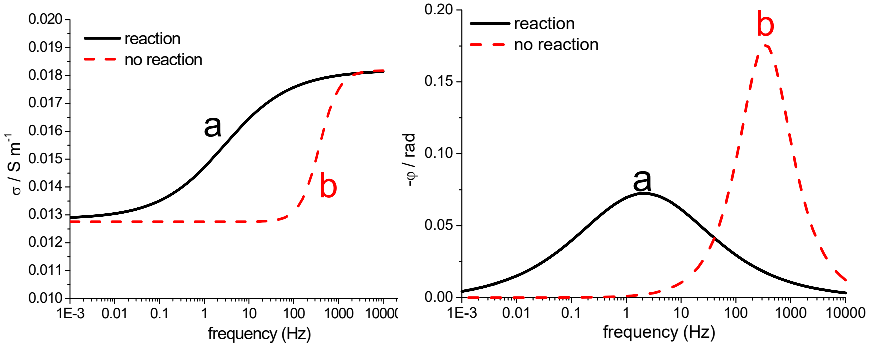

Figure 2-8. Effect of redox reactions on the predicted SIP response by the Wong model. The parameters for the model with redox reactions (curve a) are: $\alpha = 1.8 \times 10^{-7}$ A s^2 kg $^{-1}$ mol^{-1}, $\beta = 0.18$ m mol^{-1} s^{-1}, $c_r = 0.003$, $D = 1.4 \times 10^{-9}$ m^2 s^{-1}, $\varepsilon = 8.9 \times 10^{-11}$ F m^{-1}, and $v = 0.08$. In the case of the model without redox reactions (curve b), the parameters $\alpha = \beta = c_2 = 0$ and all other parameters were left unchanged.

The sensitivity of the SIP response to the parameters of the Wong model has been investigated in several studies (Mahan et al., 1986; Placencia-Gomez and Slater, 2014; Wong, 1979). The general behaviour can be summarized as follows. The maxima of $\varphi(\omega)$ and $\sigma''(\omega)$ increase with an increasing amount of conductive particles, while the peak frequency f_p (also called "critical frequency") remains constant. An increase of the radius of the conductive particles results in a broader dispersion of $\varphi(\omega)$ and $\sigma''(\omega)$, and a shift of f_p to lower frequencies. Placencia-Gomez and Slater (2014) intensively investigated the model sensitivity to electrochemical reactions. They found that an increasing diffusion coefficient of the ions in the EDL and a decreasing fraction of active ions both resulted in a sharper and higher peak of $\varphi(\omega)$ and $\sigma''(\omega)$ as well as a shift of f_p towards higher frequencies.

The analysis of the Wong model presented in Bücker et al. (2018) provided a visualization of the physical processes associated with the polarization around a conductive particle. For small conductive particles as considered in Wong (1979), the polarization response is dominated by the relaxation of the diffuse layer with a relaxation time of $\tau_{dl} = \lambda_D R/2D$. It was observed that the fully developed quasi-equilibrium diffuse layer acts as a screen of the electrical field caused by the field-induced surface charge resulting in a zero-potential zone in the vicinity of the interface at low frequencies. This explains the lower DC conductivity predicted by the Wong model when conductive inclusions are added to a host medium. In a follow-up study (Bücker et al., 2019), it was found that a pre-charged surface (in the absence of an electrical field) will reduce the screening effect of the EDL thereby increasing DC conductivity and relaxation time while decreasing the magnitude of the polarization. Outside the polarized diffusion layer, a visible non-electroneutral zone could also clearly be recognized, especially for the active species. Bücker et al. (2018) attributed this to a volume-diffusion process which leads to a concentration gradient to balance reaction currents through the particle associated with the exchange current at the particle surface. Around a big particle with a radius R that is larger than the critical size $R_c = 8\lambda_D c_r^{-2}$, the volume-diffusion layer can fully develop and its relaxation dominates the polarization of active species. The time constant is dependent on the fraction of the active species:

$$\tau_{\mathrm{vl}} = \frac{R^2}{4D(1-2c_r^{-1})^2} \qquad (2—16)$$

It is interesting to note that the Wong model has rarely been applied in near surface geophysics. To the best of my knowledge, the only application is to infer the oxidative-weathering conditions of mine waste deposits (Placencia-Gomez et al., 2015; Placencia-Gomez et al., 2013). This work showed that the Wong model was suitable to predict the SIP response for minerals including pyrite and pyrrhotite in a relatively low-frequency range (below 100 Hz). Surely the lack of applications is partly due to the complicated mathematical expressions used in this model. It is also clear that the disseminated metalliferous materials commonly investigated by geophysical prospecting methods are usually semiconductors (e.g. pyrite, magnetite and chalcopyrite), which do not fulfill the assumption of a ‘perfect conductor’ in the Wong model.

Recently, several studies reflected on the assumption of infinite conductivity of the metallic particle, and wondered whether models with this assumption allow to interpret measured broadband SIP data on semiconductors (Abdulsamad et al., 2017; Bücker et al., 2019; Misra et al., 2016; Revil et al., 2015b). Bücker et al. (2019) showed that this may be problematic and showed that the argument by Wong (1979) that a ‘perfect conductor’ can be assumed if the conductivity of the mineral is ‘hundred to a thousand times the conductivity of the host medium’, may be appropriate for DC conductivity, but not sufficient in the case of frequency-dependent data.

2.4.5 The Revil model for semi-conductive particles

Revil et al. (2015b) proposed a simplified approach to obtain the effective complex electrical conductivity of samples with disseminated semiconductive particles (referred to as ‘Revil model’ in this thesis). This simplified approach is fundamentally different from the Wong model, which is focused on the transport of ions around the particles. Instead, the Revil model suggests that it is the migration and accumulation of charge carriers inside the particle that dominate the process of induced polarization for semi-conducting particles. The Wong model assumes an instantaneous generation of the dipole moment inside the particle after the electrical field is applied, thus the inside processes have no effect on the relaxation time of the diffuse layer around the particle. This may be a reasonable assumption for a perfect electronic conductor since free electrons as the charge carriers are much faster than the movement of ions in the electrolyte. However, Revil et al. (2015b) suggested that metalliferous minerals (e.g. sulfide ore) that are targeted by (S)IP measurements are usually semiconductors which have a much slower transport of charge carriers (i.e. *p*- and *n*-charge carriers), which may be on a similar time scale as the movement of ions in the electrolyte. The diffusivity of charge carriers inside semiconductors therefore cannot be ignored when studying the polarization of disseminated semiconductors in conductive media. Although pioneering, the Revil model neglects redox reactions at the interface, which are considered by the Wong model.

The Revil model combines the Maxwell-Clausius-Mossotti mixing equation and the Cole-Cole model to provide a simple relation between the parameters of the Cole-Cole model and the properties of a conductive inclusion. In particular, the chargeability is directly related to the volume fraction of the semiconductive particles:

$$M \approx \frac{9}{2}\, \nu \qquad (2\text{—}17)$$

In addition, it is predicted that the relaxation time depends on the grain radius *R* of the spherical conductive particles:

$$\tau_0 = \frac{R^2}{D_m} \tag{2—18}$$

where D_m is the apparent diffusion coefficient of charge carriers in the semi-conductive particle (i.e. p- and n-charge carriers) rather than the diffusion coefficient D of the ions dissolved in the pore-water according to the Wong model. The Revil model was successfully verified by comparing modeling results with a broad database of experimental data (Revil et al., 2015a).

2.4.6 Other models for conductive/semi-conductive materials

Gurin et al. (2015) reported that the Wong model was not able to predict the relaxation time associated with semiconducting particles within a porous medium. They proposed a semi-empirical approach to predict the relaxation time by introducing a volumetric specific capacitance C_{sp} (with dimension of F m^{-3}) as a mineral-specific parameter that depends on mineralogy and surface chemistry:

$$\tau_0 = C_{sp}\frac{R^2}{\sigma_w} \tag{2—19}$$

Following the phenomenological basis of the interfacial polarization given by the Revil model, Misra et al. (2016) proposed a numerical model based on the Poisson-Nernst-Planck equations, referred to as the perfectly polarized interfacial polarization (PPIP) model,. This model integrates the dynamics and distribution of charge carriers inside and outside electrically conductive inclusions. An interesting part of this model is that the extended effective-medium formulations allow considering different shapes of the conductive inclusions, such as spheres, isolated parallel long rods, or thin parallel sheets. The estimated diffusion coefficients of charge carriers in electrically conductive inclusions were found to be similar to that of the p- and n- charge carriers in the inclusion material.

With a polarization concept for semiconductors similar to the Revil model and the model of Misra et al. (2016), Abdulsamad et al. (2017) modeled the dynamic changes in ionic concentration and potential distribution for a single semi-conductive particle suspended in electrolyte under the influence of an electric field using the Poisson-Nernst-Planck equations in the time domain. They considered charge carriers being electrons and holes in the particle and K^+ and Cl^- in the electrolyte. This work provides a visualized result of the system after turning on and turning off the applied external electrical field. As in the Revil model, Misra et al. (2016) and Abdulsamad et al. (2017) both agreed with the basic ideas of the electrode polarization in Wong (1979), but did not take into account possible redox reactions. In the experimental part, Abdulsamad et al. (2017) calculated the specific capacitance C_{sp} proposed by Gurin et al. (2015) for several semi-conducting particles (galena, pyrite, chalcopyrite and graphite) and found that the estimates were lower than the values reported by Gurin et al. (2015) and Hupfer et al. (2016).

2.4.7 Models for porous media with non-conductive particles

Quantitative analysis of the low-frequency polarization of porous media with non-conducting dielectric particles (sand, rock, clay, etc.) usually focuses on describing Stern layer polarization, diffuse layer polarization, or the combination of both. In addition, Maxwell-Wagner polarization typically is also considered, although the effect is typically only apparent in the kHz frequency range. Based on these polarization theories, some models dealing with the effective conductivity of a non-conductive particle will be introduced in the following.

Schwarz (1962) presented a pioneering study dealing with the effective electrical conductivity of spherical particles suspended in electrolyte. He regarded Stern layer polarization as a diffusion-controlled process that can be characterized as a capacitive effect. According to Schwarz's model, the effective complex conductivity, σ^*_{eff}, of a single spherical particle with a radius of R and a fixed ionic atmosphere within an alternating electrical field can be described as the sum of the conductivity of the particle, σ^*_p, and a term which represents the surrounding double layer as:

$$\sigma^*_{eff} = \sigma^*_p + \frac{2}{R}\frac{j\omega\tau}{1+i\omega\tau}e^2\mu_f\Sigma_f \qquad (2—20a)$$

with

$$\tau = \frac{R^2}{2\mu_f k_B T} \qquad (2—20\mathrm{b})$$

where Σ_f is the surface charge carrier density in the fixed layer (m^{-2}), T is absolute temperature (K), e is the elementary charge (A s), μ_f is the mechanical mobility of the counterions in the fixed layer (m s^{-1} N^{-1}), and k_B is the Boltzmann constant (J K^{-1}). This model can typically fit the measured phase shift well, but often fails to describe the DC conductivity because this model only considers fixed or adsorbed counterions in the Stern layer while neglecting the charge transport perpendicular to the double layer. Schurr (1964) extended the Schwarz model by combining it with the work of O'Konski (1960). In this extended model, the EDL was partitioned into two layers. Counterions in an inner layer are tightly bound to the particle surface and can only migrate tangentially along the interface. This inner layer can polarize but does not contribute to the DC conductivity. Around this layer, charges in an outer layer are loosely arranged and can readily exchange with the bulk electrolyte, therefore there is no polarization. However, the charges that move perpendicular to the surface in the outer layer contribute to the DC conductivity. Lesmes and Morgan (2001) indicated that Schurr's model assumes no charge exchange between the outer and inner layer even under the influence of an applied field, which is rather ad hoc. In addition, the amount of charge in each of the layers is hard to measure independently and can only be inferred. By generalizing previous models, Lesmes and Morgan (2001) give the complete electrical response of the fixed layer including the AC polarization of a grain $\sigma_f(AC)$ and its DC surface conductivity $\sigma_f(DC)$ as:

$$\sigma_f = \sigma_f(AC) + \sigma_f(DC) \tag{2—21a}$$

$$\sigma_f(AC) = \frac{\omega^2\tau}{1+\omega^2\tau^2} \times \frac{e^2R\Sigma_f}{kT} \tag{2—21b}$$

$$\sigma_f(DC) = \frac{e^2R\Sigma_f}{kT\tau} \tag{2—21c}$$

Fixman (1980) proposed an approximation of the dielectric relaxation of insulating but charged spheres in aqueous solution based on the Gouy-Chapman model of the EDL. In this model, the charges near the surface are not fixed as in the Schwarz model. Instead, Fixman (1980) assumed that there are continuous diffusive fluxes across the diffuse layer, which dominates the dielectric relaxation. The Stern layer was not considered in Fixman's model, which means that the double layer around the particle is continuous. The effective conductivity of a single sphere derived from Fixman's model is given by de Lima and Sharma (1992):

$$\sigma_{eff} = \frac{\sigma_0 - \sigma_\infty}{1 - 2j\omega\tau/(2+\delta_1)\left[1+(1-i)\sqrt{\omega\tau}\right]} + \sigma_\infty \tag{2—22a}$$

$$\sigma_0 = \frac{2\delta_1\sigma_w}{2+\delta_1} \tag{2—22b}$$

$$\sigma_\infty = \delta_1\sigma_w \tag{2—22c}$$

$$\delta_1 = \Sigma_1/R\Sigma_2 \tag{2—22d}$$

where R is the particle radius (m), n_1 and n_2 are the number densities of the charge carriers in the double layer and the far field electrolyte, Σ_1 is the surface counterion density (m^{-2}) necessary to balance the immobile charges on the particle and Σ_2 (m^{-2}) is the cationic concentration in the electrolyte far from the sphere. With comparable parameters, Fixman's model gives rise to a broader dielectric distribution and a larger relaxation time compared to the Schwarz model. A similar analysis was also presented by Dukhin et al. (1974) and Chew and Sen (1982). In these studies, the relaxation time of a static diffuse layer usually varies as $\tau \propto R^2/2D$.

Composite models that combine the previous theories to consider different possible interfacial and electrochemical polarization processes have also been proposed. For example, de Lima and Sharma (1992) obtained the effective conductivity of water-wet shaly sands and clay bearing rocks by combining the Schurr-Schwarz model for Stern layer polarization and Fixman's model for the diffuse layer polarization with the Maxwell-Wagner mixing model. Based on a comparison with measured data, de Lima and Sharma (1992) suggested that diffuse layer polarization is more appropriate to represent the dielectric behavior of shaly-sandstone materials.

Lesmes and Morgan (2001) proposed a complex conductivity model for saturated sedimentary rocks that considers the particle size distribution and uses the Bruggeman-Hanai-Sen (BHS) effective medium theory (Bruggeman, 1935; Hanai, 1960; Sen et al., 1981) to obtain the effective electrical conductivity. In their approach, the complex dielectric response of a single grain was obtained by directly superimposing the polarization of Stern and diffuse layer. This superposition assumes that the surface conductivity effects in both the fixed and diffuse parts of the EDL are much less than the solution conductivity, which clearly is a strong simplification. Therefore, Lesmes and Morgan (2001) indicated that their model approach represents an upper bound for the total electrochemical polarization because the mutual interaction between the polarizations of both layers was neglected. The relative contribution of the Stern and the diffuse layer to the overall polarization is mainly determined by the relative amounts of charge in each of these two layers. By comparing with measured data on Berea sandstone, it was found that Stern layer polarization dominated the response. Lesmes and Morgan (2001) attributed this to the much larger charge density and the more efficient polarization of the Stern layer. They also indicated that the model should be more sensitive to the particle size rather than the geometrical shape of the particles because both Stern layer and diffuse layer polarization are diffusion-controlled.

More recently proposed composite conductivity models for nonconductive particles basically follow the theories of Stern layer and diffuse layer polarization as in the studies discussed above (de Lima and Sharma, 1992; Lesmes and Morgan, 2001). Based on the Schwarz-Schurr theory, Leroy et al. (2008) proposed a complex conductivity model for porous media consisting of particles of silica considering the surface mineral reactions at the silanol surface sites. The model predicts the surface density of counterions in the Stern layer and both the phase shift and the magnitude of the polarization. Recently, Leroy et al. (2017) generalized their original model and added a screening effect of the polarized diffuse layer on the Stern layer by an effective factor ς (dimensionless). The revised specific conductivity obtained from the surface conductivity of the particles is given by:

$$\sigma_s^*(R,\omega) = \frac{2}{R}\left[\pm\mu_s Q_s\left(\frac{j\omega\tau_s}{1+j\omega\tau_s}\right) + \sum_{i=1}^{N} e z_i B_i^d \Gamma_i^d\right] + j\omega g \rho_s \varepsilon_0 \quad (2\text{—}23\text{a})$$

$$\tau_s = \frac{R^2}{2D_s\varsigma} = \frac{R^2|q|}{2k_B T \mu_s \varsigma} \quad (2\text{—}23\text{b})$$

The results for the upper and the lower frequency limits show that only the diffuse layer contributes to the DC surface conductivity ($\omega \rightarrow 0$), whereas both Stern layer and diffuse layer contribute to the high-frequency conductivity ($\omega \rightarrow \infty$). The key parameters of the model in Leroy et al. (2017) are summarized in Tab. 2-2.

Table 2-2. Key parameters of the model from Leroy et al. (2017)

Symbol	Description	Unit
σ_s^*	complex conductivity of the particle	S m^{-1}
R	particle radius	m
ς (≥ 1)	diffuse layer polarization effects on Stern layer polarization	dimensionless
D_s	surface diffusion coefficient of the counter-ions in the Stern layer	m^2 s^{-1}
μ_s	averaged ion mobility in the Stern layer	m^2 V^{-1} s^{-1}
Q_s	surface charge density of adsorbed ions in the Stern layer	C m^{-2}
τ_s	relaxation time of the polarization of the Stern layer	s
ω	angular frequency	rad s^{-1}
ε_0	dielectric permittivity of the vacuum	F m^{-1}
e	elementary charge of the electron	C
z_i	ion valence	dimensionless
B_i^d	ion effective mobility in the diffuse layer	m^2 V^{-1} s^{-1}
Γ_i^d	Surface site density of adsorbed ions in the diffuse layer	m^{-2}
ρ_s	volumetric density of the particle	kg m^{-3}
g	$g = 0.00191$ empirical constant	m^3 kg^{-1}
k_B	Boltzmann constant	J K^{-1}
T	temperature	K
q	ionic charge in the Stern layer	C

It is important to emphasize here that a prerequisite for the advance of in-depth understanding of IP and the parameterization of data-intensive mechanistic models is the availability of a growing database of SIP measurements on samples considering various physical and chemical parameters. Previous studies have focused on important parameters such as particle size (Leroy et al., 2008; Titov et al., 2002), pore size (Hördt et al., 2016; Titov et al., 2002), fluid salinity (Lesmes and Frye, 2001; Mahan et al., 1986; Slater and Glaser, 2003; Weller et al., 2011), hydraulic conductivity (Börner et al., 1996; Hördt et al., 2009), and surface area per pore volume (Börner et al., 1996; Weller et al., 2010). Additional laboratory and field measurements will promote the understanding of IP and the development of mechanistic models, and this was a strong motivation for the experimental work presented in this thesis.

2.4.8 Induced polarization of pore space and membrane polarization

In contrast to the above mentioned grain-based models which characterize the relaxation by particle size and surface conductivity, pore-based models are related to the pore dimensions and the pore fluid chemistry. By analyzing a broad database of sandstones and unconsolidated sediments, Weller et al. (2010) found a roughly linear relationship between the normalized chargeability m_n or the imaginary conductivity σ'' and the pore-volume-normalized specific surface area per unit mass S_{por} with proportionality coefficients c_s and c_p respectively, which represent a specific polarizability (Weller et al., 2011). S_{por} is calculated by:

$$S_{por} = A_s \cdot \rho_g \cdot (1-\phi)/\phi \qquad (2—24)$$

where A_s is the specific surface area per unit mass (m^2 g^{-1}), ρ_g is the grain density (kg m^{-3}), and ϕ is the porosity of the bulk sample.

Besides, for the dependence of the relaxation time, Revil et al. (2012b) suggested that a relationship of the form $\tau \sim \Lambda^2$ is more appropriate than a relationship of the form $\tau \sim R^2$ for measured Cole-Cole type of spectra on sand and sandstones, where Λ is the dynamic pore radius (m).

The empirical relationships between measured (S)IP spectra and the properties of pores in the absence of metallic materials is frequently discussed with the theory of membrane polarization. Membrane polarization is caused by the ion-selective effects of the EDL in narrow pores, which leads to an excess of mobile cations with respect to the mobile anions and inhibits the flow of anions (Bücker and Hördt, 2013a). Marshall and Madden (1959) proposed an impedance model for a 1-D pore unit consisting of a wide pore with a length L_1 and an interconnected narrow pore with a length L_2 (Fig. 2-9). The ion-selective effect was accounted for by assigning different ion mobilities, μ_1 for a wide pore and μ_2 for a narrow pore ($\mu_1 > \mu_2$). By solving the differential equations corresponding to the above system, Marshall and Madden (1959) obtained a complex frequency-dependent impedance (Marshall-Madden impedance). The forward model shows that a larger chargeability can be obtained with an increase of both the pore length ratio (L_1/L_2) and the mobility ratio (μ_1/μ_2). Based on the assumption of reduced ionic mobility within a Debye length distance from the solid-liquid interface due to the EDL, Volkmann and Klitzsch (2010) proposed numerical models for three types of microscale rocks. extended the Marshall-Madden model by proposing a long and short narrow pore model. This 2-D analytical model is composed of two parts. For a relatively long narrow pore system (LNP) with $L_1/L_2 \leq \mu_1/100\mu_2$, the corresponding model is:

$$Z_{LNP}(\omega) = Z_{DC}\left[1 - M_0\left(1 - \frac{tanh\sqrt{j\omega\tau_1}}{\sqrt{j\omega\tau_1}}\right)\right] \qquad (2-25)$$

while for a short narrow pore system (SNP) with $L_1/L_2 \geq 5\,\mu_1/\mu_2$, the corresponding model is:

$$Z_{SNP}(\omega) = Z_{DC}\left[1 - M_0\left(1 - \frac{1}{1 + \sqrt{j\omega\tau_2}}\right)\right] \qquad (2-26)$$

Where Z_{DC} is the DC resistivity, M_0 is the chargeability, and τ_1 and τ_2 are the time constants. The relaxation times of the LNP and SNP models are proportional to L_1^2 and L_2^2, respectively. These equations imply that the shorter relaxation process via the narrow or the wide pores dominate the relaxation time of the whole system, because the concentration difference at the boundary of wide and narrow pores is built up and balanced mainly through the path with the shorter diffusion time (Bücker and Hördt, 2013b). Hördt et al. (2017) further developed the quantitative model by relating chargeability and relaxation time to pore radius and length directly while also considering geometrical constraints of pores.

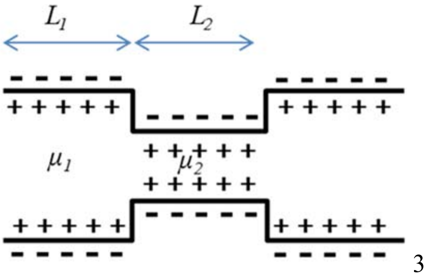

Figure 2-9. Schematic illustration of 1-D pore space model consisting an interconnected wide pore with a length L_1 (m) and ion mobility μ_1 ($\mathrm{m}^2\ \mathrm{V}^{-1}\ \mathrm{s}^{-1}$), and a narrow pore with a length L_2 (m) and ion mobility μ_2 ($\mathrm{m}^2\ \mathrm{V}^{-1}\ \mathrm{s}^{-1}$).

The models described above are able to simulate the basic features of membrane polarization. The realistic pore structure of soil, however, has pore radii with a variety of sizes and geometric connections. Stebner et al. (2017) proposed a network-impedance model to simulate the induced polarization of real porous media. It combines many two-cylinder pore units into a 3-D architecture and uses network parameters that match the porosity and the specific internal surface area of macroscopic porous media.

2.4.9 Discrimination between models for conductive and nonconductive materials

To conclude this chapter, it seems prudent to briefly discuss the potential for confusion when discussing models describing the induced polarization of porous media with and without conductive particles. It is clear that the induced polarization mechanisms around a conductive particle and a nonconductive particle are fundamentally different. However, it may be confusing when one uses terms such as ‘double layer’ or ‘diffuse layer polarization’ which appear when discussing both types of material, or when one uses the theory developed for nonconductive particles to discuss the polarization for conductive particles.

A nonconductive mineral particle immersed in water usually has a fixed negative surface charge because of the chemical reactivity of surface sites (e.g. silica) or by isomorphic substitution (e.g. clay minerals). This constant surface potential results in a steady EDL. After applying an electric field, the rearrangement and relaxation of the EDL (including Stern layer and diffuse layer) are primarily responsible for the polarization in the low-frequency range. In the absence of a fixed surface charge, the existing models for both Stern layer or diffuse layer polarization do not predict any polarization response (Bücker et al., 2019). On the other hand, such a static surface potential is often not considered in the induced polarization process of conductive particles. The conducting particle will always exhibit a surface potential that opposes the applied electrical field. As a consequence, the induced dynamic ion atmosphere (Gouy-Chapman diffuse layer) has the opposite polarity in the vicinity of the two sides of the conductive particle (Fig. 2-4). The dynamic charging of this field-induced diffuse layer is the primary source for induced polarization in the presence of conductive particles. From this summary, it becomes clear that the structure of the double layer and the boundary conditions for conductive and nonconductive particles are different. For this reason, using the same terms for the two different cases may cause confusion. For example, when one uses models considering the “diffuse layer polarization” for minerals or the models based on the Gouy-Chapman diffuse layer for conductive minerals, it should be clear that the former considers the influence of the inner fixed Stern layer of counterions with tangential movement of charges while the latter does not consider this. As also expressed by Bücker et al. (2019), one needs to be cautious whether the effect of nonzero surface charge density is taken into account when one uses theories for nonconductive minerals considering the surface conductivity or the capacitance connected with the polarizing process for conductors.

Chapter 3. Materials and methods

3.1 Introduction

To address the aims of this thesis, SIP measurements will be performed on porous media with biochar. To obtain insight into the induced polarization of biochar in porous media under natural soil conditions, controlled laboratory measurements will be conducted for both saturated and unsaturated samples. In this chapter, information will be provided on the applied sample materials including the investigated biochar types, sand, and electrolytes. In addition, general information about the experimental setups and methods will be provided. However, detailed information about the experimental approaches relevant for individual chapters only will not be provided here.

3.2 Materials

3.2.1 Properties of selected biochars

Five types of biochar from different feedstock and production processes were selected for SIP experiments and physicochemical characterization. Four of them were made by pyrolytic processes (PW700, PW800, BW550, PS). Two were derived from pine wood chips (PW700, PW800), one was derived from beech wood (BW550) and the fourth one was derived from paper mill sludge (PS). One biochar was obtained by hydrothermal carbonization (HTC) of Miscanthus (*Miscanthus x giganteus*). The numbers in the abbreviations above refer to the pyrolysis temperature (in °C).

PW700 was obtained from Carbon Terra GmbH (Augsburg, Germany). The pyrolytic process is characterised by a temperature gradient in a reactor (Schottdorf kiln) from top (input of the feed material) to bottom (output of the biochar). Air is inserted from the bottom leading to gasification at 700 °C in the glowing zone near the output. PW800 was obtained from Pyreg GmbH (Dörth, Germany). It was made by pyrolysis at 800 °C in an auger reactor. PW800 is assumed to have been pyrolyzed in relatively short time leading to an insufficient carbonization. Although no accurate information on the contact time during pyrolysis is available, this hypothesis is supported by the inhomogeneous color and the presence of some residual fragments with woody texture. These woody parts were removed before further analysis (see section 3.2.3). BW550 is a commercial charcoal made by proFagus GmbH (Bodenfelde, Germany) at 550 °C using the Degussa process. PS was provided by Gerhard Soja from the Austrian Institute of Technology. The process parameters used to generate this biochar are not known. HTC was produced by Schlitt GmbH (Antrifttal-Ohmes, Germany) using hydrothermal carbonization at 200 °C.

Some known chemical properties of the biochars are summarised in Tab. 3-1. Element analysis for PW700 and PW800 (three sieved fractions with a particle size range between 0.25 - 0.5 mm, 0.5 - 1 mm and 1 - 2 mm) was performed on a Vario EL cube (Elementar Analysensysteme GmbH, Langenselbold, Germany). The ash content was determined in a muffle furnace at 815 ± 15 °C. Data for BW550 and HTC were taken from the literature as indicated in Table 3-1. BET specific surface areas were determined by nitrogen adsorption with AUTOSORB-1 equipment (Quantachrome Instruments, Boynton Beach, USA). Samples for BET were pre-treated in vacuum at 100 °C for 2 hours to remove volatile compounds that could contaminate the apparatus. Since biochars were made from natural sources, they are heterogeneous. Therefore, it is anticipated that the actual composition and structure of a selected amount of biochar may deviate from the mean values given in Tab. 3-1 by up to 10%.

Table 3-1. Chemical composition and BET surface areas of biochars

Biochar / Size (mm)	C % (w/w)	H % (w/w)	N % (w/w)	O % (w/w)	Ash % (w/w)	H/C (molar)	O/C (molar)	$A_{s(BET)}$ ($m^2 g^{-1}$)
PW700 / 1-2	77.9	1.70	0.623	13.5	9.1	0.26	0.17	185
PW700 / 0.5-1	71.5	1.68	0.703	14.1	15.3	0.28	0.20	172
PW700 / 0.25-0.5	65.7	1.74	0.593	14.3	19.4	0.32	0.22	173
PW800 / 1-2	82.4	1.77	0.400	11.0	4.2	0.26	0.13	181
PW800 / 0.5-1	81.6	1.95	0.350	11.7	4.8	0.29	0.14	174
PW800 / 0.25-0.5	81.6	2.09	0.430	12.4	4.8	0.31	0.15	174
BW550§	87.5	2.63	0.320	9.6	1.6	0.36	0.11	39
HTC$	50.4	5.09	< 0.2	35.9	5.1	1.21	0.71	5.4

§ Data for element and ash content refers to “Charcoal” in Borchard et al. (2014)

$ Data for element and ash content refers to “htcBC5” in Bai et al. (2014)

To convert weight fractions to volumetric fractions, the density of the biochar is required. Considering the porous nature of biochar particles, the required density is the grain or skeletal density (Brewer et al., 2014), which represents the density of the solid part only excluding the open porosity. The grain density of biochar particles was determined by a gas pycnometer (AccuPycTM 1330, Micromeritics, Norcross, USA) and was found to be ~1.80 g cm^{-3} for PW700, PW800 and BW550 and 1.5 g cm^{-3} for HTC.

3.2.2 Sand and electrolyte

All samples were prepared with commercial F36 sand (Quarzwerke Frechen GmbH, Frechen, Germany). It consists of 99.3 % SiO_2. The particle diameter of this sand ranges from 0.125 to 0.250 mm. The grain density was 2.6 g cm^{-3} as given by the manufacturer. The electrolyte solutions were prepared with NaCl, $CaCl_2 \cdot 2H_2O$, $FeSO_4 \cdot 7H_2O$ (all ≥ 99.5% purity, Merck, Darmstadt, Germany) and deionized water.

3.2.3 Pre-treatments before sample preparation

PW700 and PW800 were divided into three size fractions before sample preparation (0.25 - 0.5 mm, 0.5 - 1 mm and 1 - 2 mm). For BW550, a size fraction of 1-2 mm was used. The three fractions for PW700 were obtained by dry sieving of the material as it was obtained. PW800 and BW550 were obtained in larger pieces, which were first crushed and then sieved dry. The internal of PW800 and BW550 were not fully carbonized. Woody fragments were the removed from the crushed pieces. PS and HTC were used as they were obtained. PS had a particle size between 1 and 2 mm, while HTC was a powdery material with unknown size distribution.

Before sample preparation, the investigated biochar and sand were pre-wetted. Biochar particles were immersed in the selected electrolyte solution for 24 hours to fully saturate the inner pores of the biochar particles and to avoid that the biochar particles float on the excess water during sample preparation. The sand was also moistened to a pasty consistence using the selected electrolyte. Mixtures of sand and biochar were homogenized by stirring with a spoon. After these preparatory steps, blank control samples consisting of pure sand or sand-biochar mixtures were prepared. More information on this final step is provided in the relevant chapters.

3.3 SIP measurement setup

3.3.1 Electrical impedance spectrometer

The four-point high-precision electrical impedance spectrometer developed by Zimmermann et al. (2008) was used for all SIP measurements. This system allows measuring the relatively weak phase response of porous sedimentary rocks or soil media in a frequency range between 1 mHz to 45 kHz with a phase accuracy better than 0.1 mrad below 1 kHz. This system comprises a function generator, an amplifier unit, an analog-digital converter (ADC), a PC and a sample holder with four-point-electrode arrangement (see Fig. 3-1). The function generator (Agilent 33120A, Agilent Technologies, Santa Clara, CA) is connected to current electrodes to provide the excitation signal in a frequency range between 1 mHz to 45 kHz with a user-defined voltage range. A voltage range of ± 5 V was used in this study. The amplifier unit was designed to measure the voltages at each of the electrodes. Custom-made triaxial cables were used to connect electrodes and amplifier. An optimized circuit design, operational amplifiers, and an identical construction were used for these the amplifier units to minimize load and cross talk. A signal acquisition card (PCI-4472, National Instruments, US) was used to digitize the voltage signal with 24-bit Sigma-Delta ADCs with digital anti-aliasing filters. LabVIEW and MATLAB programs were developed for controlling the system, data acquisition and post-processing. Correction methods based on an equivalent electrical model were developed and used to improve the complex impedance determination. For more details about this measurement system, the reader is referred to Zimmermann et al. (2008).

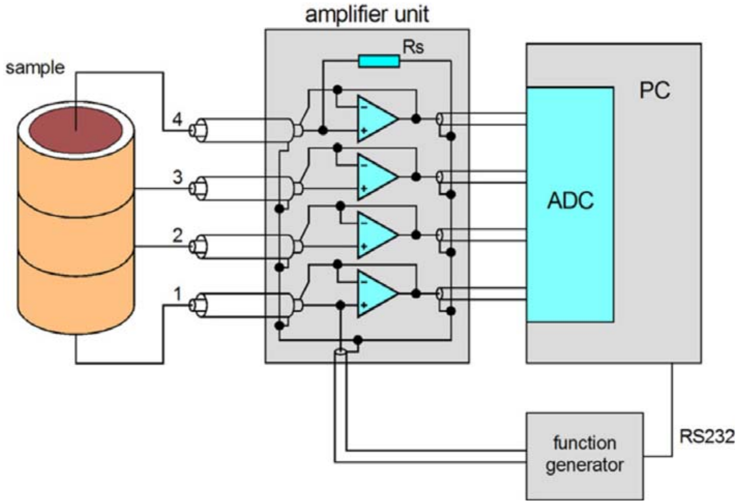

Figure 3-1. Sketch of the four-point measurement system (Zimmermann et al., 2008). Electrodes 1 and 4 are used for current injection and electrodes 2 and 3 are used for voltage measurements

Accurate SIP measurements can only be made with an accurate impedance spectrometer, but an appropriate design of the sample holders and electrode array is equally important. In the following, the three types of sample holders used in this thesis are described in more detail.

3.3.2 Sample holder for SIP measurements on saturated samples

The sample holder used to investigate saturated sand-biochar mixtures is shown in Fig. 3-2. It consists of a cylindrical sample holder with a four-point electrode array combined with a flushing system. The cylindrical sample holder was made of polymethyl methacrylate (PMMA) and was 180 mm long with an inner diameter of 30 mm. Two porous bronze disks with a diameter of 30 mm were placed at the top and the bottom of the cylindrical sample holder and used as current electrodes. Two cylindrical brass potential electrodes with a diameter of 6 mm were inserted in the borings of the side wall of the column at a height of 6 and 12 cm from the bottom of the sample holder. To avoid electrode polarization, the potential electrodes were retracted into the bores by about 2 times the diameter of the potential electrodes (Huisman et al., 2016). The water-filled boring ensures contact between the electrode and the sample. The flushing system consisted of a multi-channel peristaltic pump (Model 205u, Watson-Marlow, Rommerskirchen, Germany) connected with a plastic water tank. The pump was connected to the bottom of the column for injecting aqueous electrolyte from the water tank to the sample holder. Electrolyte was flushed through the samples and the current electrodes from the bottom to the top of the sample.

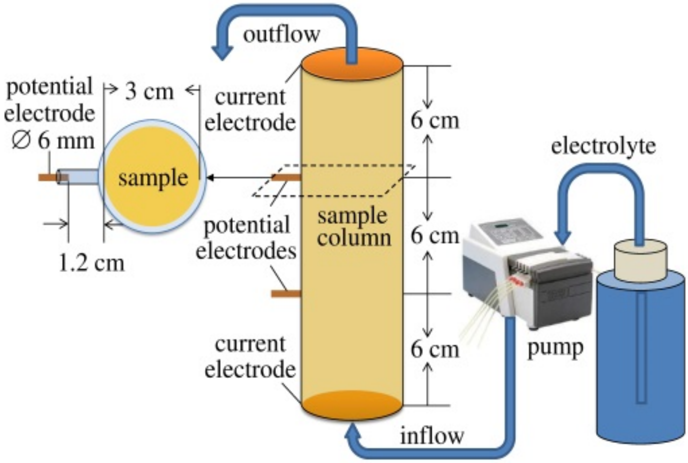

Figure 3-2. Sketch of the saturated experimental setup

3.3.3 Sample holder for SIP measurements during drainage

The measurement setup developed by Breede et al. (2011) for joint SIP and hydraulic measurements was also used in this study (Fig. 3-3). This setup combined a multi-step-outflow (MSO) unit to drain the sample (referred to as "MSO drainage"), and a four-point electrode array for SIP measurements. The sample holder consisted of three connected cylindrical units made of PMMA with an inner diameter of 80 mm. The sample material was contained in the middle cell with 100 mm height and held in position by two porous ceramic plates at the top and bottom of the sample material. Above and below this middle unit, there are water-filled units to increase the SIP measurement accuracy by increasing the distance between the current and potential electrodes (Zimmermann et al., 2008). To drain the sample material, air pressure was applied to the top ceramic plate by means of a tube. The drained water flowed into a burette, where the water height was measured by a pressure sensor and converted to the amount of drained water. If the dry weight of the solid phase at the start or the end of the experiment is known, the amount of drained water can be used to calculate the volumetric water content of the sample at any time. Porous bronze plate electrodes at the top and bottom of the sample holder were used to inject current (see Fig. 3-3). Potentials were measured using two custom-made non-polarizable electrodes consisting of a small tube of PMMA with a diameter of 5 mm and a length of 210 mm with a 1-mm silver wire inside immersed in 4 mM NaCl. One end of these electrodes consisted of a cone-shaped porous ceramic with a high air-entry pressure, which ensures reasonable electrical contact with the sample material even for unsaturated conditions.

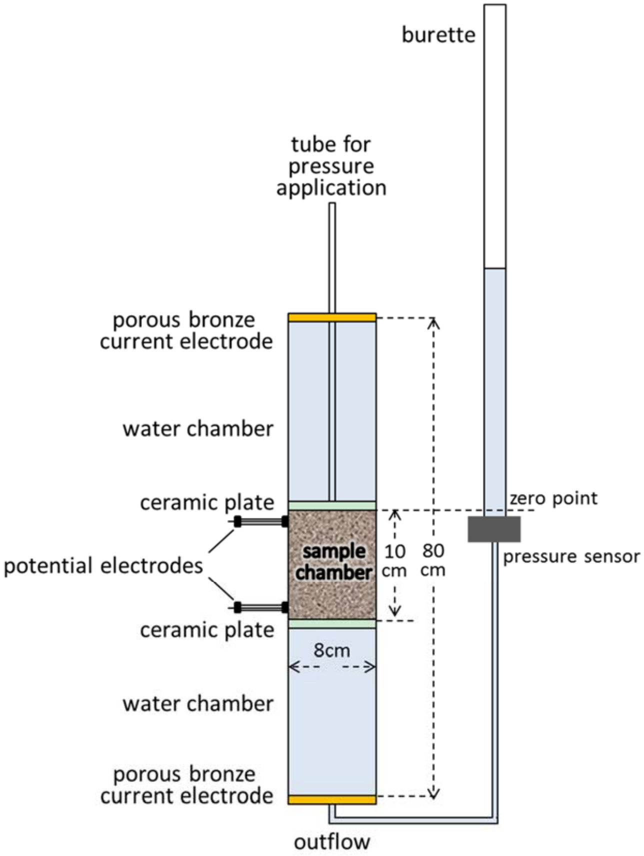

Figure 3-3. Sketch of the sample holder used to make SIP measurements during pressure drainage of unsaturated samples

3.3.4 Sample holder for SIP measurements during evaporative drying

The sample holder used to make SIP measurements during evaporative drying of unsaturated samples is a rectangular box made of PVC with a four-point electrode array (Fig. 3-4). The inner size of the box is 60 × 5.7 × 7.97 cm (length × width × height). Two porous bronze plates positioned at 12 cm from each end were used to inject current. The prepared soil material was filled into the sample holder between the two current electrodes. Two non-polarizable electrodes as described in Section 3.3.3 were inserted into the surface of the sample to measure the electrical potential. The distance between each of the adjacent electrodes was 12 cm according to the design guidelines provided in Zimmermann et al. (2008).

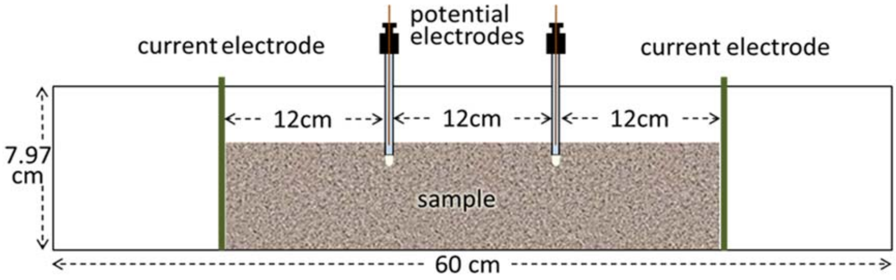

Figure 3-4. Sketch of the sample holder used to make SIP measurements during evaporative drying of unsaturated samples

3.4 SIP data acquisition and interpretation

3.4.1 SIP data acquisition

The complex impedance of all investigated samples was measured at 97 frequencies approximately equally spaced between 1 mHz and 45 kHz in log-space using the electrical impedance spectrometer described above. The SIP measurement started from the maximum frequency, decreasing to the minimum frequency, and then returning back to the maximum frequency. These repeated measurements were used to check for drift in sample properties during the relatively long duration of the SIP measurements (e.g., due to temperature variations, water outflow, or ion release from biochar during the 2.5-h-long SIP measurements). In all cases except for the samples during evaporation, it was found that this drift was negligible. All experiments were performed in the laboratory at a temperature of 19 to 23°C with a temperature variation of less than 0.5 °C during one single SIP measurement.

As introduced in Chapter 2.2, the measured complex impedance was converted to the complex electrical conductivity $\sigma^*(\omega)$ by using the appropriate geometrical factor k of the four-point electrode array (Eq. 2-5). For all sample holders, l_l is always the distance between the two potential electrodes. For both cylindrical sample holders, the area A was obtained from the inner radius of the sample holder. For the box, A is the cross-sectional area of the rectangular packed sample determined from the inner width of the box and the filling height of the sample material, which was indirectly obtained from the known inner height of the box and the measured distance between the surface of the sample and the top edge of the sample holder. The obtained complex conductivity was corrected to values at 20 °C by using a linear correction by 2 % per °C (Binley et al., 2010). Electromagnetic coupling caused by the contact impedance of the potential electrodes may strongly affect the measured signal at high frequencies (above 100 Hz). The correction method proposed by Huisman et al. (2016) was applied to minimize this effect.

3.4.2 Debye decomposition

Debye decomposition (DD) (Nordsiek and Weller, 2008; Weigand and Kemna, 2016a; Zisser et al., 2010) was used to obtain the relaxation time distribution (RTD) of the measured spectra with key parameters about the chargeability and relaxation time. DD decomposes the complex resistivity ρ^* into a superposition of N Debye relaxations:

$$\rho^* = \rho_0 \left[1 - \sum_{k=1}^{N} m_k \left(1 - \frac{1}{1 + i\omega\tau_k}\right)\right] \qquad (3—1)$$

where each of the N Debye spectra is defined by a chargeability m_k and an associated relaxation time τ_k, and the DC resistivity ρ. A user-defined range of τ_k values is used to obtain information about the relaxation time distribution (RTD). A larger m_k means a higher weight of the RTD term determined by τ_k. τ_{peak} refers to the local maximum of the RTD terms, which corresponds to the peak of the spectra of imaginary resistivity. τ_{peak} is useful if multiple dominant relaxation phenomena (and thus multiple polarization peaks) are present in a given SIP spectrum (Weigand and Kemna, 2016a). If there is only one peak in the spectrum like a single Cole-Cole curve (e.g. Warburg or Debye curve), τ_{peak} is determined by the τ_k of the maximum m_k. The summation of m_k yields the total chargeability M:

$$M = \sum_{k=1}^{N} m_k \qquad (3—2)$$

which is a measure for the area under the phase spectrum. The normalised total chargeability M_n is obtained by:

$$M_n = M/\rho_0 \qquad (3—3)$$

M_n was found to be a proxy for the polarizability of the internal surface (Lesmes and Frye, 2001; Weller et al., 2010). For materials with significant frequency-dependent electrical properties, M and M_n better represent the strength of polarization rather than the values of σ'', ρ'' or φ at a single frequency.

In this thesis, DD was performed using a Matlab implementation of Zisser et al. (2010). Hundred relaxation times (N = 100) in a range of $1/(10 \cdot 2\pi f_{max})$ s to $10/(10 \cdot 2\pi f_{min})$ s were used to fit each SIP spectrum where f_{min} = 0.001 and f_{max} = 10000 Hz. The extension of the time range by one decade to each side is equivalent to an extension of the frequency range by one decade with respect to the range covered by the data. This wider frequency range is needed because of the sensitivity of the fitted spectral complex resistivity to higher or lower relaxation times (or frequencies). However, only the chargeabilities within the frequency range of interest (from 0.001 to

10000 Hz) are used for the subsequent interpretation to minimize the influence of the used regularization on the obtained results. The fitting routine uses Tikhonov regularization to constrain the relaxation time distribution. Parameters of M, M_n, and τ_{peak} were used to analyse the results. More detailed information on the used DD implementation can be found in Zisser et al. (2010) and (Kelter et al., 2015).

Chapter 4. SIP measurements on saturated sand-biochar mixtures*

4.1 Introduction

The aim of this chapter is to determine the sensitivity of SIP to the presence of disseminated biochar in sand under various conditions. Therefore, the SIP response of sand-biochar mixtures of four different biochars from different feedstock and production processes will be investigated (PW700, PW800, BW550, HTC) as a function of the (1) mass fraction of biochar (%), (2) particle mean diameter d (mm) of biochar and (3) electrical conductivity of the electrolyte σ_w (mS m^{-1}). SIP measurements will be analysed using a Debye decomposition approach. The links between the SIP response and biochar properties will be discussed.

4.2 Materials and methods

4.2.1 Sample preparation

Homogeneous wetted mixtures of sand and investigated biochar with various size fraction and mass fraction were prepared by the method introduced in Chapter 3.2.3. This mixture was filled into the sample holder (see Chapter 3.3.2) in steps of about 1 cm^3 using a wet-packing procedure. The water surface was always kept about 0.5 cm higher than the sand-biochar mixture during the filling procedure. Small air bubbles

---

* This chapter has been adapted based on a published journal article:
Gao, Z., Haegel, F. H., Huisman, J. A., Esser, O., Zimmermann, E., & Vereecken, H. (2017). Spectral induced polarization for the characterisation of biochar in sand. *Near surface geophysics*, *15*(6), 645-656.

were removed by stirring slowly with the spoon. This procedure was repeated until the sample holder was filled. Although all sand-biochar mixtures were carefully prepared, deviations of up to 10 % of biochar content may have occurred along the column because the density difference between biochar and sand resulted in a tendency of biochar to separate from sand during wet packing. A blank control sample consisting of pure F36 sand was prepared with the same filling procedure.

After sample preparation, all samples were flushed with 4 mM NaCl solutions for at least 24 hours to equilibrate the electrolyte content in the samples and to control the electrical conductivity of the aqueous electrolyte solution (σ_w). The sample was flushed with a relatively low and constant flow rate of 0.5 L/hour to avoid disturbance of the distribution of biochar. In addition, samples with 1 % and 2 % biochar were further flushed with 6, 8, 12 and 16 mM NaCl solutions to investigate the dependence of the complex electrical conductivity on electrolyte concentration. The range of σ_w varied from 46 to 172 mS m^{-1} covering a range of salinity that is typically found in agricultural soil. It was difficult to achieve identical electrical conductivity for the inflow and outflow for each of the samples because of ions released from biochar. Flushing was maintained until the measured electrical conductivity of the outflow was stable and close to that of the inflow with the discrepancy less than 2 %. The properties of the sand-biochar mixtures investigated in this chapter are summarized in Tab. 4-1.

Table 4-1. Parameters of measured samples of sand-biochar mixture

Biochar in mixture	Particle diameter / mm	Mass fraction and associated range of pore water conductivity / mS m^{-1} (NaCl)			
		0.5 %	1 %	1.5 %	2 %
PW700	0.25-0.5	--	47	--	--
	0.5-1	--	47.4	--	--
	1-2	46.8	46.9 - 168.7	46.9	46.4 - 171.7
PW800	0.25-0.5	--	46	--	--
	0.5-1	46	46	47.2	47
	1-2	46 - 170	46 - 170.3	--	47.3 - 170.8
BW550	1-2	--	--	--	45 - 169.1
HTC	Powdery	--	45.5 – 169.5	47.5	47.5 - 170.7

The pore-volume-normalized surface area S_{por} as introduced in Chapter 2.4.8 was calculated using Eq. 2-24. Due to the low fraction of biochar in the mixture and the relatively large size of the particles of biochar compared to sand, preparation of a representative sample of the sand-biochar mixture for directly determining A_s of the mixture was not feasible. As an alternative, a mixing law was used to calculate S_{por} for each of the sand-biochar mixtures by:

$$S_{por} = [(1-\xi)\,(A_s(\text{sand})\,\rho_{ds}) + \xi\,(A_s(\text{BET})\,\rho_{db})]\,(1-\phi)/\phi \qquad (4—1)$$

where A_s(sand) is the specific surface area per unit mass of sand (0.16 m^2 g^{-1}), A_s(BET) is the specific surface area per unit mass of the considered biochar (Tab. 3-1), ρ_{ds} is the grain density of sand (2.6 g cm^{-3}), ρ_{db} is the skeletal density of biochar (1.8 g cm^{-3} for PW700, PW800 and BW550, 1.5 g cm^{-3} for HTC (Brewer et al., 2014)), ϕ is the porosity of the bulk sample (0.42 to 0.43), and ξ is the mass fraction of biochar.

4.2.2 SIP data acquisition and interpretation

After the samples were flushed with each prepared electrolyte for at least 24 hours and the electrical conductivity of the outflow was found to be constant, SIP measurements were conducted on the samples with the method introduced in Chapter 3.4.1 to obtain the complex electrical conductivity $\sigma^*(\omega)$ of the samples, which included the real part $\sigma'(\omega)$, imaginary part $\sigma''(\omega)$ and phase $\varphi(\omega)$. Debye decomposition (Chapter 3.4.2) was used to analyse the measured SIP data to yield the total chargeability M, and the normalized total chargeability M_n.

4.3 Results of measured complex electrical conductivity and Debye decomposition

4.3.1 Dependence on type of biochar

Fig. 4-1 shows $\sigma'(\omega)$ and $\sigma''(\omega)$ for sand-biochar mixtures with 2 % biochar and the pure sand sample saturated with 4 mM NaCl solution. $\sigma'(\omega)$ of the different sand-biochar mixtures showed nearly identical values at the lowest frequency. Similar DC conductivities with the same electrolyte concentration suggests that the samples have a similar formation factor for Archie's law (Archie, 1942) and thus a similar porosity, which provides confidence in the reproducibility of the sample preparation procedure. There was a significant increase of $\sigma'(\omega)$ with increasing frequency for both biochars from pine wood (i.e. PW700 and PW800) resulting from a large polarization of these samples in the investigated frequency range (Fig. 4-1a). A slight increase was found for biochar of type BW550, while $\sigma'(\omega)$ only marginally depended on frequency for HTC. The corresponding spectra of $\sigma''(\omega)$ are shown in Fig. 4-1b. Overall, all four investigated biochars showed a larger response of $\sigma''(\omega)$ in comparison with pure sand. PW700 and PW800 showed the largest peaks of $\sigma''(\omega)$, i.e. the strongest magnitude of polarization. For these two biochars, $\sigma''(\omega)$ exhibited the typical shape of a single Cole-Cole curve with a significant peak at approximately 5.5 Hz for PW700 and 0.4 Hz for PW800. BW550 showed a moderate peak at 2 Hz and a secondary peak at approximately 4000 Hz. HTC showed the weakest polarization compared to other types of biochar. The $\sigma''(\omega)$ of HTC exhibited a peak at about 40 Hz, with a value one order of magnitude larger than that of sand.

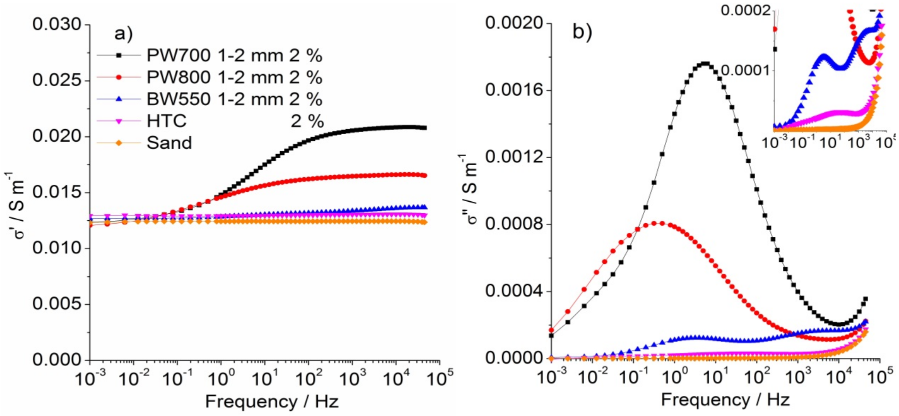

Figure 4-1. Complex conductivity of mixtures of sand and 2 % of different biochars (4 mM NaCl); a) real part, b) imaginary part. The inset expands the y-scale to highlight the spectra of samples with low polarization.

4.3.2 Dependence on mass fraction of biochar

Fig. 4-2 shows the effect of the amount of biochar on the SIP spectra for sand-PW800 (*d*: 0.5 - 1 mm) mixtures at an electrolyte concentration of 4 mM NaCl. The increasing mass fraction of biochar did not affect the DC conductivity and the position of the peak of $\sigma''(\omega)$ much, but increased $\sigma'(\omega)$ at high frequency and produced more pronounced peaks of $\sigma''(\omega)$. The measured complex conductivity of other types of biochar showed a similar dependence on mass fraction.

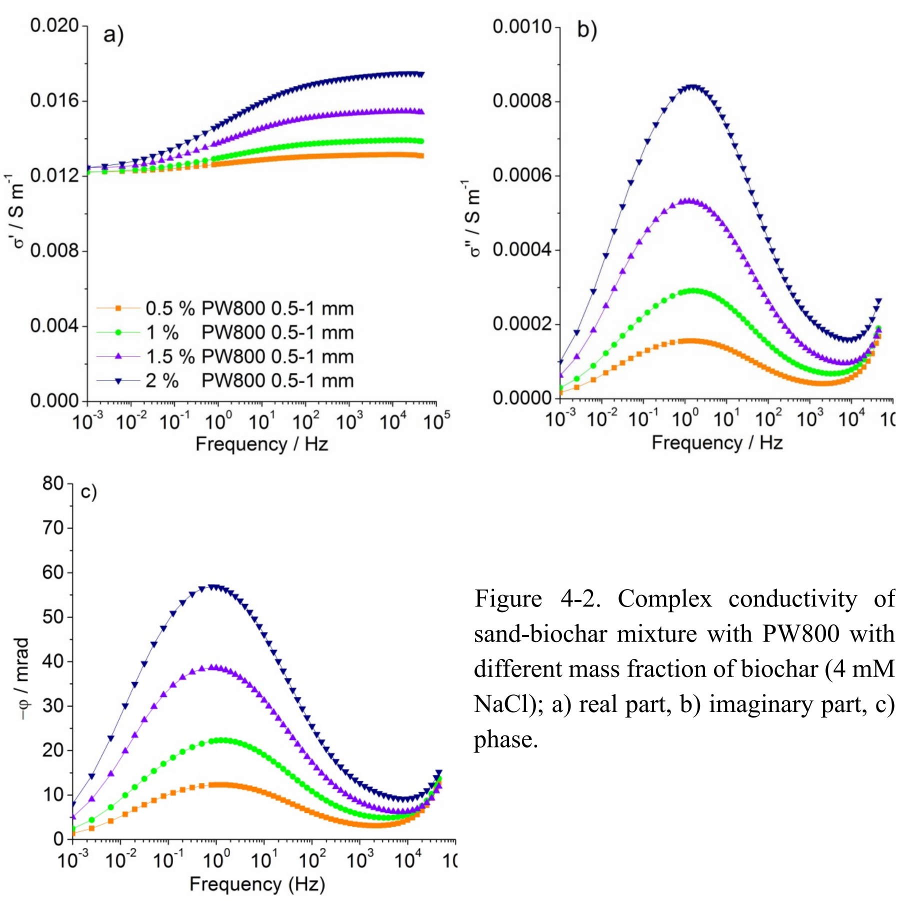

Figure 4-2. Complex conductivity of sand-biochar mixture with PW800 with different mass fraction of biochar (4 mM NaCl); a) real part, b) imaginary part, c) phase.

The SIP spectra of the sand-biochar mixtures were further examined by using Debye decomposition. In Fig. 4-3, the total chargeability M obtained from the Debye decomposition showed a linear relationship with the mass fraction of biochar. Linear regression models where the intercept is fixed to M for the pure sand with the same electrolyte concentration were fitted to the data. The pyrolytic biochars (i.e. PW700, PW800) showed a much larger slope than HTC. The deviation of the measured points from the linear fit is mainly a consequence of the heterogeneity of the biochars themselves and problems associated with obtaining a homogeneous biochar distribution in the samples during sample preparation (i.e. the mass fraction is known at the column scale but the SIP measurements are representative of the sand-biochar mixture between the two potential electrodes only). Repeated measurements showed a deviation of $\sigma''(\omega)$ or M of up to 20 % for these reasons. Overall, the results presented in Fig. 4-3 suggest that M is a potential indicator for the amount of the biochar in soil.

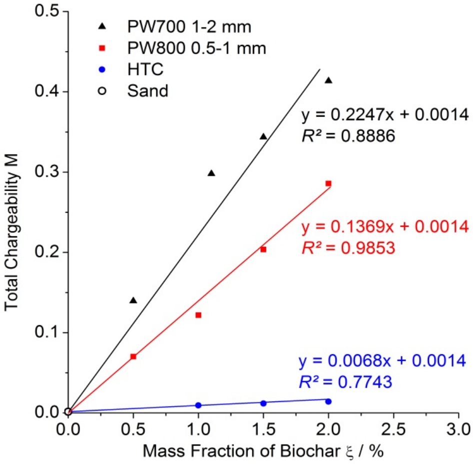

Figure 4-3. Total chargeability M of PW700, PW800 and HTC as a function of mass fraction of biochar in sand-biochar mixtures (4 mM NaCl).

4.3.3 The dependence on particle size of biochar

Fig. 4-4 shows how $\sigma''(\omega)$ depends on the diameter d of the biochar particles. Sand-biochar mixtures with the same mass fraction of 1% but three different size fractions of PW700 and PW800 were investigated at an electrolyte concentration of 4 mM NaCl, respectively. The peak frequencies of $\sigma''(\omega)$ shifted to lower frequencies with increasing d. This behaviour was expected since larger grains usually correspond to longer relaxation times for the SIP response. τ_{peak} values from Debye decomposition as a function of the d are shown in Fig. 4-5 for PW700 and PW800. A power-law relationship between τ_{peak} and d was found with exponents equal to 2.7 for PW700 and 2.3 for PW800.

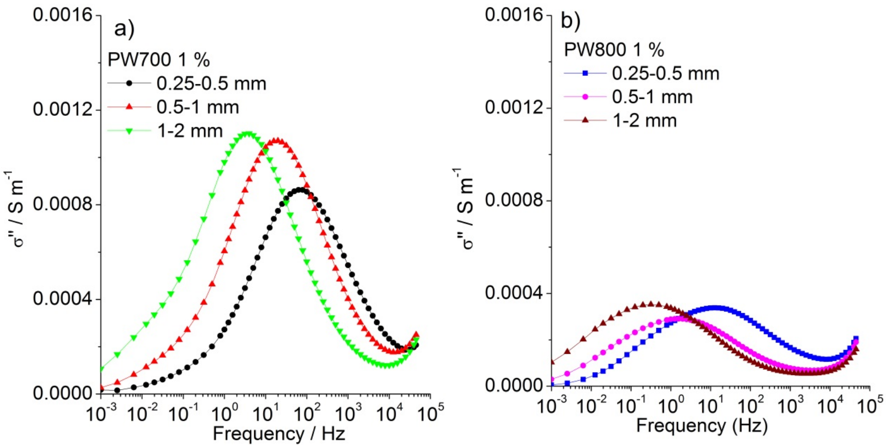

Figure 4-4. Imaginary part (*σ''*) of the complex conductivity of a) PW700 and b) PW800 with different particle diameter of biochar in sand-biochar mixtures (4 mM NaCl).

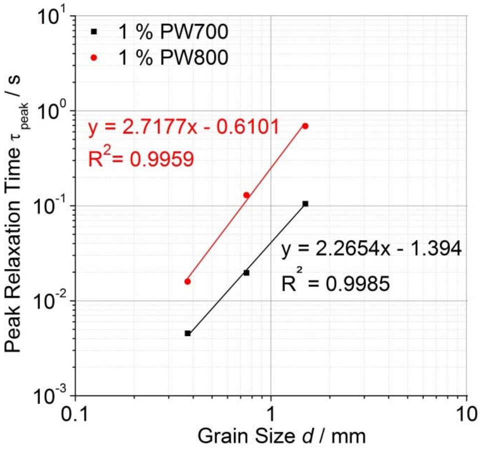

Figure 4-5. Peak relaxation time τ_{peak} of PW700 and PW800 as a function of grain diameter *d* of biochar in sand-biochar mixtures (4 mM NaCl).

4.3.4 Dependence on electrolyte concentration

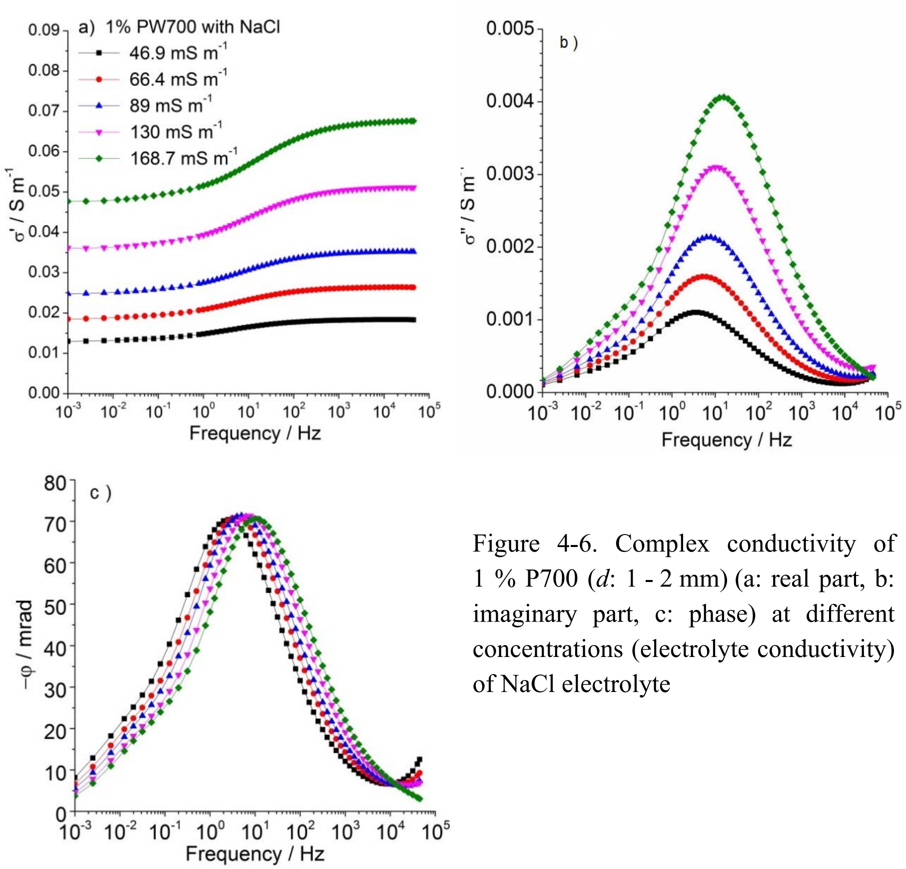

Figure 4-6. Complex conductivity of 1 % P700 (*d*: 1 - 2 mm) (a: real part, b: imaginary part, c: phase) at different concentrations (electrolyte conductivity) of NaCl electrolyte

Results presented in Fig. 4-6 to 4-9 show that σ_w had a significant influence on the measured complex electrical conductivity of all types of biochar. The DC conductivity was proportional to σ_w for all samples (Fig. 4-6a to 4-9a) in accordance with Archie's law (Archie, 1942). The biochars PW700 (Fig. 4-6b, c) and PW800 (Fig. 4-7b, c) showed similar behaviour for $\sigma''(\omega)$ and $\varphi(\omega)$. The magnitude of $\sigma''(\omega)$ increased and the peak in $\sigma''(\omega)$ shifted to higher frequencies with increasing electrolyte concentrations. However, the shape of the spectra remained relatively constant. The spectra of $\varphi(\omega)$ for PW700 showed an approximately parallel translation to higher frequencies with increasing electrolyte concentration. A similar parallel translation was observed for $\varphi(\omega)$ of PW800, although the peak magnitude slightly decreased for this biochar (Fig. 4-7c). Fig. 4-7 also shows that the observed σ_w-dependence is similar for mixtures with different mass fraction for biochar PW800.

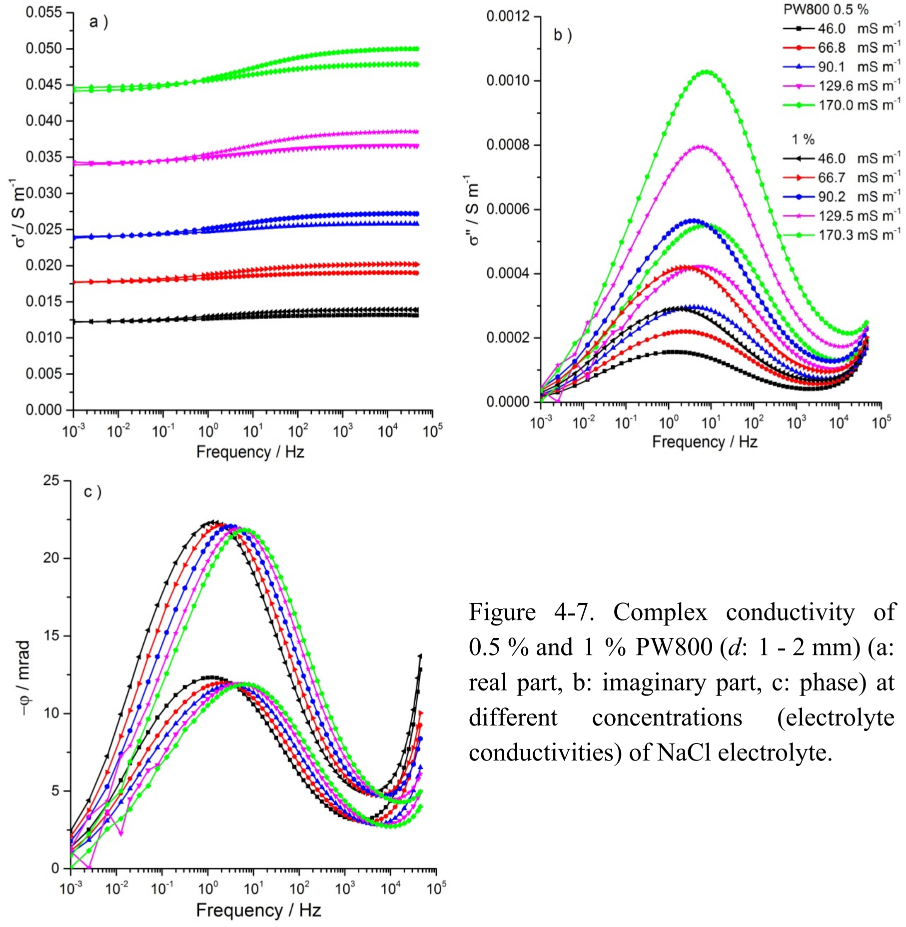

Figure 4-7. Complex conductivity of 0.5 % and 1 % PW800 (*d*: 1 - 2 mm) (a: real part, b: imaginary part, c: phase) at different concentrations (electrolyte conductivities) of NaCl electrolyte.

Spectra of complex electrical conductivity for biochar BW550 (Fig. 4-8) and HTC (Fig. 4-9) exhibited a similar dependence on σ_w. For these two biochars, an increase in $\sigma''(\omega)$ (Fig. 4-8b, Fig. 4-9b) with increasing electrolyte concentration was again observed, but the $\varphi(\omega)$ decreased considerably with increasing electrolyte concentration (Fig. 4-8c, Fig. 4-9c)in contrast to PW700 and PW800.

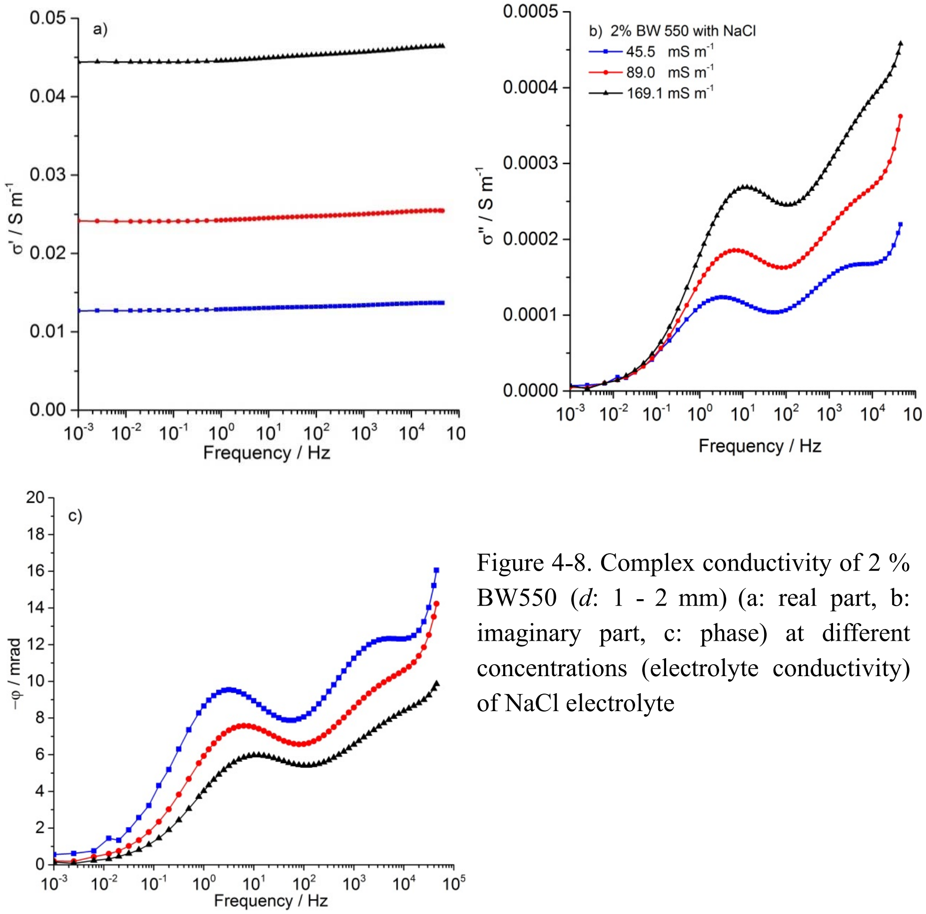

Figure 4-8. Complex conductivity of 2 % BW550 (*d*: 1 - 2 mm) (a: real part, b: imaginary part, c: phase) at different concentrations (electrolyte conductivity) of NaCl electrolyte

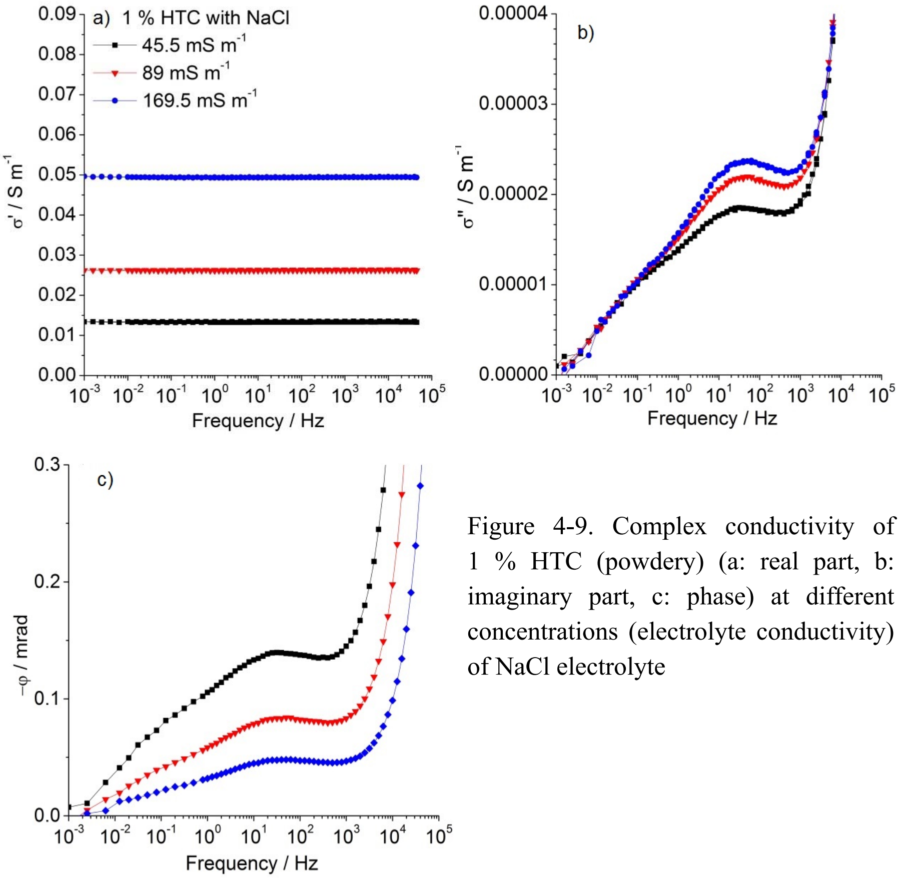

Figure 4-9. Complex conductivity of 1 % HTC (powdery) (a: real part, b: imaginary part, c: phase) at different concentrations (electrolyte conductivity) of NaCl electrolyte

The normalized chargeability M_n and the peak relaxation time τ_{peak} were determined using Debye Decomposition. In general, M_n increased with increasing electrolyte concentration for all four types of biochar (Fig. 4-10). A nearly linear relationship with σ_w was observed for mixtures with 2 % PW700 and PW800. M_n increased approximately with the square root of σ_w for mixtures with 2 % BW550. The samples with 2 % HTC did not show a power-law dependence on σ_w at all. τ_{peak} decreased with increasing σ_w for PW700, PW800 and BW550 (Fig. 4-11). In contrast, the τ_{peak} of HTC remained constant with varying σ_w within the measurement accuracy.

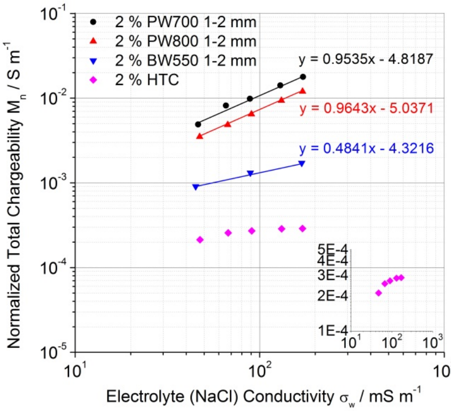

Figure 4-10. Normalized total chargeability M_n of mixtures of 2 % PW700, PW800, BW550 and HTC in sand as a function of electrolyte conductivity (NaCl).

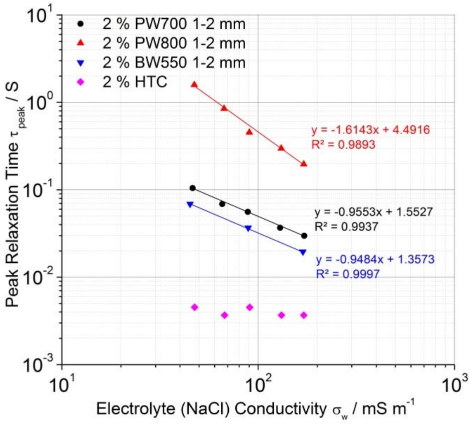

Figure 4-11. Peak relaxation time τ_{peak} of mixtures of 2 % PW700, PW800, BW550 and HTC in sand as a function of electrolyte conductivity (NaCl).

4.4 Discussion

This chapter presented systematic SIP measurements on sand-biochar mixtures. The results clearly show that the type of biochar is a main factor that influences the SIP response of sand-biochar mixtures (Fig. 4-1). Biochar exhibits large variations of the electrical conductivity depending on the degree of carbonization and associated graphitization (Gabhi et al., 2017), and materials with larger electrical conductivity are expected to cause stronger polarisation. Generally, a higher heating temperature and a longer heating time during the production process result in a higher degree of carbonization. Hoffmann et al. (2019) found the high carbonization temperature and high specific surface area lead to the increase of electrical conductivity. With its distinct low carbon content, high H/C and O/C ratios (Tab. 3-1), and the low production temperature, HTC is expected to be the least electrically conductive biochar. Variations between the three types of pyrolytic biochar are due to their different production temperature and production processes (e.g. presence of air in the case of PW700). Gabhi et al. (2017) reported that the electrical conductivity of biochar derived from the same kind of biomass increased by six orders of magnitude when the biochar was exposed to higher temperature during pyrolysis. This was accompanied by a moderate increase of the carbon content by 7 % and a reduction of the H/C ratio by 46 %, which indicates a higher degree of carbonization. The increase in electrical conductivity was, however, mainly attributed to a simultaneous increase of graphitization. Haegel et al. (2012) reported that $\sigma''(\omega)$ was negatively correlated with the H content for biochar derived from wood. The same relationship between polarization and carbon content or H/C ratio was also found for PW700 with different particle diameters but not for PW800 (Fig. 4-4). However, differences were relatively small (chargeability between 0.23 and 0.30 for PW700 and between 0.12 and 0.14 for PW800) and unambiguous correlations could not be obtained. BW550 had the largest carbon content but a higher H/C ratio and a weaker polarization compared with other pyrolytic biochars derived from wood (PW700 and PW800). Apparently, the graphitization of BW550 is lower due to the lower production temperature. In addition, BW550 had a lower BET surface area (Tab. 3-1). This also suggests that the structure of biochar and/or the feedstock may have a significant effect on polarization. A clear proof of this influence, however, would require systematic investigations on tailored products made from the same feedstock using different pyrolysis temperatures and processes.

Overall, we conclude that there is a general qualitative correspondence between the observed strength of the polarization and the electrical conductivity of biochar inferred from pyrolysis temperature and chemical composition of the four biochars. However, more quantitative data on the electrical conductivity of particulate biochars would be needed to obtain more reliable relationships between the polarization and the electrical conductivity of biochars. Such data are still rare for particulate biochar. Previous studies have presented measurements on larger blocky samples (Gabhi et al., 2017; Jiang et al., 2013), or powders of biochar (Hoffmann et al., 2020; Hoffmann et al., 2019). However, these studies neglected the internal structure (e.g. porosity) of particle which can influence the interpretation of the electrical conductivity of biochars considerably. Unfortunately, the determination of the electrical conductivity of solid biochar remains challenging, and is beyond the scope of this study.

The characteristics of the SIP spectra of sand-biochar mixtures can qualitatively be compared to those of other materials. Generally, the SIP response of pyrolytic biochar (PW700, PW800 and BW550) showed similar characteristics as metallic materials, in particular for the pine-wood biochars (PW700 and PW800) which were produced at higher temperature. For example, the observed phase shift for 2 % silver nanoparticles in sand saturated with NaCl solution exhibited a typical Cole-Cole spectrum with a single maximum (Joyce et al., 2012) similar to the σ'' for PW800 and PW700 (Fig. 4-1). The peak phase of the porous media with 2% silver nanoparticles was about 75 mrad, which is in between the 55 mrad for PW800 and 110 mrad for PW700 for the same mass fraction. The phase maximum obtained for the sand-biochar mixture with 2 % BW550 sample (about 18 mrad) is in the same order of magnitude as that from 2 % pyrite in a sand-agar gel matrix (12 - 15 mrad) (Revil et al., 2015a). Okay et al. (2014) found that $\sigma''(\omega)$ for a mixture of sand and 1 % clay is in the range of 10^{-6} - 10^{-4} S m^{-1}, and increases slightly with increasing σ_w, similar to the sand-HTC mixture investigated here. Gurin et al. (2015) found that $M_n \propto \sigma_w$ for metallic materials (galena, cryptomelane, chalcopyrite, iron) corresponding to our results for PW700 and PW800 (Fig. 4-10). M_n of HTC showed a smaller increase beyond σ_w > 80 mS m^{-1} (Fig. 4-10). Similar behaviour was also observed for sand (Slater and Glaser, 2003) and sandstone (Weller et al., 2011). Lesmes and Frye (2001) attributed this behaviour to changes of surface charge density and ionic mobility for non-metallic materials. Increasing electrolyte concentration leads to a stronger association of ions at the mineral-electrolyte interface and a compression of the diffuse double layer which might result in a reduced mobility of the ions due to ion-ion interactions. Weller et al. (2010) argued that conductive particles are able to support a higher charge density per unit S_{por} and therefore do not show a saturation effect of σ'' with increasing σ_w.

The power-law exponents for the relationship between τ_{peak} and d were 2.7 for PW700 and 2.3 for PW800. These values are somewhat larger than the value of 2 typically suggested by models of EDL polarization and membrane polarization for non-conductive particles (see Chapter 2). The Wong model and the PPIP model (see Chapter 2) predict a decrease of τ_{peak} for increasing σ_w for conductive particles, in agreement with the measured results by Gurin et al. (2015) and the behaviour of PW700, PW800 and BW550 in this study (Fig. 4-10). In contrast, the τ_{peak} of HTC did not depend on σ_w, as expected for non-conductive materials. It is important to realize that all available models have been derived for non-porous particles. The effect of an internal porosity and surface area on the SIP response of biochar is unknown, and needs to be investigated in further experimental and modelling studies.

Previous studies have shown that a relationship between SIP parameters and the specific surface area per unit mass normalized to the pore volume, S_{por}, exists for various materials including metallic mineral-sand mixtures and clay-sand mixtures

(Slater et al., 2006; Weller et al., 2015b; Weller et al., 2010). These relationships suggest that $\sigma''(\omega)$ at a specific frequency or M_n is approximately linearly dependent on S_{por}. As the SIP spectra of biochar have a relatively strong frequency dependence, it is more suitable to show M_n rather than $\sigma''(\omega)$ as a function of S_{por} (Fig. 4-12). In comparison with other data sets (e.g. Fig. 3 in Weller et al. (2010)), M_n values of biochar fell in between the values of conductive or semi-conductive materials (iron/magnetite) and clay. PW700 showed the largest M_n, close to metallic materials, while HTC showed values in a similar range as sand-clay mixtures. PW800 and BW550 showed values in between these two extremes. This further substantiates the notion that pyrolytic biochars are electronic conductors or semiconductors and that electrode polarization (see Chapter 2) of particles of biochar might be the dominating mechanism of polarization. In contrast, the main mechanism of polarization for HTC seems to be double-layer polarization, which is further supported by the reduced increase of M_n with increasing electrolyte concentration (Fig. 4-10) and the insensitivity of τ_{peak} to σ_w (Fig. 4-11). It should be mentioned that S_{por} of biochar might be overestimated due to the potentially large errors for BET determination on biochar. In particular, the heating procedure for BET determination may have vaporized the organic matter of biochar, thus increasing the measured surface area (Sigmund et al., 2017).

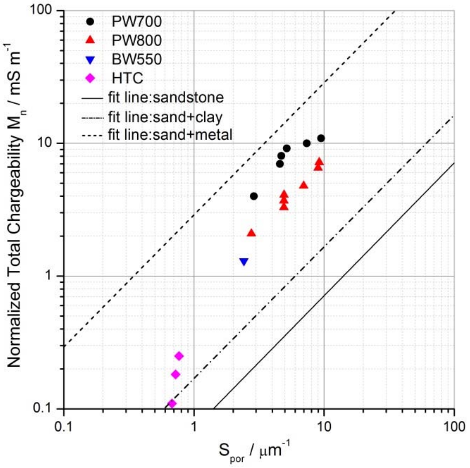

Figure 4-12. Relationship between normalized total chargeability M_n derived from Debye decomposition and the normalized specific surface area per unti mass S_{por} for different sand-biochar mixtures (NaCl electrolyte, 100 mS m^{-1}). For comparison, fitting curves for different materials from Weller et al. (2010) are also provided.

4.5 Conclusions

This chapter demonstrates that it is possible to detect and characterize particles of biochar in a sand matrix by SIP. All measured biochars exhibited an obvious frequency-dependent SIP response. The dependence of SIP spectra on key physical and chemical properties were discussed in this chapter. By comparing the SIP measurement on biochar and previous data on other materials, the polarizing mechanism for biochar was qualitatively analysed. However, a mechanistic model to improve the understanding of the polarization of biochar would still be beneficial to develop strategies and techniques for quantitatively analysing biochar in soil. This will be addressed in the following chapter.

Chapter 5. Modeling the spectral induced polarization data of saturated sand-biochar mixtures

5.1 Introduction

As illustrated in Chapter 2, the interpretation of the induced polarization of porous media depends heavily on the absence or presence of electrically conductive minerals. The (S)IP response of conductive minerals has been utilized in mineral exploration of base metals for a long time (Nelson and Van Voorhis, 1983; Seigel et al., 2007). More recently, there is also increasing interest for environmental purposes, such as evaluating the potential risk of pollution from mine tailings (Placencia-Gomez et al., 2015) and monitoring amendments for contaminated site remediation such as silver nanoparticles (Aal et al., 2017). The results presented in Chapter 4 suggest that the SIP response of some types of biochar in sand-biochar mixtures has similar characteristics as the response of metallic particles in terms of amplitude and phase of the complex electrical conductivity. This is supported by previous studies that showed that both particles and powders of black carbon materials have considerable electrical conductivity (Gabhi et al., 2017; Kastening et al., 1997). It is also likely that redox reactions occur at the surface of biochar given the expected surface groups (Biniak et al., 2001; Kastening et al., 1994; Kastening et al., 1997), which may additionally influence the polarization of sand-biochar mixtures.

Although there are numerous studies presenting (S)IP measurements, only a limited number of studies have used mechanistic models for characterizing the polarization of porous media with electrically conductive minerals. Therefore, it is of interest to explore whether the available models for disseminated conductive minerals introduced in Chapter 2 can be applied to describe the SIP response of porous media with biochar inclusion. The Wong model was originally developed for disseminated sulfide ores. Using this model, Placencia-Gomez et al. (2013) and Placencia-Gomez and Slater (2014) explored whether SIP can be used to infer oxidative-weathering conditions of mine waste deposits. They found that the Wong model was able to predict the SIP response of deposits containing pyrite and pyrrhotite in the low-frequency range (below 100 Hz). The Revil model was also applied to a broad database of semiconductors and the fitted parameters describing a Cole-Cole type spectrum were related to the electrical and physical properties of disseminated conductive particles directly (Revil et al., 2015a; Revil et al., 2015b). The availability of a suitable mechanistic modeling approach to describe sand-biochar mixtures would be beneficial for the interpretation of the SIP response in field applications where environmental conditions (e.g. water content, pore water chemistry) are expected to change. As a first step to establishing such a modeling approach, this chapter explores whether the models of Wong (1979) and Revil et al. (2015b) allow describing the SIP response of saturated sand-biochar mixtures. In particular, the relationship between model parameters and sample properties such as electrolyte chemistry as well as the amount and size of biochar particles will be investigated and discussed.

5.2 Considerations about the polarization of biochar

As already discussed in previous chapters, biochar is generally a highly porous material with a large specific surface area due to its abundant macropores and micropores. It also has numerous surface functional groups. The electrical properties of active carbon have been investigated in detail by Kastening et al. (1997). They found that porous particles of active carbon show a considerable electrical conductivity, but that the mechanisms determining the electrical conductivity are different from those of pure metallic materials or semiconductors. They proposed a so-called “hopping” mechanism to explain the observed electrical conductivity. In this model, it is assumed that the skeleton of the particle exhibits a turbostratic structure that contains spatially separated graphite-like conductive domains with free charge carriers inside. The graphitic layers of neighbouring domains are twisted toward each other with weak electronic overlap. Therefore, the current path exhibits electronic barriers between the conductive domains that restrict the free flow of charge carriers and the transfer of electrons from one domain to another adjacent domain. As a result, the electronic conductivity determined by the mobility and the associated diffusion coefficient of the charge carriers is expected to be lower for biochar than for pure graphite or metal.

In the case of biochar particles, it is expected that the electrically conductive zones are formed by layers of condensed 6-membered rings associated with the π-bonds of carbon atoms in the sp^2 state, which are formed from the sp^3 state in the original biomass through the process of carbonization during thermal decomposition (Biniak et al., 2001). Thus, the electrical conductivity of biochar is expected to be highly influenced by the feedstock used to create biochar and the conditions of the production process, such as heating temperature, contact time and gas or liquid composition during the heat treatment. Moreover, the electrical conductivity may show anisotropy due to the anisotropic graphitic crystallite alignment originating from the structure of feedstock. Recently, Gabhi et al. (2017) investigated six types of biochar derived from various feedstock and found that the skeletal conductivity of biochar particles was positively correlated with the degree of carbonization and varied in a large range from 2.5×10^{-4} to 399.7 S m^{-1}. This range is comparable to that of semiconductors and the highest measured value is similar to the electrical conductivity of a single graphite crystal. Gabhi et al. (2017) also attributed the high skeletal conductivity to the presence of randomly oriented sheet structures of graphite crystals in the biochar.

In case of the Wong model, redox reactions and associated leakage currents across the particle-electrolyte interface are also considered. In the case of biochar, it is possible that charge transfer occurs at the interface of the biochar and the electrolytic solution. Surface chemical analyses have shown that biochar contains various functional groups at the surface, e.g. hydroxyl groups (phenolic or alcoholic), carbonyl groups (including quinones) and carboxylic groups (Pereira et al., 2015). Dissolved ions (e.g. $Fe^{2+/3+}$) or water molecules (H^+, OH^-) in the electrolytic background can potentially be oxidized or reduced by those surface functional groups. One possible relevant schematic redox reaction between water and biochar is illustrated in Fig. 5-1. Electrons can be transferred from water to a quinone group at the positive (anodic) side of the biochar particle while oxygen is released. On another site on the surface of the biochar particle, a possible cathodic reaction can occur with hydroquinone as the donor that gives electrons to water and hydrogen is released.

Cathodic reaction

$2\ H_2O + 2\ e^- \rightarrow H_2 + 2\ OH^-$

Anodic reaction

$H_2O \rightarrow 2\ H^+ + 2e^- + 1/2\ O_2$

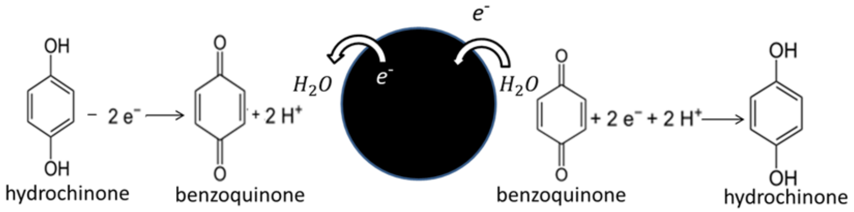

Figure 5-1. Schematic illustration of a possible redox reaction at the surface of biochar.

The occurrence of redox reactions at the surface of biochar is supported by the observed irreversible and reversible Faradaic processes at the surface of carbon electrodes (Pandolfo and Hollenkamp, 2006). In particular, leakage currents across the carbon electrode interface were reported to be positively correlated with the amount of surface functional groups. However, ionic adsorption associated with charge transfer in a two-electrode system is likely different from the polarization of disseminated biochar particles because the potential difference across a millimeter-sized biochar particle is considerably smaller than the potential difference between anode and cathode in a typical electrochemical cell. Therefore, the number of reduced and oxidized species produced during the polarizing process of the biochar is small according to the Nernst equation:

$$E_{cell} = E^0 + (R_{gas}T/z_{tr})\ln(c_{ox}/c_{red}) \qquad (5—1)$$

where E_{cell} is the potential of the cell, E_0 is the standard potential of the redox reaction, R_{gas} is the ideal gas constant, T is the temperature, z_{tr} is the number of transferred electrons, F is the Faraday constant, c_{ox} is the concentration of the oxidized species and c_{red} is the concentration of the reduced species. The value of c_{ox}/c_{red} is referred to as reaction quotient. In the case of SIP measurements in this work, 5 V peak voltage during over a distance of 18 cm in the sample holder was applied corresponding to an electrical field of the cell of 0.278 V cm^{-1} and a voltage difference of 27.8 mV for a 1 mm particle of biochar. For instance, E^0 for water splitting at pH 7 is 1.23 V and E^0 for Fe^{2+}/Fe^{3+} is + 0.77 V. Despite the relatively small potential difference across disseminated biochar particles, the results obtained for charged carbon electrodes in electrolyte indicate that the surface functional groups of biochar can participate in redox reactions on the interface between biochar particles and electrolyte.

The porous nature of biochar particles is also expected to play an important role in the electrical polarization of biochar. Previous studies have shown that the charging process in the pores of carbon materials is dependent on the pore size and the electrical conductivity of the electrolyte (Kastening and Heins, 2005). The very large BET surface area of biochar particles (Sigmund et al., 2017) suggests that the majority of surface area is found within micropores and macropores of the biochar particles. Therefore, the majority of surface functional groups are expected to be located at pore surfaces and not on the outside of the particle. This might lead to a slower movement of ions near the reactive sites and a limited accessibility to the redox-reactive sites. In addition, the EDL of opposing pore walls in micropores is expected to overlap and, consequently, ion diffusion is restricted due to the membrane polarization (Kastening and Heins, 2005). In addition, the type of ions also influences the penetration of electrolyte into small pores since larger ions (e.g., Ca^{2+}) may not be able to enter micropores (or only after the removal of their solvating shell). This may also explain why the anticipated proportional relationship between the EDL capacitance and the available surface area of porous carbon was sometimes not observed (Salitra et al., 2000).

Given the physical and electrochemical properties of biochar reviewed in this section, a suitable model to describe the polarization of biochar should ideally consider the polarization of the EDL around conductive particles associated with 1) electrical conduction in the solid phase of biochar, 2) possible electrochemical reactions occurring at the surface functional groups of biochar, and 3) movement of charge carriers around the outside of the particle and in the saturated pores of the particle of biochar. The available model approaches proposed by Wong (1979) and Revil et al. (2015b) that were discussed in Chapter 2 are partly able to describe these processes, but they are clearly substantially simplified. For example, the instantaneous movement of charges inside the conductive particle assumed by the Wong model may not be fully applicable to biochar. The Revil model neglects possible redox reactions between biochar and electrolyte. In addition, both models only consider non-porous spherical particles. Despite these limitations, it is worthwhile to explore to what extent these two models can describe the induced polarization of porous media containing biochar particles.

5.3 Data and methods

5.3.1 Properties of investigated biochar

SIP measurements on four types of biochar mixed with sand were presented in

Chapter 4. Two of those biochars with strong polarization (PW700 and PW800) were selected for this study. Some physical and chemical parameters of the investigated biochars are listed in Table 3-1. Considering the possible implications for modelling, the two following biochar properties are highlighted here again. First, contact with air during heating resulted in a higher oxygen/carbon ratio (O/C ratio) for PW700 and a potentially larger amount of oxygen-containing surface groups, which may lead to more redox reactions. In contrast, PW800 is assumed to have been pyrolized in a relatively short time leading to an insufficient carbonization and thus a potentially lower electrical conductivity. Although no accurate information on the contact time of pyrolysis is available, this hypothesis is supported by the inhomogeneous color and the presence of some residual woody fragments in the obtained material of PW800 that were removed before sample preparation.

5.3.2 SIP data and properties of samples

The modelling presented in this chapter is focussed on the SIP measurements on saturated sand-biochar mixtures with PW700 and PW800 that were presented in Chapter 4. In particular, it will be explored whether the model is able to capture the effect of mass fraction, size of biochar particles, as well as various concentration of NaCl electrolyte on the SIP response. To further investigate the importance of electrolyte type and redox processes, additional SIP measurements will be presented and modelled here too. These additional SIP measurements were made on the sample of sand-biochar mixture with a 2% mass fraction of PW700 biochar with a particle diameter range between 1 - 2 mm. The parameters and results of this sample with NaCl electrolyte was presented in Chapter 4 (Fig. 4-1, Fig. 4-10, Fig. 4-11 Tab. 4-1). After flushing with the NaCl electrolyte with increasing concentration (4 mM, 6 mM, 8 mM, 12 mM and 16 mM), the sample was flushed with 4 mM NaCl electrolyte again and made the SIP measurement to verify the consistency of the sample. Next, the sample was flushed successively with different electrolytes. 2 mM $CaCl_2$ solution was applied at first, which has a similar electrical conductivity as the 4mM NaCl solution. After that, the sand-biochar mixture was flushed with a mixture of $CaCl_2$-$FeSO_4$ solution. Here, the fraction of $FeSO_4$ solution was stepwise increased from a molar percentage of 0 to molar percentages of 5 %, 20 % and 40 %, while the conductivity of the electrolyte was kept constant around 0.046 S m^{-1}. The electrolyte solutions were prepared with deionized water. Oxygen was largely excluded from the solutions containing $FeSO_4$ by permanent flushing with nitrogen. The result of this additional measurement will be presented and discussed associated with the possible redox reaction and modelling results in the next chapter thus they are not shown in this chapter for conciseness. The SIP measurements were conducted on the sample for each electrolyte and concentration gradient with the sample method as in Chapter 4. The properties of this additionally measured sand-biochar mixture with $CaCl_2$ and $CaCl_2$-$FeSO_4$ solution are summarized in Tab. 5-1. Other parameters of investigated sand-biochar mixtures with PW700 and PW800 with NaCl solution refer to Tab. 4-1.

Table 5-1. Properties of the investigated sand-biochar mixtures

Biochar in mixture	Particle diameter *d* / mm	Mass fraction of biochar / %	Electrolyte	Pore-water conductivity / mS m^{-1}
PW700	1-2	2	100 % $CaCl_2$	47.0
			95% $CaCl_2$+5% $FeSO_4$	46.2
			80% $CaCl_2$+20% $FeSO_4$	45.9
			60% $CaCl_2$+40% $FeSO_4$	45.2

5.3.3 Estimation of parameters for the Wong model and Revil model

To apply the Wong model to experimental data, a considerable number of model parameters needs to be defined. The effective electrical conductivity according to the Wong model is provided by Eq. 2-14 and 2-15. The related parameters are summarized in Tab. 2-1. A priori reduction of the number of model parameters used for model fitting is desirable to improve the reliability of the model fits and the interpretability of the fitted model parameters. Therefore, some model parameters were given fixed values using reasonable assumptions or previously reported values (R, σ_w, c_0, ε, α and β). The remaining parameters were fitted within physically reasonable ranges to provide the best match with the experimental data (ν_w, D, σ_0, and c_r).

Appropriate values for the fixed model parameters in the Wong model were determined as follows. The particle size d ($d = 2R$) of the biochar was described by a distribution of different radius fractions R_i. A uniform distribution between the mesh sizes of the sieves (i.e., R = 0.125 - 0.25 mm, 0.25 - 0.5 mm, 0.5 - 1 mm) was assumed and ten equidistant size classes were used to define R_i. In contrast to Wong (1979), the conductivity of the electrolyte σ_w was used rather than the DC conductivity of the sample σ_0 to calculate the Debye screening length $(\sqrt{2}\chi)^{-1}$. The conductivity of the electrolyte σ_w was assumed to be equal to the measured electrical conductivity of the outflow during the flushing procedure. c_0 refers to the concentration of the electrolyte. The specification of an appropriate value of the dielectric permittivity ε of water in the Wong model is more challenging. The ε of bulk water has a value of $78\varepsilon_0$ at 25 °C, where ε_0 is the permittivity of free space, which is 8.85×10^{-12} F m^{-1}. However, Wong (1979) argued that ε in this model should reflect the state of the electrolyte near the particle-liquid interface. Considering the reduced ability of water molecules at the interface to freely orientate themselves in an applied electrical field, it is expected that the appropriate value for ε is lower than that of bulk water (Wong, 1979). Detailed investigations have shown that ε of the first layer of water molecules near a charged surface is about $6\varepsilon_0$ (Bockris and Reddy, 1973). From the second layer to the bulk water, ε was estimated to increase from about $6\varepsilon_0$ to $78\varepsilon_0$ (at 25 °C) with a mean value of about $40\varepsilon_0$ (Bockris and Reddy, 1973). Wong (1979) assumed a value of $11.3\varepsilon_0$ (10^{-10} F m^{-1}) for a smooth particle surface. In the case of biochar, a stronger immobilization of water molecules near the surface is anticipated because of the rougher surface and the important role of the large surface area in micropores for the total surface area. For this reason, a value of $\varepsilon = 7\varepsilon_0$ was applied in this study. Finally, the electrochemical reaction parameters α and β in the Wong model were fixed a priori. Wong (1979) introduced the parameters α and β to define the net reaction current density across the metal-electrolyte interface. The parameter α is related to the migration of active ions under the influence of an external electrical field, and the parameter β is related to the diffusive perturbation of the concentration of active ions. Appropriate values for α and β can be derived from the equilibrium exchange current density i_0, which represents the charge exchange without an external electric field, using:

$$\alpha = \frac{i_0 l}{c_2 k_B T} \qquad (5—2a)$$

$$\beta = \frac{i_0}{e c_2} \qquad (5—2b)$$

where k_B is the Boltzmann constant (1.381×10^{-23} J K^{-1}), e is the elementary charge (1.6×10^{-19} C), T is the absolute temperature (293 K, as room temperature), and l is the distance between the particle surface and the outer Helmholtz layer (assumed to be 0.4 nm in this study). Reported values for i_0 vary from 10^{-12} to 10^{3} A m^{-2} depending on the material, the specific reaction and other conditions (Wong, 1979), which implies a wide range of possible values for α and β. Since direct measurements of i_0 are not available for the biochars investigated here, we assumed that i_0 was around 1.6×10^{-7} A m^{-2}. This value can be obtained from the measurement on porous carbon material (Kastening and Heins, 2005).

After determining appropriate values for the fixed model parameters, suitable parameter ranges need to be defined for the remaining parameters that will be estimated through model fitting. The volume fraction v_w significantly influences the strength of the induced polarization as expressed by the magnitude of $\varphi(\omega)$ and $\sigma''(\omega)$. For the case of solid conductive spheres with a smooth surface disseminated in a sand media, the volume fraction of conductive particles can be calculated from the mass fraction of conductive particles and the ratio of the grain density of the conductive inclusions and the sand. For the case of biochar, the high porosity of the particles and the rough surface are expected to increase the effective volume fraction significantly. A rough estimate of the v_w for a sand-PW700 mixture (1 % mass fraction of biochar) using the porosity of the pure sand and the sand-biochar mixture, the grain density of the sand, and the skeletal density of biochar particles suggests that the value of the volume fraction of biochar can be 5 to 6 times that of the mass fraction (also see Chapter 6). Due to this uncertainty, the v_w was treated as a fitting parameter in this study. Wong (1979) suggested that his model is only applicable for volume fractions below 16 % because interactions between the induced dipole moments of individual particles are not considered. Therefore, the acceptable parameter range was defined by the mass fractions of the sample (lower limit) up to a maximum value of 16 %.

The mobility of the ions μ was directly coupled with the diffusion coefficient D through $\mu = (40\ \mathrm{V}^{-1})\cdot D$ at 20 °C (Wong, 1979). The D of the ions in bulk solution for the used electrolytes (i.e. Na^+, Ca^{2+}, Cl^-, SO_4^{2-}) are between 1.0 to $1.5 \times 10^{-9}\ \mathrm{m^2\ s^{-1}}$ at 25°C. However, the effective D near the surface of the biochar can be much smaller because of the restricted motion of the water molecules and the ions near the interface and in the narrow pores due to van der Waals and electrostatic forces. For example, the effective D in micropores of active carbon was reported to be one order of magnitude smaller than that in dilute solutions (Kastening and Heins, 2005). Arguing along the same line, Placencia-Gomez et al. (2015) assumed that D can range from 10^{-11} to $10^{-9}\ \mathrm{m^2\ s^{-1}}$ for pyrite-sand and pyrrhotite-sand mixtures saturated with tap water. Therefore, the acceptable range of values for D was defined as 10^{-11} to $1.5 \times 10^{-9}\ \mathrm{m^2\ s^{-1}}$.

The Wong model predicts a decreasing DC conductivity σ_0 with increasing v_w (i.e., Fig. 9 in Wong 1979). This can be explained by the fully developed quasi-equilibrium diffuse layer that acts as a screen of the electrical field (Bücker et al., 2019). However, this behaviour was not observed for the sand-biochar mixtures investigated in this thesis. For a saturated sample, it is expected that σ_0 is proportional to σ_w according to Archie's law (Archie, 1942). The results presented in Chapter 4 showed a relatively constant σ_0 for sand-biochar mixtures with the same σ_w but different types and mass fractions of biochar. This difference between the Wong model and the experimental results might be attributed to the macropores that penetrate the particles of biochar, which are thus permeable for the electrolyte. These macropores provide an additional pathway of electromigration through the biochar particle. Ions may be transported there rather than exclusively along the surface around a solid conductive particle as in the case of the original work of Wong (1979) and studies on many types of metal-bearing rock. To ensure a good fit between model and experimental data, it was necessary to treat σ_0 in the Wong model as a fitting parameter. The range of possible values was restricted between 1 and 2 times the measured real part of the electrical conductivity at the lowest frequency (1 mHz). Finally, the fraction of active ions c_r was allowed to vary in the full range between 0 and 1, since no information is available for this fit parameter.

To apply the Revil model, the SIP measurements were first fitted by a single Cole-Cole model (Eq. 2-12) to obtain the chargeability M (dimensionless), the Cole-Cole exponent c_{cc} (dimensionless) and the relaxation time τ_0 (s). The fitted M was used to estimate the volume fraction v_R of biochar in mixtures (Eq. 2-17), which may be different from v_w in the Wong model. The τ_0 and the mean particle radius R of the biochar were used to estimate the effective diffusion coefficient D_m of the charge carriers inside the particles of biochar (Eq. 2-18).

The model fits presented in this chapter were all obtained with the nonlinear fitting function "lsqnonlin" of Matlab (The MathWorks Inc., Natick, US). The objective function was the sum of squared residuals between the effective electrical complex conductivity derived from the Wong model or Cole-Cole model and the measured values. The residuals for the real part and imaginary part were calculated separately and then summed. The residuals of the imaginary part were weighted by a factor of 10 stronger than the residuals of the real part, which ensured that both were in the same order of magnitude. The SIP measurements were only modelled for frequencies below 10 kHz, since measurements above this frequency are less reliable for the SIP system used here (Zimmermann et al., 2008b; Huisman et al., 2016).

5.4 Results and Discussion

5.4.1 Measured complex electrical conductivity of sand-biochar mixtures

As discussed in detail in Chapter 4, the measured $\sigma^*(\omega)$ of the sand-biochar mixtures prepared with PW700 and PW800 showed a similar behavior regarding the effects of the applied amount (Fig. 4-2), the particle size of biochar (Fig. 4-3), and the concentration of electrolytes (Fig. 4-4 and Fig. 4-7). It was found that a larger amount of biochar in the sand-biochar mixtures resulted in an increased $\sigma''(\omega)$ and a corresponding steeper increase of $\sigma'(\omega)$. Also, an increased particle size of the biochar resulted in broader relaxation spectra of $\varphi(\omega)$ and $\sigma''(\omega)$ and a decrease in the peak frequency. Finally, an increase of electrolyte concentration resulted in a proportional increase of $\sigma'(\omega)$ and $\sigma''(\omega)$, while the magnitude of $\varphi(\omega)$ remained relatively constant with a parallel translation of the peak to higher frequencies.

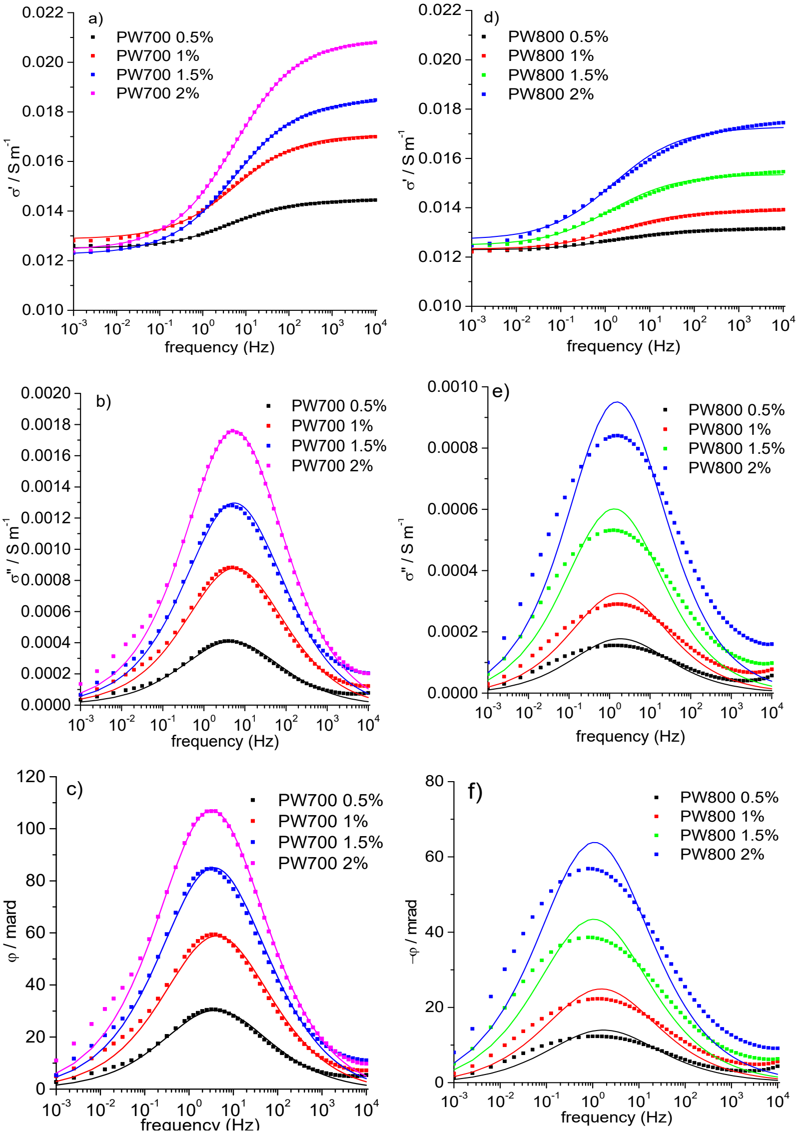

Figure 5-2. Real part $\sigma'(\omega)$, imaginary part $\sigma''(\omega)$, and phase $\varphi(\omega)$ of the measured complex electrical conductivity for sand-biochar mixtures with various mass fractions of PW700 (a, b, c) and PW800 (d, e, f) with 4 mM NaCl (dots). The predictions obtained with the Wong model using the prescribed and fitted model parameters in Tab. 5-4 and Tab. 5-5 are also provided (lines).

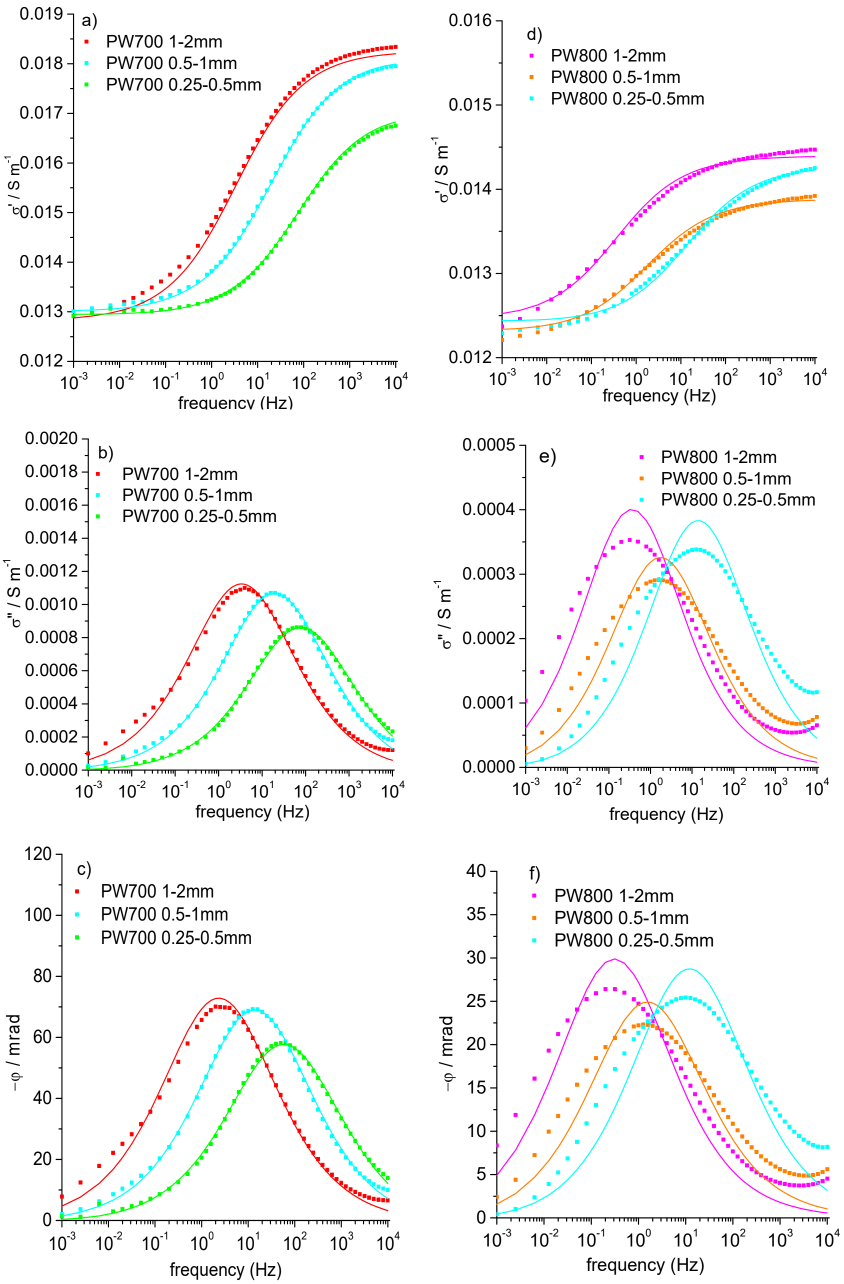

Figure 5-3. Real part $\sigma'(\omega)$, imaginary part $\sigma''(\omega)$, and phase $\varphi(\omega)$ of the measured complex electrical conductivity for sand-biochar mixtures with various particles sizes of PW700 (a, b, c) and PW800 (d, e, f) with 4 mM NaCl (dots). The predictions obtained with the Wong model using the prescribed and fitted model parameters in Tab. 5-4 and Tab. 5-5 are also provided (lines).

The results of the additional measurements made to investigate the influence of the electrolyte chemistry (NaCl, $CaCl_2$, $CaCl_2$-$FeSO_4$) and possible redox reactions on the measured complex electrical conductivity of PW700 are shown in Fig. 5-5. Generally, it was found that a change of the type of electrolyte while maintaining a nearly constant σ_w of the solution had only a minor influence on the SIP response of the sand-biochar mixtures. This can be seen from the phase spectra shown in Fig. 5-5a. After a change of the electrolyte from NaCl to $CaCl_2$, the measured spectra of $\sigma''(\omega)$ and $\varphi(\omega)$ decreased slightly in the low-frequency range but showed steeper peaks with nearly constant peak frequency f_p. The maxima of the measured $\sigma''(\omega)$ and $\varphi(\omega)$ decreased slightly when the $CaCl_2$ solution was replaced by the $CaCl_2$-$FeSO_4$ solution. The changes in the SIP response in the presence of $FeSO_4$ in solution are assumed to be related to redox reactions, which will be discussed in more detail later in this chapter.

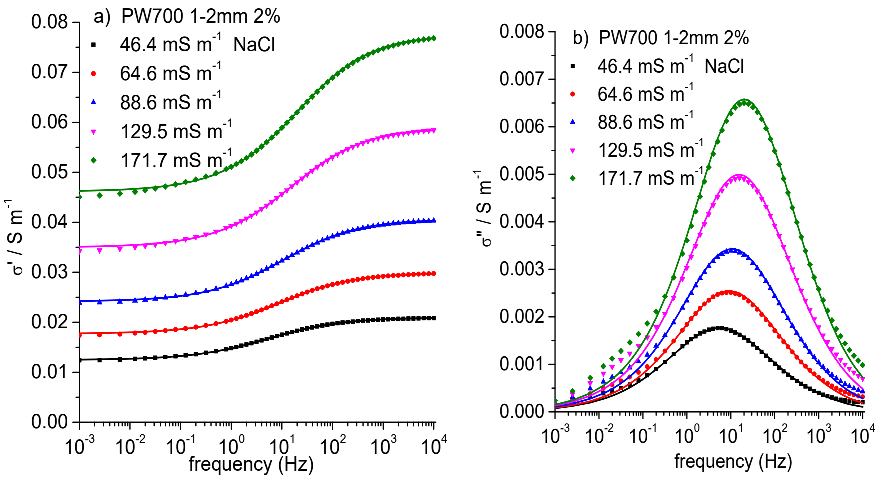

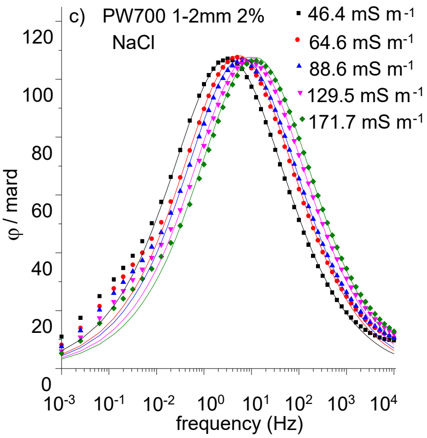

Figure 5-4. Real part $\sigma'(\omega)$ (a), imaginary part $\sigma''(\omega)$ (b), and phase $\varphi(\omega)$ (c) of the measured complex electrical conductivity for sand-biochar mixtures with PW700 biochar with different concentrations of NaCl electrolyte (dots). The predictions obtained with the Wong model using the prescribed and fitted model parameters in Tab 5-4 are also provided (lines).

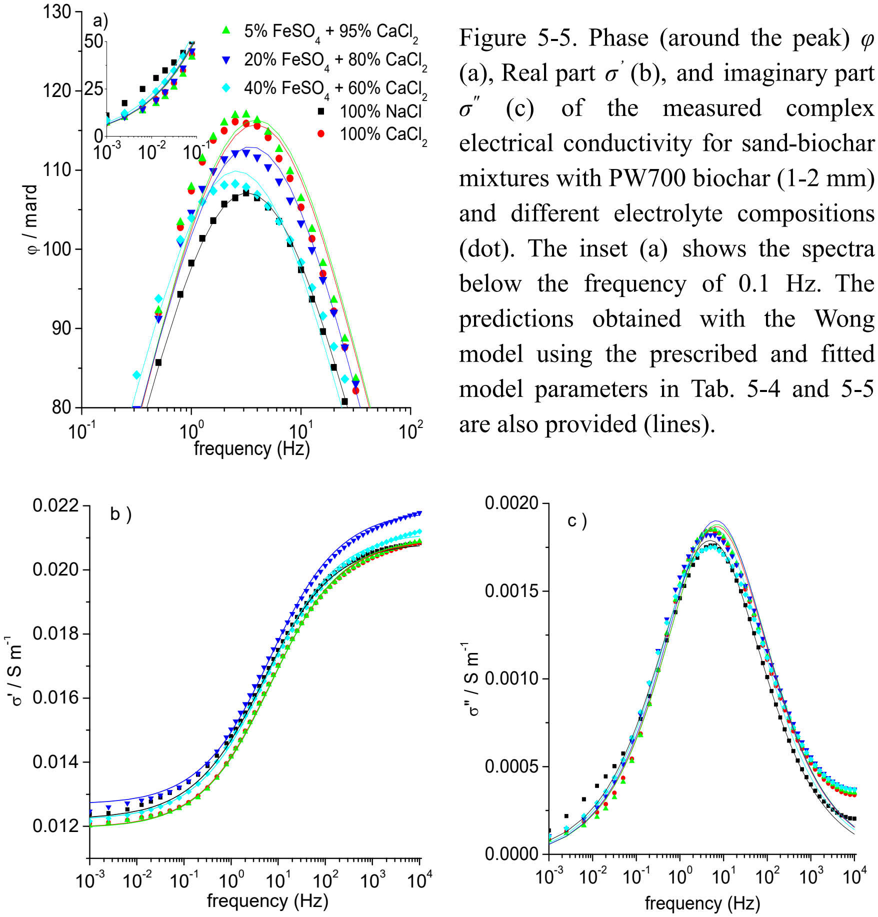

Figure 5-5. Phase (around the peak) φ (a), Real part σ' (b), and imaginary part σ'' (c) of the measured complex electrical conductivity for sand-biochar mixtures with PW700 biochar (1-2 mm) and different electrolyte compositions (dot). The inset (a) shows the spectra below the frequency of 0.1 Hz. The predictions obtained with the Wong model using the prescribed and fitted model parameters in Tab. 5-4 and 5-5 are also provided (lines).

5.4.2 Model fitting results and analysis for the Revil model

The Cole-Cole model was flexible enough to be able to fit the measured SIP spectra very closely for both types of biochar. The given and fitted model parameters are summarized in Tab. 5-2. The fitted chargeability M_{cc} increased with increasing mass fraction of biochar. An increase in particle size of biochar resulted in a decrease of the fitted relaxation time τ_0. Also, τ_0 approximately inversely linear decreased with increasing pore-water conductivity σ_w for the sand-biochar mixtures, which was in correspondence with the shift of the phase spectra with increasing electrolyte concentration (Fig. 5-4c) and the analysis on the peak relaxation time in Chapter 4

(Fig. 4-11). The fitted Cole-Cole exponent c_{cc} for the PW700 biochar varied around 0.5, which is identical to the exponent of the Warburg model. The fitted c_{cc} for the PW800 biochar was found to be somewhat lower and varied around 0.4.

Table 5-2. Summary of the fitted parameters of the Cole-Cole model.

Biochar	w/w %	Particle diameter *d* / mm	Electrolyte / mol %	σ_w / mS m^{-1}	*M*	τ_0 / s	c_{cc}
Given					Cole-Cole Model		
PW700	0.5	1-2	100% NaCl	46.8	0.14	0.051	0.49
PW700	1	1-2		46.9	0.31	0.051	0.49
PW700	1.5	1-2		46.9	0.34	0.031	0.49
PW700	1	0.5-1		47.4	0.27	0.010	0.53
PW700	1	0.25-0.5		47.0	0.23	0.003	0.56
PW700 (one sample)	2	1-2	100% NaCl	46.4	0.43	0.032	0.47
	2	1-2		64.6	0.43	0.019	0.47
	2	1-2		88.6	0.43	0.016	0.47
	2	1-2		129.5	0.43	0.011	0.47
	2	1-2		171.7	0.43	0.008	0.47
	2	1-2	100% $CaCl_2$	47.0	0.45	0.030	0.47
	2	1-2	95% $CaCl_2$+ 5% $FeSO_4$	46.2	0.45	0.031	0.48
	2	1-2	80% $CaCl_2$+ 20% $FeSO_4$	45.9	0.45	0.030	0.45
	2	1-2	60 % $CaCl_2$+ 40% $FeSO_4$	45.2	0.46	0.036	0.44
PW800	0.5	0.5-1	100% NaCl	46.0	0.07	0.111	0.40
PW800	1	0.5-1		46.0	0.13	0.104	0.40
PW800	1.5	0.5-1		47.2	0.20	0.109	0.43
PW800	2	0.5-1		47.0	0.30	0.113	0.40
PW800	1	0.25-0.5		46.0	0.14	0.016	0.46
PW800	1	1-2		46.0	0.16	0.639	0.38

Using the fitted parameters of the Cole-Cole model, the volume fraction of biochar in the mixture v_R and the effective diffusion coefficient of the charge carriers within the particles of biochar D_m were estimated following the considerations of the Revil model (Tab. 5-3). The v_R varied around 5 to 7 times the mass fraction for PW700 (except for the packing of 0.5 % mass fraction) and around 3 times the mass fraction for PW800.

The volume fraction obtained for PW700 is close to the estimated value based on particle density (also see Chapter 6). The estimated D_m is around 10^{-5} m^2 s^{-1} for PW700 and 10^{-6} m^2 s^{-1} for PW800. Gurin et al. (2015) and Revil et al. (2015a) reviewed a broad base of SIP measurements and their own measurements on various sand-semiconductor mixtures including galena, pyrite, chalcopyrite, magnetite, cryptomelane, zero-valent iron and porous graphite. They found that the D_m derived from the $\tau \sim R^2$ relationship varied from 10^{-11} to 10^{-5} m^2 s^{-1}. The D_m for PW800 was of the same order of magnitude as those published for chalcopyrite and galena, while the D_m for PW700 was on the highest end of the values observed for disseminated semi-conductive materials. Overall, these results are in agreement with the qualitative assumptions about the electrical conductivity of the two types of biochar already presented in Chapter 4.

Tab. 5-3 shows that the estimated D_m decreased with increasing salinity of the pore solution for sand-biochar mixtures with PW700. This was already reported by Gurin et al. (2015) for other conductive minerals. Abdulsamad et al. (2017) argued that the higher concentration of ions in the pore solution may lead to a faster charging process (smaller τ) around the conductive particle. However, this seems inconsistent with the assumptions of the Revil model, where D_m should not be influenced by the charge carriers outside the particle. Although the order of magnitude of D_m is still meaningful to qualitatively classify the type of material, these results suggest that important processes are not adequately considered in the relatively simple modelling approach of Revil et al. (2015b).

Table 5-3. Summary of the calculated parameters of the Revil model

Biochar	w/w %	Particle diameter *d* / mm	Electrolyte / mol %	σ_w / mS m^{-1}	v_R / %	D_m / m^2 s^{-1}
Given					Revil Model	
PW700	0.5	1-2	100% NaCl	46.8	3.1	1.1×10^{-5}
PW700	1	1-2		46.9	6.9	1.1×10^{-5}
PW700	1.5	1-2		46.9	7.6	1.8×10^{-5}
PW700	1	0.5-1		47.4	6.0	1.4×10^{-5}
PW700	1	0. 25-0.5		47.0	5.1	1.2×10^{-5}
PW700 (one sample)	2	1-2	100% NaCl	46.4	9.6	1.8×10^{-5}
	2	1-2	100% NaCl	64.6	9.6	3.0×10^{-5}
	2	1-2		88.6	9.6	3.5×10^{-5}
	2	1-2		129.5	9.6	5.1×10^{-5}
	2	1-2		171.7	9.6	7.0×10^{-5}
	2	1-2	100%$CaCl_2$	47.0	10.0	1.9×10^{-5}
	2	1-2	95% $CaCl_2$ +5% $FeSO_4$	46.2	10.0	1.8×10^{-5}
	2	1-2	80% $CaCl_2$ +20% $FeSO_4$	45.9	10.0	1.9×10^{-5}
	2	1-2	60 % $CaCl_2$ +40% $FeSO_4$	45.2	10.2	1.6×10^{-5}
PW800	0.5	0.5-1	100% NaCl	46.0	1.6	1.3×10^{-6}
PW800	1	0.5-1		46.0	2.9	1.4×10^{-6}
PW800	1.5	0.5-1		47.2	4.4	1.3×10^{-6}
PW800	2	0.5-1		47.0	6.7	1.2×10^{-6}
PW800	1	0.25-0.5		46.0	3.1	2.2×10^{-6}
PW800	1	1-2		46.0	3.6	8.8×10^{-7}

5.4.3 Model fitting results and analysis for the Wong model

The prescribed and fitted model parameters for the Wong model are provided in Tab. 5-4 for the sand-biochar mixtures with PW700 and in Tab. 5-5 for PW800. In general, the Wong model was able to fit the complex electrical conductivity of the sand-biochar mixtures with PW700 with good accuracy (Fig. 5-2, 5-3, 5-4). In the case of PW800, the fit is less good. Only $\sigma'(\omega)$ and the peak relaxation frequency f_p were reasonably described (Fig. 5-2, 5-3). Wong (1979) already indicated that his model is only able to describe Cole-Cole-type spectra with an exponent between that of a Warburg model and Debye model (i.e., c_{cc} between 0.5 and 1.0). Thus, the shape of the SIP spectra for PW800 with a c_{cc} around 0.4 was too broad to be fitted with the Wong model. This is perhaps related to the relatively low electrical conductivity of the PW800 particles, which may invalidate the assumption of instantaneous polarization used in the Wong model. As mentioned earlier, PW800 was found to be insufficiently carbonized during pyrolysis, possibly leading to a smaller overlap of graphite layers and a fragmented distribution of the graphite-like conductive domains, which increases the barriers for charge transfer inside the material. This is also supported by the results for the Revil model, where the D_m for PW800 was one order of magnitude smaller than that for PW700.

The fitted values for the volume fraction of PW700 biochar particles v_W were about 6.5 times the mass fraction, which is in good agreement with the volume fraction estimated from the particle density (see Chapter 6) and the results of v_R obtained with the Revil model. Both Placencia-Gomez and Slater (2014) and Wong (1979) reported that the fitted v overestimated the actual volume fraction. This was attributed to the elongated shape of the particles that deviated from the assumed spherical particles (Wong, 1979). Although Revil et al. (2015b) argued that the shape factor has very limited influence on the polarization of conductive particles, the considerable effect of the variable shape factors for elongated metallic particles was predicted by the modification of the Wong model proposed by Wong and Strangway (1981). They found that ellipsoidal particles with the long axis parallel to the applied electric field can yield much stronger polarization than spherical particles. However, when the particles are oriented with their long axis perpendicular to the electrical field, the magnitude of the polarization was similar to that of spherical particles. The latter case likely applies to the sand-biochar mixtures considered here. Since the mixtures were packed in saturated conditions with a slight excess of electrolyte, some biochar particles floated at the electrolyte surface during sample preparation because of the low grain density of biochar. Thus, the expected preferred orientation of the long axis of the biochar particles is perpendicular to the electrical field in the SIP measurements presented here (if any). This may explain why v_w was not overestimated for PW700. Interestingly, the fitted v_w for PW800 (Tab. 5-5) was around 3 times that of the mass fraction, which is again in agreement with the volume fraction v_R (Tab. 5-3) derived from the Revil model. However, the difference in the fitted effective volume fraction for PW700 and PW800 for the same mass fraction is hard to explain reasonably given the similar feedstock and pyrolysis process. A more detailed characterization of the biochars would be required to elucidate the observed differences in the SIP response.

The fitted D_w values obtained with the Wong model ranged from 3×10^{-10} to 4×10^{-10} m^2 s^{-1}, which is about one fourth of the diffusion coefficient in dilute solutions. These values are in agreement with the range fitted by Placencia-Gomez and Slater (2014). As argued above, the diffusion coefficient for internal surfaces inside porous biochar particles is expected to be smaller than that for a smooth outer surface because diffusion in micropores is restricted. Despite the variation in mass fraction and particle size of biochar, the fitted value for σ_0 (Tab. 5-4) was approximately the same for the sand-PW700 mixtures with the same pore-water conductivity. This result is consistent with the overlapping measured SIP spectra at low frequencies (Fig. 5-2). In a recent study by Bücker et al. (2019), it was found that a pre-charged surface (in the absence of an electrical field) will reduce the screening effect of the EDL, thereby increasing DC conductivity and relaxation time while decreasing the magnitude of the polarization. As argued above, it is assumed that σ_0 is independent of the concentration of biochar due to the porous nature of the particles, which allows electrolytic conduction through the particle. The fitted values of c_r also were relatively similar, which is reasonable since c_0 and c_2 are expected to be constant for the same pore-water conductivity.

As expected, an increase of the pore-water conductivity resulted in higher values of fitted σ_0 and lower fitted values of c_r (Tab. 5-4). This can be attributed to the increasing concentration of the inactive ions Na^+ and Cl^- in the host media, which enhanced the DC conductivity of the mixture according to Archie's law (Archie, 1942) but did not contribute to the charge-transfer reactions. To describe the SIP measurements after a change of the electrolyte from NaCl to $CaCl_2$ (Fig. 5-5), the fitted c_r parameter was reduced from 0.018 for NaCl to 0.014 for $CaCl_2$ to better fit the steeper peak in the imaginary part of the electrical conductivity. This lower fitted value may be caused by irreversible reactions between surface functional groups and Ca^{2+} that block the reactive sites on the surface of biochar. A possible explanation for the observed decrease of $\sigma''(\omega)$ and $\varphi(\omega)$ at low frequencies when $CaCl_2$ was used instead of NaCl solution is related to the charging process of the micropores of the biochar particles. The smallest pores with the lowest diffusion coefficients for counterions may be entered by Na^+, but Ca^{2+} may be excluded due to an ion-selective effect of micropores (Salitra et al., 2000). This would lead to a loss of polarization at low frequencies. However, the effect of changing the type of electrolyte on the polarization of sand-biochar mixtures was generally small, as also indicated by the very small changes in M_{cc} and τ_0 derived by fitting the Cole-Cole model (Tab. 5-2). With an increasing amount of $FeSO_4$ in the $CaCl_2$-$FeSO_4$ electrolyte solution, the fitted c_r increased from 0.014 to 0.018. This suggests that Fe^{2+} might be engaged in a charge-transfer reaction. However, the molar percentage of $FeSO_4$ increased from 0 to 40%, whereas c_r only showed a mild increase of about 25% (Tab. 5-4). Therefore, the influence of the concentration of Fe^{2+} on the intensity of the redox reaction is disproportionate.

Table 5-4. Summary of sample properties and prescribed and fitted Wong model parameters for sand-biochar mixtures with PW700.

w/w %	Particle diameter d / mm	Electrolyte / mol %	σ_w / S m^{-1}	$\varepsilon / \varepsilon_0$	i_0 / 10^{-7} A m^{-2}	c_r	D / 10^{-10} m^2 s^{-1}	v_w / %	σ_0 / S m^{-1}
		Given					Model		
0.5	1-2	100% NaCl	0.046	7	1.6	0.016	3.6	3.3	0.0131
1	1-2		0.046	7	1.6	0.014	3.0	6.4	0.0142
1.5	1-2		0.046	7	1.6	0.016	3.2	9.3	0.0141
1	0.5-1		0.046	7	1.6	0.014	3.7	7.5	0.0145
1	0.25-0.5		0.046	7	1.6	0.017	3.6	6.1	0.0141
2	1-2	100% NaCl	0.046	7	1.6	0.018	3.7	11.8	0.0149
2	1-2		0.065	7	1.6	0.013	3.7	11.9	0.0212
2	1-2		0.089	7	1.6	0.012	3.9	11.8	0.0289
2	1-2		0.130	7	1.6	0.010	3.8	11.8	0.0419
2	1-2		0.172	7	1.6	0.008	3.9	11.7	0.0552
2	1-2	100% $CaCl_2$	0.047	7	1.6	0.014	3.0	12.7	0.0145
2	1-2	95% $CaCl_2$+ 5% $FeSO_4$	0.046	7	1.6	0.014	3.0	12.8	0.0144
2	1-2	80% $CaCl_2$+ 20% $FeSO_4$	0.046	7	1.6	0.015	3.0	12.5	0.0146
2	1-2	60% $CaCl_2$+ 40% FeSO4	0.045	7	1.6	0.018	3.2	12.2	0.0145

Table 5-5. Summary of sample properties and prescribed and fitted Wong model parameters for sand-biochar mixtures with PW800.

w/w %	Particle diameter d / mm	Electrolyte	σ_w / S m^{-1}	$\varepsilon / \varepsilon_0$	i_0 / 10^{-7} A m^{-2}	c_r	D / 10^{-10} m^2 s^{-1}	v_w / %	σ_0 / S m^{-1}
		Given					Model		
0.5	0.5-1	100 % NaCl	0.046	7	1.6	0.017	4.0	1.5	0.0126
1	0.5-1		0.046	7	1.6	0.020	4.0	2.8	0.0128
1.5	0.5-1		0.046	7	1.6	0.017	4.0	4.7	0.0134
2	0.5-15		0.046	7	1.6	0.018	4.0	7.2	0.0140
1	0.25-0.5		0.046	7	1.6	0.017	3.0	3.1	0.0130
1	1-2		0.046	7	1.6	0.017	4.0	3.3	0.0130

5.5 Summary and outlook

In this chapter, it was attempted to improve the understanding of electrical polarization in sand-biochar mixtures by linking the physical properties of the samples with mechanistic SIP models. The Wong model was partially able to describe the complex electrical conductivity of sand-biochar mixtures. It is interesting to note that the Wong model has rarely been applied even though it has been around for a considerable time. Surely, this is partly because of the complicated mathematical expressions used in this model. It is also clear that the disseminated metalliferous particles commonly investigated by SIP are usually semiconductors (e.g. pyrite, magnetite and chalcopyrite) with a relatively low mobility of charge carriers compared to a perfect conductor. Therefore, the assumption of instantaneous particle polarization used in the Wong model may not be widely applicable as in the case of the biochar PW800 used here. In addition, the parameters of redox reaction between the soil solution and conductive inclusion are not easy to be investigated or determined. Recent studies on the SIP response of mixtures with conductive materials (Abdulsamad et al., 2017; Misra et al., 2016; Revil et al., 2015b) have mainly considered the process of building-up the dipole moment and EDL, but have so far ignored possible redox reactions. Considering the expected variation in the electrical conductivity of different types of biochar particles, it is evident that the movement of charges inside biochar particles needs to be considered. The Revil model is a simple and straightforward model to consider this. However, it misses some key parameters to describe measured samples (especially for the host media), thus leading to imprecise results. Clearly, a robust mechanistic model is currently not available to support non-invasive monitoring of biochar. Likely, such a model needs to consider multiple polarization mechanisms because of the large variation of properties of different types of biochar. The recently proposed mechanistic SIP models developed by Abdulsamad et al. (2017) and Misra et al. (2016) consider diffusion coefficients of charge carriers both in the disseminated particles and the host medium, and are thus potentially very interesting. However, these models require precise determination of many parameters, such as the conductivity of biochar particles and the density of all charge carriers. Unfortunately, this information is typically not known.

Chapter 6. Spectral induced polarization on unsaturated sand-biochar mixture*

6.1 Introduction

Chapters 4 and 5 presented first SIP measurements and modelling work on saturated sand-biochar mixtures with four types of biochar. The results showed that two of these biochars exhibited strong polarization, which was attributed to the electrical conductivity of the biochar particles caused by the higher degree of graphitization. Although these results were a first promising step towards the use of SIP to characterize biochar, it was focused on the SIP signature of biochar in saturated soil. For possible future field studies, it is also important to understand how unsaturated conditions affect the SIP signature of biochar in soil.

The objective of this chapter is to investigate how the SIP spectra of sand-biochar mixtures change with saturation. Pressure drainage and evaporative drying are two strategies commonly used to conduct SIP measurements on unsaturated samples (Binley et al., 2005; Breede et al., 2011; Ulrich and Slater, 2004). Ulrich and Slater (2004) suggested that the first approach is more representative for draining and filling caused by water table changes in the vadose zone and the influence of plant water uptake on capillary water, which is perhaps corresponding to the long-term environment of biochar after field application. The second approach using evaporation is more representative of the topsoil where the biochar is initially applied.

---

* This chapter has been adapted based on a published journal article:
Gao, Z., Haegel, F. H., Esser, O., Zimmermann, E., Vereecken, H., & Huisman, J. A. (2019). Spectral induced polarization of biochar in variably saturated soil. Vadose zone journal, 18(1), 1-13. https://doi.org/10.2136/vzj2018.12.0213

6.2 Materials and methods

To obtain an improved picture of the induced polarization of biochar in soil closer to actual field conditions, two series of SIP measurements were conducted on unsaturated samples dried using pressure drainage and evaporation. For the pressure drainage, the joint MSO-SIP system introduced in Chapter 3.3.3 was applied. Three sand samples with pure sand, 1 %, and 2 % additions of biochar PW800 (by weight) were drained by pressure, and SIP measurements were made at different saturation levels. The SIP measurements were fitted with a Cole-Cole model, and the resulting dependence of the DC electrical conductivity, the total chargeability, and the peak relaxation time on saturation will be discussed within the context of previous findings and available mechanistic models for SIP. For evaporation measurements, the rectangular sample holder with a four-point electrode array introduced in Chapter 3.3.4 was applied. Several sets of pure sand samples and samples of sand with 2 % additions of biochar PS (by weight) with different initial water saturation were investigated with time-lapse SIP measurements during evaporation. The results of the evaporation experiments will be compared with those of the MSO measurements. The details of the sample preparation and SIP measurements for the two series of experiments will be introduced in the following sections.

6.3 MSO drainage

6.3.1 Sample preparation and drainage experiment

The complex conductivity of pure sand and two sand-biochar mixtures with 1 and 2 % mass fractions of biochar was investigated as a function of saturation. The key parameters of the materials are briefly repeated here. The particle size of biochar PW800 was 1 - 2 mm. The biochar particles had a skeletal density of about 1.80 g cm^{-3} and a specific surface area per unit mass of 181 m^2 g^{-1}. The used F36 sand had a mean particle diameter of 0.16 mm and a grain density of 2.65 g cm^{-3}. Other parameters are provided in Chapter 3.2.

The SIP measurements on saturated sand-biochar mixtures with PW800 have been presented in Chapter 4 and 5. The saturated sand-biochar mixtures with 2% PW800 showed a relatively strong phase of more than 50 mrad owing to the relatively large pore surface and the presumed noticeable electrical conductivity of the particles expected from the low hydrogen/carbon (H/C) ratio of this biochar. The total normalized chargeability of 0.007 S m^{-1} for an electrolyte conductivity of 0.1 S m^{-1} was comparable with the magnitude expected for semi-conductive materials (Weller et al., 2010).

The preparation of the saturated sand-biochar mixtures proceeded as follows. At first, biochar was immersed in a NaCl electrolyte with an electrical conductivity of 0.045 S m^{-1} for 24 hours before sample preparation, to fully saturate the inner pores of the biochar particles and to avoid the biochar floating during sample preparation. The sand was moistened to a pasty consistence by adding the same NaCl electrolyte and stirring with a spoon. It was then fully mixed with the wet biochar until the biochar particles were well distributed in the sand. Next, the sample material was filled into the measurement cell with a similar wet packing procedure as used by Breede et al. (2011). The material was filled into the sample holder step by step while a layer of NaCl electrolyte was maintained above the sample material. Gentle stirring with a spoon removed air bubbles and avoided zonation leading to a visually homogeneous distribution of the biochar particles. After packing, the resulting porosity (ϕ) was calculated from the volume of the sample holder (V_{tot}), the mass of sand (w_{s}) and biochar (w_{bio}), the skeletal density of biochar (ρ_{bio}), and the grain density of sand (ρ_s) with

$$V_{tot} = \frac{{w_s}/{\rho_s} + {w_{bio}}/{\rho_{bio}}}{1-\phi} = (1-\upsilon)V_{tot} + \upsilon V_{tot} = \frac{w_s}{\rho_s(1-\phi_s)} + \frac{w_{bio}}{\rho_{bio}(1-\phi_{bio})} \tag{6—1}$$

The porosity of the pure sand sample ($\phi = \phi_s$) was 0.40, the porosity of the mixture with 1% biochar was 0.42, and the porosity of the mixture with 2% biochar was 0.44. If it is assumed that this increase in porosity is solely due to the addition of biochar, the equation can be split into individual additive volumes of sand and biochar with the volume fraction of biochar (ν) and the individual porosities of biochar (ϕ_{bio}) and sand (ϕ_s). The porosity of the biochar particles was estimated to be around 0.83 and the volume fractions of the 1 and 2% sand-biochar mixtures were estimated to be 6 and 10%, respectively.

6.3.2 Sample drainage and SIP measurement

After installation of the sample holder in the joint MSO-SIP setup, SIP measurements were first made on the saturated sample. The complex impedance of the sample was measured with the method presented in Chapter 3.4.1. The three samples were then drained in a series of pressure steps. The size of the pressure steps were chosen such that the decrease of saturation between two successive SIP measurements was small. When the outflow was negligible after the application of a pressure step, SIP measurements were made on consecutive days to verify that the sample was in approximate equilibrium. If the difference between the two consecutive SIP measurements was < 2%, the next pressure step was applied. Using this procedure, the entire drainage experiment lasted for around 2 months for each sample. The applied pressure was converted into suction at the bottom of the soil column (matric potential in centimeters). An overview of the applied suctions for the three samples is provided in Tab. 6-1.

Table 6-1. Applied suction steps ($|h|$) and the corresponding saturation values (S_w) for the pure sand and the two sand-biochar mixtures.

Sand		Sand-biochar mixture (1%)		Sand-biochar mixture (2%)	
$\lvert h\rvert$ cm	S_w %	$\lvert h\rvert$ cm	S_w %	$\lvert h\rvert$ cm	S_w %
15	100	20	100	20	100
53	100	41	100	41	100
57	99	49	98	49	98
59	97	51	97	51	98
61	88	53	96	53	95
64	71	56	87	56	87
67	64	58	85	58	78
69	51	60	81	60	77
71	41	62	77	62	73
74	35	64	69	64	62
77	32	66	64	66	54
80	28	68	56	68	47
83	26	71	48	71	40
87	24	74	42	74	36
92	22	80	38	80	32
95	21	82	36	82	31
99	20	87	34	87	29
105	20	92	33	92	27
112	19	97	32	97	26
153	19	102	32	102	26
204	18	112	30	112	25
306	18	122	29	122	25
408	18	173	29	173	24
510	17	224	28	224	23
700	15	306	28	306	23

The water content of the samples as a function of the pressure head, h, obtained from the stepwise drainage of the three samples was fitted with the van Genuchten model for the water retention curve (Van Genuchten, 1980):

$$\frac{\theta(h)-\theta_r}{\theta_s-\theta_r} = (1+|\alpha_{vG}h|^{n_{vG}})^{-m_{vG}} \tag{6—2}$$

where θ_r and θ_s are the residual and saturated soil water content, respectively, α_{vG} is the inverse of the air-entry value, n_{vG} is a shape factor related to the pore size distribution, and m_{vG} = 1-1/n_{vG}. In the case of the sand-biochar mixtures, the water content is described using a simple dual-porosity model with two domains (Šimůnek et al., 2003):

$$\theta(h) = \nu\theta_{bio}(h) + (1 - \nu)\theta_{sand}(h) \qquad (6—3)$$

where $\theta_{sand}(h)$ and $\theta_{bio}(h)$ are the water retention curves of the sand and the biochar, and ν is the volume fraction of biochar in the sand-biochar mixture.

6.3.3 Data interpretation

Measured SIP data were converted to the complex electrical conductivity $\sigma^*(\omega)$ by using the appropriate geometrical factor k of the SIP-MSO set-up (see Chapter 3.4.1). Data pre-processing was also applied for temperature correction and the reduction of electromagnetic coupling (see Chapter 3.4.1). The measured complex conductivities of each measurement were fitted with a Cole-Cole model (Eq. 2-12) using the approach presented in Chapter 5.3.3. The total chargeability M, relaxation time τ_0 (s), and Cole-Cole exponent c_{cc} were derived from this analysis. In the previous chapter, analysis of the Cole-Cole parameters showed that the normalized chargeability M_n of sand-biochar mixtures falls between that of sand-clay and sand-metal mixtures. However, M_n was found to be sensitive to the conductivity of the pore fluid, which is highly variable in agricultural soils where biochar is anticipated to be applied. Therefore, it is preferred to use M instead of M_n in this chapter.

6.3.4 Results and discussion of water retention of sand-biochar mixtures

Fig. 6-1a shows the dependence of the water content, θ, of the sand and the two sand-biochar mixtures on the matric potential during pressure drainage. With increasing suction, the θ of sand showed a steep decrease that started at a matric potential of -55 cm. This initial drainage is associated with the air-entry pressure of the largest pore. In the matrix potential range between -55 and -80 cm, almost the entire pore space was drained. This indicates a narrow pore size distribution as expected for the well-sorted sand used here. Beyond a matric potential of -80 cm, the θ of sand hardly decreased anymore. The water retention curve for sand was adequately described by the van Genuchten model (Fig. 6-1a), and the resulting parameters are provided in Tab. 6-2. These hydraulic parameters for sand are similar to those reported by Bechtold et al. (2012) for a different sample of the same type of sand.

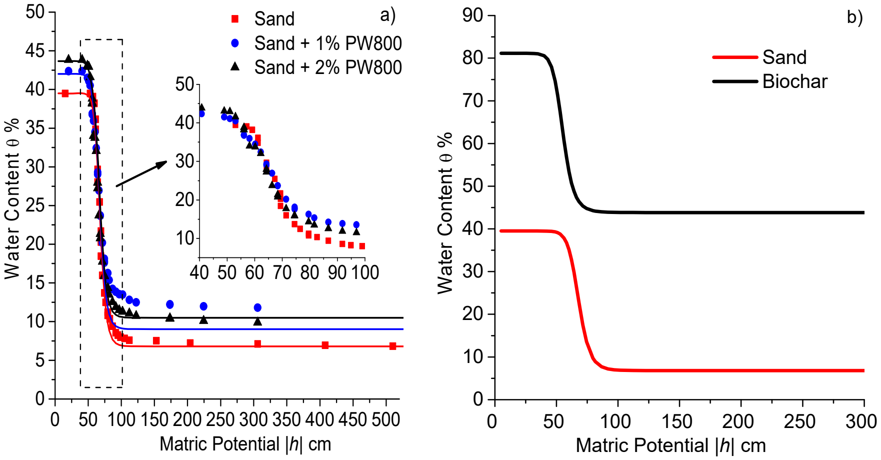

Figure 6-1. Water retention characteristics describing the relationship between water content (θ) and matric potential (h) for pure sand and the two sand-biochar mixtures with 1% and 2% PW800 biochar; (a) measured values and fits according to Eq. (6-2) and (6-3) using the curves from (b) for pure sand and pure biochar; (b) fit for pure sand by Eq. (6-2) and modeled curve for pure biochar according to Eq. (6-2) and (6-3) from the fit for the 2% sample.

Table 6-2. Fitted model parameters for the water retention curve of sand and biochar

	Parameters of the van Genuchten model				
Material	θ_s (%)	θ_r (%)	α_{vG} (cm^{-1})	n_G	m_G
Sand	40	7	0.015	15.4	0.94
Biochar	81	44	0.018	13.0	0.92

The water retention characteristics of the two sand-biochar mixtures showed a relatively similar behaviour as the pure sand. However, the water content of the saturated sand-biochar mixtures was larger than that of the saturated sand, and increased with an increasing amount of biochar. In addition, the water content of the sand-biochar mixtures showed a somewhat earlier decrease around a matric potential of -50 cm, and increasing residual water content due to the addition of biochar. However, it is important to note that the residual water content of the 2% sand-biochar mixture was lower than that of the 1% sand-biochar mixture. This is not consistent with previous work. For example, Głąb et al. (2016) and Amoakwah et al. (2017) both found a positive correlation between the amount of added biochar and the residual water content for most of the investigated samples. Therefore, it was concluded that the sample with 1% biochar showed signs of erroneous data at higher absolute values of matric potential, which will be discussed below.

In a next step, the dual-porosity model was fitted to the measured data of the 2 % sand-biochar mixture using the estimated volume fraction of biochar (10 %). For this, it was assumed that the hydraulic parameters of the sand remained unchanged, and only the hydraulic parameters of the biochar were varied. The resulting hydraulic parameters of biochar are provided in Tab. 6-2, and Fig. 6-1a presents the fit of the dual-porosity model to the experimental data. In addition, Fig. 6-1b shows the estimated water retention curves for pure sand and pure biochar. The fitted hydraulic parameters suggest that the biochar particles are highly porous and have a saturated water content of around 81%. This value is close to the estimated porosity of the biochar particles (83%), which is expected since the saturated water content and porosity estimates were obtained from the same weight data. In addition, the fitted residual water content of the biochar was high with 44%, indicating a significant micro-porosity that remains saturated even for high matric potentials. In addition, the air entry pressure was found to be lower (higher α_{vG}) and the pore size distribution somewhat broader (lower n_{vG}) for biochar than for sand. This explains the broader range of pressures with significant drainage of the sand-biochar mixtures. These findings can be summarized with the conceptual model presented in Fig. 6-2, which is well supported by the available literature on biochar (Bikbulatova et al., 2018).

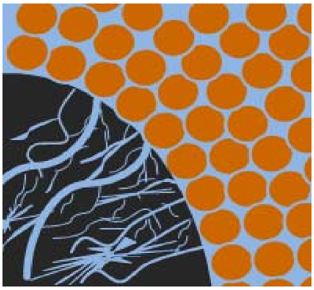

Figure 6-2. Conceptual illustration of different types of porosity present in sand-biochar mixtures. Orange indicates sand particles that result in a relatively narrow pore size distribution, whereas the black area indicates biochar with a heterogeneous pore size distribution with both large and small pores.

Fig. 6-2 shows a biochar particle with large and small pores surrounded by spherical sand particles with relatively uniform large pores between them. The radius r_{min} of the smallest pores, which can be drained at a matric potential of $h = -300$ cm (i.e. the maximum suction applied to the sand-biochar mixtures), can be calculated from the Young-Laplace equation:

$$r_{min} = \frac{2\gamma cos\vartheta}{\rho_w g h} \qquad (6—4)$$

Using this equation, a radius of 4.9 µm was obtained with the surface tension of water $\gamma = 0.0727$ kg s^{-2}, the density of water $\rho_w = 1000$ kg m^{-3}, the gravitational acceleration constant $g = 9.81$ m s^{-2}, and a wetting angle $\vartheta = 0°$ (complete wetting). For wetting angles larger than 0, which is rather probable for biochars, smaller radii would be obtained. This pore size matches well with the characteristic pore size of biochars measured by mercury intrusion (Lu and Zong, 2018).

The previous results are based on the analysis of the results for the 2% sand-biochar mixture. The predicted water retention curve for the 1% sand-biochar mixture using the hydraulic parameters in Tab. 6-2 and the estimated volume fraction of biochar (6%) are also provided in Fig. 6-1a. For low matric potentials, the predicted water content matched the measured water content relatively well, but the quality of the fit deteriorated for higher matric potentials. It is important to note that the measured residual water content at high matric potential even is underestimated when it is assumed that the biochar particles remain fully saturated throughout the drainage experiment. Therefore, it was concluded that the measured water retention curve for the 1% sand-biochar mixture is not physically plausible, and that these data should be used with care when they are used to analyse the relationship between complex electrical conductivity and saturation. The physically implausible results are attributed to an unidentified error in the outflow measurements for the 1% sand-biochar during drainage (e.g. undetected leakage, calibration drift in the pressure transducer used to measure water outflow). In order to not fully discard the complex electrical conductivity measurements for the 1% sand-biochar mixture, the saturation of the 1% sand-biochar mixture was estimated from the modelled instead of the measured water retention curve in the following. Obviously, this is a very crude approximation and therefore the following results for the electrical measurements on the 1% sand-biochar mixture can only be interpreted in a qualitative manner.

6.3.5 Results and discussion of SIP measurements during pressure drainage

The measured frequency-dependent complex electrical conductivity of the sand and sand-biochar mixtures for varying water saturation is presented in Fig. 6-3 for frequencies between 1 mHz and 1 kHz. Data for higher frequencies were not considered because of the increasing importance of capacitive errors with increasing desaturation (Huisman et al., 2016). In a first step, the DC electrical conductivity (σ_0) determined by fitting a Cole-Cole model to the SIP data will be interpreted as a function of saturation. As expected, σ_0 decreased with decreasing water saturation (Fig. 6-5). For homogeneous samples like the sand sample used in this study, the σ_0 of a porous media can be described by the following relationship derived by Linde et al. (2006):

$$\sigma_0 = \frac{1}{F}\sigma_w S_w^{n_1} + \left(\frac{F-1}{F}\right)\sigma'_{surf} \qquad (6—5)$$

$$F = \phi^{-m_1} \qquad (6—6)$$

where F is the formation factor, ϕ is porosity, m_1 is the cementation exponent, σ_w is the conductivity of the pore electrolyte, n_1 is the saturation exponent, and σ'_{surf} is the real part of the surface conductivity. This model ignores deviations that occur when approaching the percolation threshold (Jougnot et al., 2010), which is expected to be situated at very low saturation for sand. It was able to fit the data for sand reasonably well with the water conductivity used for sample preparation (0.045 S m^{-1}) (Fig. 6-4). The fitted model parameters for sand were $F = 3.75$, $m_1 = 1.42$, $n_1 = 2.27$, and $\sigma'_{surf} = 3.92 \times 10^{-15}$ S m^{-1}. This latter low value for σ'_{surf} is a result of the fitting procedure and just indicates negligible surface conductivity for the pure sand. The formation factor F matches well with a previously reported value for a similar sand (Breede et al., 2011), and the saturation exponent n_1 falls within the range determined by Ulrich and Slater (2004).

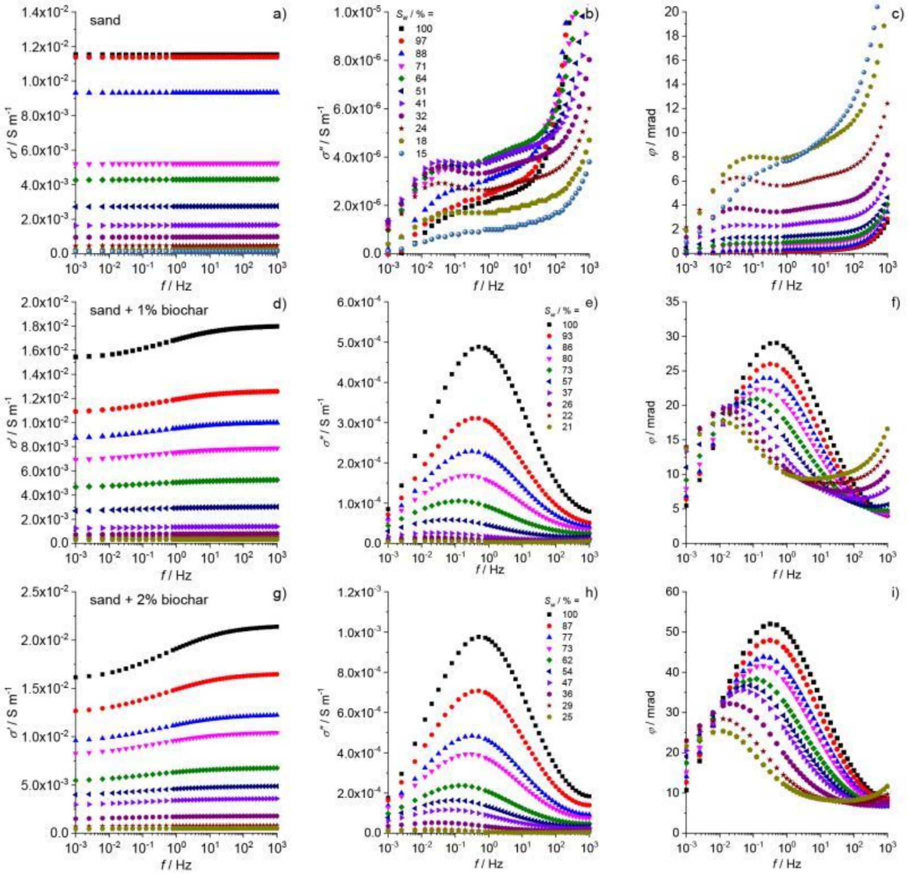

Figure 6-3. SIP measurements on pure sand (top row), 1% sand-biochar mixture with PW800 (middle row), and 2% sand-biochar mixture with PW800 (bottom row) for a range of saturation. SIP measurements are presented as the real part of the electrical conductivity σ' (left column), the imaginary part of the electrical conductivity σ'' (middle column), and the phase of the electrical conductivity φ (right column).

The relationship between σ_0 and S_w of the sand-biochar mixtures was different from that of sand in two aspects. First, σ_0 at full saturation increased with increasing amount of biochar although the conductivity of the water used for sample preparation was identical. Second, the relationship between log (σ_0) and log (S_w) was found to be non-linear for the sand-biochar mixtures, especially in the low saturation range (Fig. 6-4). Sen (1997) showed that models such as those presented in Eq. 6-5 do not apply for heterogeneous samples with micro- and macro-porosity. In particular, the water contained in the micropores may become disconnected when the large pores are drained, and therefore contribute less to the bulk conductivity. For such cases, Sen (1997) argued that the mixing model of Maxwell (1873) can be used if the volume fraction of the inclusions is below the percolation threshold (~18%), which is valid for the sand-biochar mixtures investigated here. Therefore, the following model based on Maxwell (1873) is used to calculate the σ_0 of unsaturated sand-biochar mixtures (Sen, 1997):

$$\sigma_0 = \sigma_s \frac{2\sigma_s + \sigma_{bio} - 2\,v_{bio}(\sigma_s - \sigma_{bio})}{2\sigma_s + \sigma_{bio} + v_{bio}(\sigma_s - \sigma_{bio})} \qquad (6—7)$$

with

$$\sigma_s = \sigma_w S_{w_s}^{n_s} \phi_s^{m_s} \qquad (6—8)$$

$$\sigma_{bio} = \sigma_w S_{w_{bio}}^{n_{bio}} \phi_{bio}^{m_{bio}} \qquad (6—9)$$

where σ_s and σ_{bio} are the saturation-dependent electrical conductivity of the sandy host media and biochar, respectively, v_{bio} is the volume fraction of the biochar particles, σ_w is the water conductivity, S_{wi} is the water saturation, n_i is the saturation exponent, m_i is the cementation exponent, ϕ_i is the porosity, and the subscript i can either be s for the sandy host medium or *bio* for the biochar particles.

For the sand-biochar mixtures, σ_0 as a function of S_w predicted by Eq. 6-7 to 6-9 was compared with the available measurements. S_{ws} and S_{wbio} were calculated from the obtained water retention curves (Fig. 6-1b and Tab. 6-2) for each of the applied pressure steps (Tab. 6-1). The values of m_s and n_s for the sand fraction were assumed to be equal to the fitted values of m_1 and n_1 from the model of Linde et al. (2006) that were obtained for the pure sand sample. This seems a reasonable approximation because of the relatively low volume fraction of biochar. It was also assumed that σ_w was equal to the electrical conductivity of the water used for sample preparation. Finally, the values of

n_{bio} and m_{bio} were not known. The saturation exponent was set to the widely used value of 2 following the original work by Archie (1942). The cementation exponent was also set to the value of 2. This is the lower limit for cementation exponent found by Fang et al. (2018) for coal using gas diffusion measurements. The model showed a reasonable fit to the measured σ_0 for the 2 % sand-biochar mixtures (Fig. 6-4b). In particular, the nonlinearity in the log-log representation of the data is well captured. However, the model seems to underestimate σ_0 for the entire range of saturation. This is at least partly related to a probable underestimation of σ_w due to a release of adsorbed ions from the biochar during sample preparation. The fit to the measured data could be slightly improved by fitting σ_w to the measured data (result not shown), which resulted in a value of σ_w = 0.055 S m^{-1} instead of the value of 0.045 S m^{-1} for the 4 mM NaCl solution used during sample preparation. This is an increase of 22%. In previous work, σ_0 was found to be 0.0140 S m^{-1} for a sample with the same composition and similar porosity when it was flushed with 4 mM NaCl solution. The value of σ_0 at full saturation determined in this study was 14% larger. The model fit to the measurements of the 1% sand-biochar mixture is shown in Fig. 6-4a. Clearly, the model fit is of much lower quality, which is attributed to the considerable uncertainty in the saturation of this sand-biochar mixture as explained in the previous section.

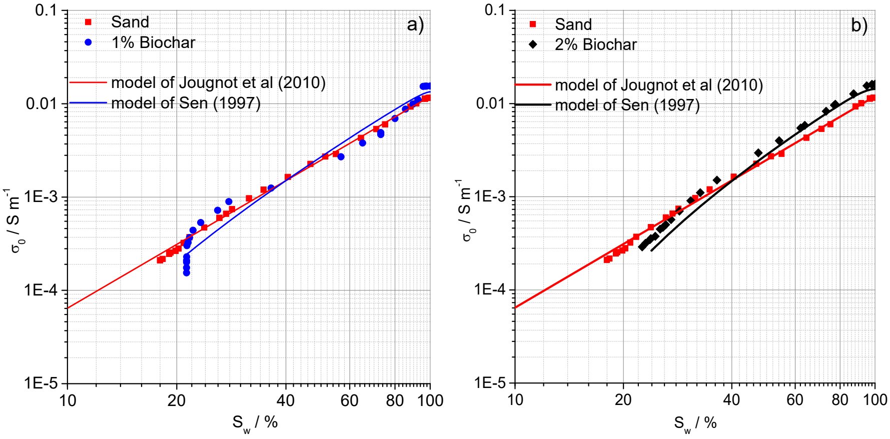

Figure 6-4. Direct current conductivity σ_0 as a function of saturation S_w for a) sand and the 1% sand-biochar mixture with PW800 and b) sand and the 2% sand-biochar mixture with PW800. The solid red line indicates the model predictions using the model of Linde et al. (2006) for sand and the blue and black lines indicate the model predictions using the model of Sen (1997) for sand-biochar mixtures.

In a next step, the $\sigma''(\omega)$ and the parameters M and c_{cc} derived from the fitted Cole-Cole models were analysed. The $\sigma''(\omega)$ and $\varphi(\omega)$ of sand showed a weak maximum in the low-frequency range around 0.01 ~ 0.1 Hz for partially saturated conditions and a strong increase in the high-frequency range with desaturation (Fig. 6-3b and c). The $\sigma''(\omega)$ in the mHz to Hz frequency range first increased and then decreased with decreasing water saturation. The maximum value for $\sigma''(\omega)$ in this frequency range was obtained for a water saturation of around 45%. These results for sand agree well with the results of Breede et al. (2012), who used similar sand and the same experimental method. Breede et al. (2012) proposed a conceptual model to explain how desaturation affects the SIP spectra of sand based on the short-narrow pore model (Titov et al., 2004). Their explanation suggests that the grain contact areas act as the short-narrow pore at full saturation. With increasing desaturation, the large inter-grain pores which are the dominant pathway of electrical current for the saturated sample release water while the grain contact regions remain wet. Therefore, the remaining water films around the particle become the narrow pores that connect the thicker water films at the grain contact areas for electrical current flow. This results in a decrease of the ohmic conductivity and an increase of polarization. With progressing drainage, the difference in thickness between the water films in the grain contact area and around the particles decreases, therefore, both the magnitude and phase of $\sigma^*(\omega)$ decrease. The increase of $\sigma''(\omega)$ and $\varphi(\omega)$ for frequencies above 100 Hz is related to the increasing contact impedance of the potential electrodes with decreasing saturation (Huisman et al., 2016), and to Maxwell-Wagner polarization of the porous media (Breede et al., 2012).

The shape of the measured $\sigma'(\omega)$ and $\sigma''(\omega)$ is similar for the mixtures with 1% biochar (Fig. 6-3d and 6-3e) and 2% biochar (Fig. 6-3g and 6-3h). The $\sigma'(\omega)$ increased with increasing frequency and approached a plateau. The increase in conductivity with frequency was stronger for the sand-biochar mixture with 2% biochar than for the mixture with 1% biochar. Accordingly, a peak was found in $\sigma''(\omega)$ and $\varphi(\omega)$, which is consistent with the Kramers-Kronig relationship that describes the coupling between $\sigma'(\omega)$, $\sigma''(\omega)$ and $\varphi(\omega)$ (Toll, 1956).

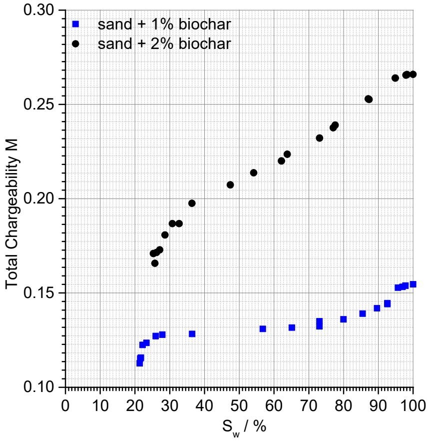

Figure 6-5. Total chargeability (M) as a function of saturation (S_w) obtained by fitting a Cole-Cole model to spectral induced polarization (SIP) data for the 1 % and 2 % sand-biochar mixture with PW800.

The modelling parameters M and c_{cc} as a function of saturation are presented in Fig. 6-5 and 6-6 for the two sand-biochar mixtures. The M values obtained for the 1 % and 2 % sand-biochar mixtures ranged from 0.11 - 0.16 and 0.16 - 0.28, respectively. In addition, M decreased continuously with decreasing saturation as expected from the decreasing size of the peak in $\sigma''(\omega)$ (Fig. 6-3f and 6-3i). It decreased fast between 95 % and 75 % and thereafter decreased slower until a water saturation of 40 %. In the low-saturation range, the decrease in M with decreasing saturation became faster again. The fitted c_{cc} values for the two sand-biochar mixtures varied slightly between 0.34 and 0.43 and were slightly less than those found by Maineult et al. (2018) using pore network modelling. In contrast with the results of Maineult et al. (2018), c_{cc} decreased with desaturation (Fig. 6-6) for our samples, which reflects the increasing influence of the background of the matrix. Again, the behaviour of the 1 % sand-biochar mixture should be interpreted with care due to the uncertainty in the saturation.

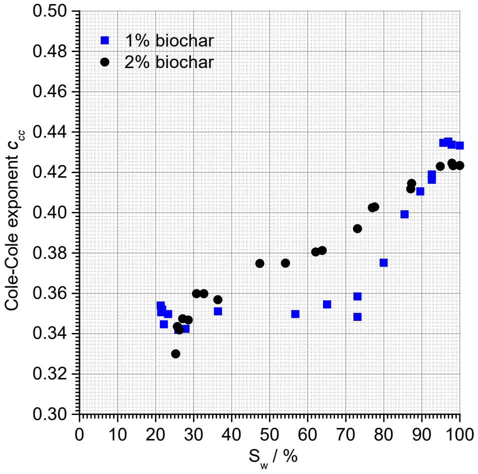

Figure 6-6. Cole-Cole exponent (c_{cc}) as a function of saturation (S_w) obtained by fitting a Cole-Cole model to spectral induced polarization (SIP) data for the 1% and 2% sand-biochar mixture with PW800.

The polarization of the sand-biochar mixture can also be interpreted by applying the mixing model presented in Eq. 6-7 in principle for the whole frequency range (e.g., see the reformulated Eq. 13 in Revil et al. (2015b)). In the simple case of a non-draining conductive particle in a non-polarizing sand background, it can be shown that the chargeability will decrease with decreasing saturation (i.e., decreasing electrical conductivity). The same trend can also be seen from the measurements with variable water electrical conductivity but the same amount of biochar presented in Chapter 4. However, a more quantitative analysis using mixing models is currently hampered by the need to estimate $\sigma^*(\omega)$ as a function of saturation for both the sand and the biochar fraction. In qualitative terms, it is observed that the drainage of the large pores led to an initially strong decrease in the chargeability in the high saturation range, which may be explained by the loss of continuity in the water film within and around the particles of biochar. With increasing desaturation, the polarization of the sandy host media is increasing while the polarization of the biochar further decreases. This opposite behaviour becomes significant when $\sigma''(\omega)$ of the sand-biochar mixtures decreases to a comparable order of magnitude as the sand. This may explain the reduced decrease of chargeability for intermediate saturations between 75% and 40%. With progressing drainage, the polarization of sand starts to decrease, resulting in a stronger decrease in the polarization of the sand-biochar mixtures.

In a final step, the dependence of the relaxation time (τ_0) on saturation was analysed. Fig. 6-3 indicates that the peak frequency shifted to lower frequencies with decreasing saturation for both sand-biochar mixtures. The τ_0 derived from fitting the Cole-Cole model is presented in Fig. 6-7 as a function of S_w. It was found that the τ_0 increased with decreasing saturation, which is the opposite direction as observed for unsaturated sand without conductive particles (Breede et al., 2012) and modelling results on pore networks without conductive particles (Maineult et al., 2018). The values for τ_0 varied from 0.3 s for saturated sand-biochar mixtures to around 20 s for sand-biochar mixtures with a saturation of 0.26. The sand-biochar mixtures with 2% biochar showed a linear relationship between $\log(\tau_0)$ and $\log(S_w)$ with a slope of -3.17, whereas the sand-biochar mixtures with 1% biochar showed a somewhat nonlinear relationship but the same general trend.

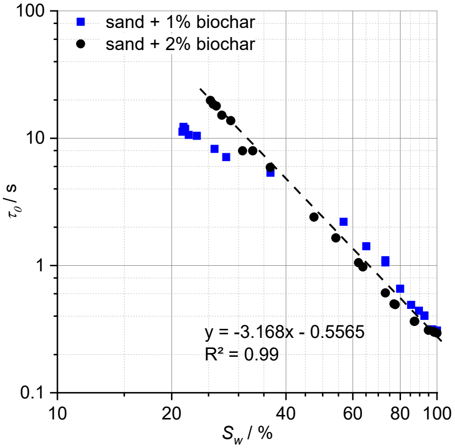

Figure 6-7. Relaxation time (τ_0) as a function of saturation (S_w) obtained by fitting a Cole-Cole model to spectral induced polarization (SIP) data for the 1% and 2% sand-biochar mixture with PW800.

In a range of studies, τ_0 was described as a function of particle size d and a diffusion coefficient D (Gurin et al., 2015; Leroy et al., 2008; Revil et al., 2015b; Schwarz, 1962):

$$\tau_0 \propto \frac{d^2}{D} \qquad (6-10)$$

As introduced in Chapter 2, D is the diffusion coefficient of the counter-ions in the Stern layer (Leroy et al., 2008; Schwarz, 1962), the diffusion coefficient of charge carriers inside the conductive particle (Revil et al., 2015b), or the apparent diffusion coefficient of the charge carriers responsible for the polarization dependent on both the particle mineralogy and surface chemistry (Gurin et al., 2013). In the case of the sand-biochar mixtures, the increasing τ_0 with decreasing saturation can potentially be explained by a decrease of the apparent diffusion coefficient of ions due to desaturation of the biochar particles. Kastening and Heins (2005) reported that the ionic diffusion coefficient in micropores of active carbon is about one order of magnitude smaller than in the macropores due to restricted movement within the strongly overlapping EDL of opposing pore walls and the surface chemical properties of active carbon. It should also be noted that the peak frequency of $\varphi(\omega)$ of the sand-biochar mixtures approached that of the pure sand for low saturation (Fig. 6-3), which might suggest that the polarization of biochar is very weak at low saturation.

In previous chapters, it was found that $\varphi(\omega)$ and M mainly depend on the amount of biochar, and that τ_0 depends on the particle size of biochar and on the electrical conductivity of the water in the porous media in the case of saturated sand-biochar mixtures. The relationships found for saturated conditions were consistent with measurements (Placencia-Gomez and Slater, 2016; Revil et al., 2015a) and modeling (Gurin et al., 2015; Revil et al., 2015b; Wong, 1979) of porous media with conductive particles. In the case of unsaturated sand-biochar mixtures, the highly porous nature of biochar played an important role in understanding the experimental results. The water retention curves of the sand-biochar mixtures were interpreted using a dual-porosity model, and it was found that the biochar particles have a macroporosity that drained in a similar pressure range as the sand and a relatively large microporosity that remained saturated in the pressure range considered in this study. At high suction, biochar particles with a considerable amount of residual water were dispersed in a dry sand background. This resulted in a nonlinear dependence of $\sigma'(\omega)$ on saturation in a log-log representation that could be described with a dielectric mixing model of Maxwell (1873). The drainage of the biochar particles probably also explains the steep decrease of $\varphi(\omega)$ and M and the continuous increase of τ_0 with decreasing saturation.

6.4 Evaporation

6.4.1 Sample preparation

The evaporation experiment with time-lapse SIP measurements was conducted at the beginning of this study and was initially designed as a preliminary experiment to verify the equipment and measurement strategy. For this reason, the biochar PS was used (Chapter 3), which was only available in a limited amount and was not characterized well in terms of the relevant physical and chemical properties. In the end, it was nevertheless decided to include the results of this experiment in this thesis. The application of biochar made from pyrolysis of paper mill sludge for agricultural or environmental purposes is interesting because of the potential to reduce the pollution of the paper industry while contributing to carbon capture and sequestration efforts (Van Zwieten et al., 2010). It is thus meaningful to investigate how the SIP spectra for mixtures with this biochar develop in unsaturated condition to support possible non-destructive SIP monitoring of biochar in the field. In addition, a qualitative comparison between the effects of drainage and evaporation is possible even though this biochar is less characterized.

In contrast to the samples used in the MSO-SIP set-up that were wet-packed and thus saturated at the beginning, samples for evaporation were unsaturated initially. To prepare each of the unsaturated samples, known amounts of dry material and water were used for each sample. The amount of water was selected to obtain an initial saturation in a range from 30 % to 90 % with steps of 10 % difference for each packing. Because of a varying amount of evaporation during sample preparation, the actual value of initial saturation of each sample showed considerable deviations from the expected value. Therefore, the initial saturation was determined based on the weight of water and the pore volume of solid material after sample preparation.

To prepare the samples, dry materials with known mass fraction (i.e. 98% sand, 2% biochar) were put into a plastic box. The sample material was then slightly moistened with 4 mM NaCl solution to increase cohesion and then mixed until a visually homogeneous distribution of biochar particles was achieved. During mixing, the rest of the predetermined amount of solution was added to the mixture step by step. After this, the sand-biochar mixture was filled into the box-shaped sample holder (see Chapter 3.3.4). The distance between the surface of the mixture and the top edge of box was measured to determine the sample height in the box. As the surface of the solid materials was not fully flat despite manual leveling, the expected error of this height determination is estimated to be ~10 %. After sample preparation, a cover was placed at the surface of the mixture to keep the evaporation rate at the surface low and the distribution of water content inside the mixture relatively even. With the known size of the box and the known spacing between the electrodes, the geometrical factor k of the four-point electrode arrangement was obtained (see Chapter 3.4.1). It was also used to obtain the volume of material V for the calculation of saturation and porosity. A box with pure sand with approximately the same saturation was also prepared as a reference using the same procedure.

The used dry materials (i.e. sand and biochar), the empty box used for mixing, and the sample holder before and after sample preparation were weighed. The mass of the water solution w_w in the samples was obtained by subtracting the weight of dry material from the increase of weight of the box after sample preparation. Using a water density of ρ_w = 0.998 g cm^{-3}, the volume of aqueous solution was obtained by $V_w = w_w / \rho_w$. With the measured volume of materials V and the calculated porosity ϕ, the initial saturation S_0 for each of the samples was obtained by:

$$S_0 = \frac{V_w}{V\phi} \qquad (6—11)$$

Each set of samples (i.e. the reference of sand sample and the sand-biochar mixture) were measured several times with irregular time intervals until they were dry. After this, the pair of boxes was cleaned and filled with the next set of samples. This packing procedure was repeated six times with different amounts of solution and the same amount of solid materials, which resulted in a range of initial saturations for different samples (Tab. 6-3). The porosity of pure sand samples was similar for all samples. The porosity of the sand-biochar mixtures varied between 0.43 and 0.46, which is attributed to insufficient reproducibility of the mixing process.

Table 6-3. Initial saturation and porosity of each set of samples.

Sand			Sand-biochar mixtures		
Sample Set&No.*	Initial Saturation S_0 / %	Porosity	Sample Set&No.*	Initial Saturatio S_0 / %	Porosity
S1	40	0.41	S+PS1	36	0.45
S2	47	0.41	S+PS2	41	0.44
S3	67	0.41	S+PS3	53	0.46
S4	75	0.41	S+PS4	66	0.44
S5	91	0.41	S+PS5	76	0.46
S6	92	0.41	S+PS6	83	0.43

*S means pure sand sample. S+PS means sand-biochar mixture of sand and 2% biochar PS. No. refers to each pair of sample sets.

6.4.2 SIP measurements and saturation determination

The SIP measurements were conducted using the method described in Chapter 3.4.1. Since the surface of the sample holder was not completely sealed and the bronze electrodes on both ends of the sample were porous, water evaporated continuously after packing and the mass of the box decreased with time. Because one SIP measurement lasted for about 2.5 hours, the desaturation during each of the SIP measurements could not be ignored. Therefore, the box was weighed before and after each SIP measurement to obtain the weight (w'). From the initial mass of the filled box before the first SIP measurement (w_0), the amount of aqueous solution used in the sample (w_w) and the initial saturation (S_0), the saturation of the samples for each SIP measurement (*S'*) was obtained by

$$S' = S_0 \frac{w_w - (w_0 - w')}{w_w} \qquad (6—12)$$

where w_0- w' is the mass loss of water, and w_w - ($w_0 - w'$) is the remaining water in the box. SIP measurements and weighing were conducted once or twice per day. The SIP measurements on each set of samples lasted for about 1 week until the mass of the sample holder did not decrease anymore. In between measurements, the boxes of sand and sand-biochar mixture were stored close to each other under the same conditions of evaporation.

6.4.3 Effect of evaporation on real part of the complex conductivity

The $\sigma'(\omega)$ of two pairs of samples (No. 2 and 3 in Tab. 6-3) are shown in Fig. 6-8. These two samples are representative for the general behaviours of all samples. As expected, σ' decreased with decreasing water saturation. The SIP measurement was made from the highest frequency to the lowest frequency and then back to high frequencies. Because most of the acquisition time is spent at low frequencies (0.001 to 0.1 Hz), a drop in σ' due to desaturation can be observed at these frequencies. For frequencies above 1 Hz, the frequency dependence of σ' was too small to be visible in Fig. 6-8, suggesting that evaporation was negligible in this short time span. The two values of the saturation *S'* obtained by weighing just before and after the SIP measurement can thus be assigned to the high-frequency part of each separate half of the SIP measurement.

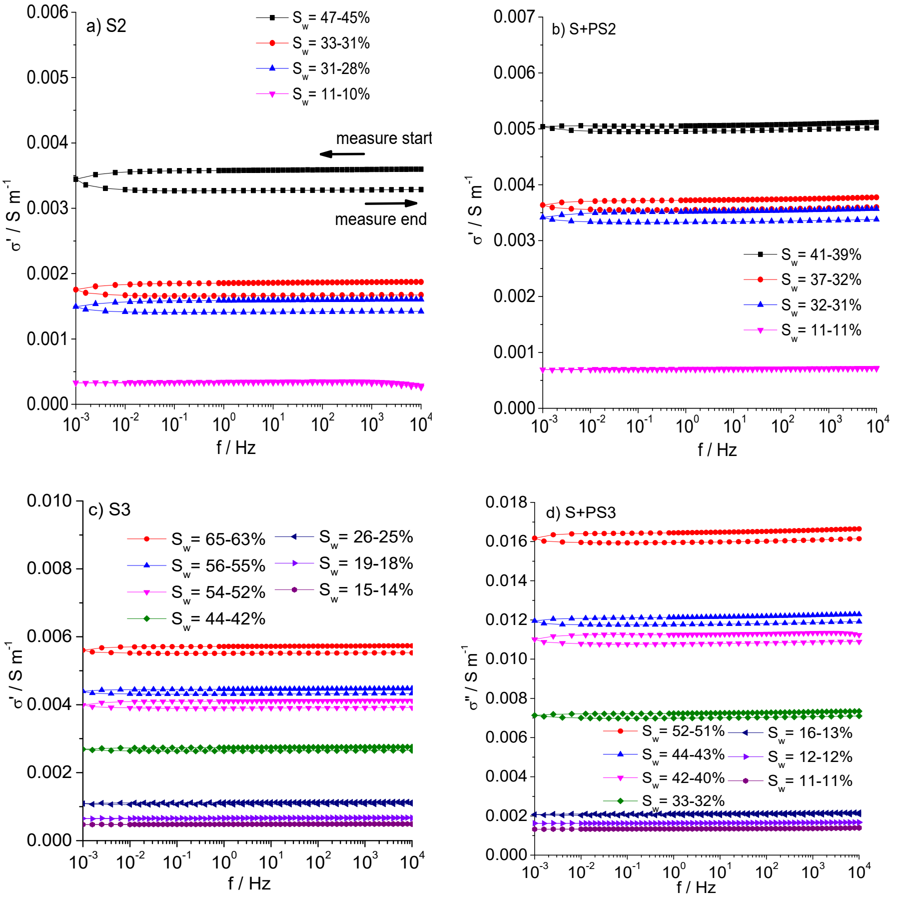

Figure 6-8. Frequency-dependent real part of the complex electrical conductivity (σ') of sample set S2 (top row) and sample set S3 (bottom row). S indicates a pure sand sample. S+PS indicates a sand-biochar mixture with 2 % biochar PS.

To better understand the relationship between saturation and the electrical conductivity of the measured samples, a simplified form of Archie's law (Archie, 1942) was used to fit the measured σ':

$$\sigma'_{10} = b_{ev} S_w^{n_{ev}} \qquad (6-13)$$

where σ'_{10} (S m^{-1}) is the measured σ' at 10 Hz, n_{ev} is the saturation exponent, and the coefficient b_{ev} (S m^{-1}) includes the information about the porosity and the electrical conductivity of the pore water. The subscript *ev* refers to evaporation. This model fitted the σ' well for both sand and sand-biochar mixtures (Fig. 6-9) using the parameters provided in Tab. 6-4. One data set of sand with low saturation (No. S1) was not fitted because of an obvious error in the SIP measurement, which was probably caused by a bad connection between sand and electrodes when the sample was very dry.

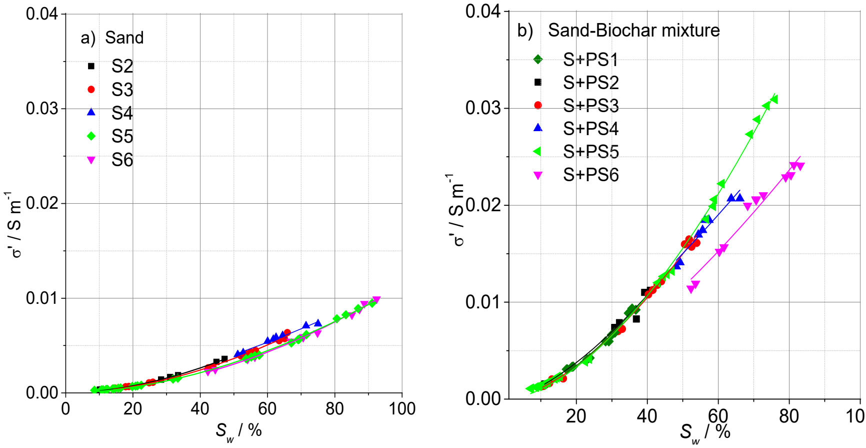

Figure 6-9. Measured real part of the complex electrical conductivity σ' at 10 Hz as a function of water saturation S_w and fitted curves of the simplified Archie's law; a) pure sand samples, b) sand-biochar mixtures with 2 % biochar PS.

Table 6-4. Comparison of the fitting results of different sets of samples with varying initial saturation.

Sample Set&No.*	Sand			Sample Set&No.*	Sand-biochar mixtures		
	S_0 / %	b_{ev}	n_{ev}		S_0 / %	b_{ev}	n_{ev}
S1	40	-	-	S+PS1	36	0.049	1.653
S2	47	0.014	1.813	S+PS2	41	0.043	1.504
S3	67	0.013	1.823	S+PS3	53	0.046	1.604
S4	75	0.012	1.529	S+PS4	66	0.037	1.294
S5	91	0.011	1.822	S+PS5	76	0.050	1.690
S6	92	0.012	1.921	S+PS6	83	0.033	1.522

In general, the σ'_{10} of the sand-biochar mixtures (Fig. 6-9b) was considerably higher than the σ'_{10} of the pure sand (Fig. 6-9a). This is at least partly related to the release of ions from the biochar, which increased the ionic concentration of the pore water solution and thus the real part of the conductivity. A larger b_{ev} and a lower n_{ev} were obtained for the sand-biochar mixtures (Tab. 6-4). It should be noted that these fitted coefficients are not straightforward to interpret. They are not directly comparable to the true coefficients in Archie's law (Archie, 1942), because evaporation will increase the electrolyte concentration and the electrical conductivity of the pore water solution during desaturation. The sample S+PS6 deviates from the other samples, and shows a generally lower electrical conductivity. This is attributed to an error in the preparation of the electrolyte solution.

6.4.4 Effect of evaporation on imaginary part of the complex conductivity

The measured $\sigma''(\omega)$ for the same two representative samples (No. 2 and 3 in Tab. 6-3) is shown in Fig. 6-10. The σ'' of sand showed a slight increase with frequency (Fig. 6-10a). The $\sigma''(\omega)$ for the corresponding sand-biochar mixture increased more strongly with frequency (Fig. 6-10b and d). However, the $\sigma''(\omega)$ for sand and sand with PS biochar was in the same order of magnitude, which was about two orders of magnitude smaller than the $\sigma''(\omega)$ for PW800 at a similar saturation (Fig. 6-3). This indicates that the PS biochar is a material that has low polarization, which is only somewhat stronger than the polarization of pure sand.

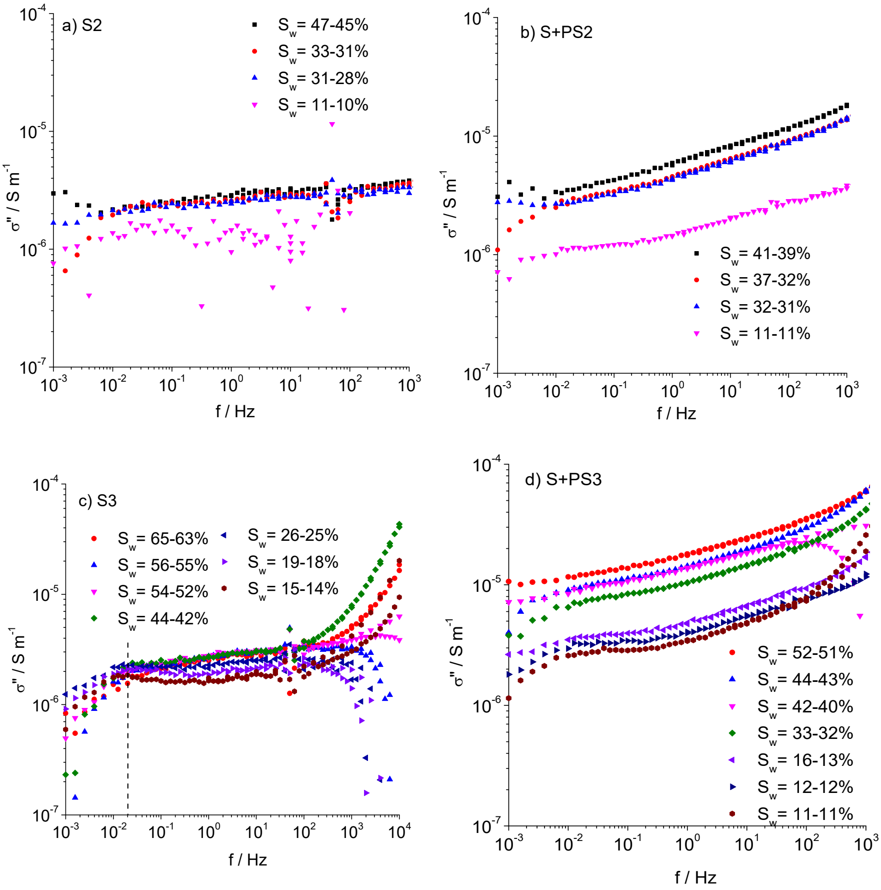

Figure 6-10. Frequency-dependent imaginary part of the complex electrical conductivity (σ'') of sample set S2 (top row) and sample set S3 (bottom row). S indicates pure sand samples. S+PS indicates sand-biochar mixture with 2 % biochar PS. Obvious noise can be observed at around 50 Hz for some measurements, which was caused by the presence of other power sources (AC 230 V/50 Hz).

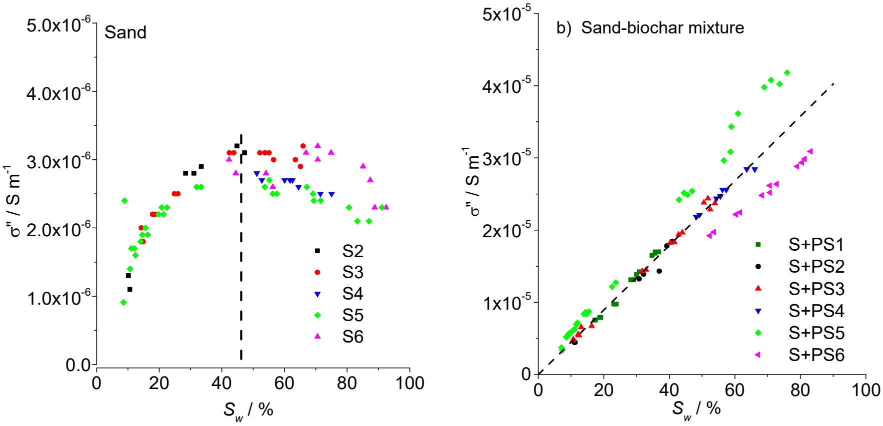

Figure 6-11. Measured imaginary part of the complex electrical conductivity σ'' at 10Hz as a function of water saturation S_W; a) pure sand sample, b) sand-biochar mixture with 2 % biochar PS. Please note that the scale of the Y-axis of panel b) for biochar is one order of magnitude larger than that of panel a) for sand.

The $\sigma''(\omega)$ for both sand and sand-biochar mixtures showed a dependence on saturation (Fig. 6-10). Again, $\sigma''(\omega)$ at 10 Hz (σ''_{10}) was selected as a representative frequency to further study the relationship between $\sigma''(\omega)$ and water saturation S_w (Fig. 6-11). In general, the σ''_{10} of sand-biochar mixtures was larger than that of sand because of the polarization of PS biochar, especially in the high saturation range. For sand (Fig. 6-11a), σ''_{10} increased with decreasing saturation, reached a maximum at a saturation around 45 %, and then decreased with further desaturation. This is consistent with the previous findings for the MSO sample in section 6.3.4 and with the results of Breede et al. (2012). The σ''_{10} for the sand-biochar mixtures (Fig. 6-11b) showed a linear relationship with saturation with a relative constant slope and an intercept close to zero. The deviation for sample S+PS6 is again attributed to a lower electrolyte concentration as explained earlier. The larger values for sample S+PS5 could be caused by a larger biochar fraction in the sample, which is partly supported by the relatively high porosity (Tab. 6-3). The results for the drainage of a sand-biochar mixture with PW800 (Fig. 6-5) showed a M-S_w relationship with a relatively large intercept and a flat slope when S_w was above around 30-40 %, but a higher slope below this critical S_w. In addition to the obvious reason that two different biochars were used, the differences between the two desaturation methods may be affected by the increasing electrolyte concentration during the evaporation. The results presented in Chapter 4 suggest that an increasing pore water electrical conductivity will lead to an increase of the polarization at least at full saturation. To investigate the differences between saturation methods in more detail, future studies should investigate the effect of drainage and evaporation on the SIP response for the same type of biochar. In addition, it may be helpful to investigate how the imaginary part of the electrical conductivity of sand-biochar mixtures depends on the pore water electrical conductivity for unsaturated conditions.

6.5 Conclusions

The SIP response of sand-biochar mixtures is larger than that of sand in unsaturated conditions, independent of the method used for desaturation (i.e. drainage or evaporation). The polarization of the sand-biochar mixtures approaches that of sand with decreasing water content, but the difference can still be well quantified at low saturation, allowing the distinction of soil with and without biochar. For the biochar types used in this study, the effect seems to be large enough to be also quantified in real soil, but this needs to be investigated in more detail. The characteristics of the spectral response of biochar in sand at varying water content can potentially be used to discriminate spatial variation of biochar and water content in field experiments.

7. Conclusions and outlook

In this chapter, the general conclusions from this work will be presented first. The thesis will end with an outlook for future research based on these conclusions.

7.1 Conclusions

Biochar is a promising material for addressing some pressing agricultural and environmental issues. However, its long-term impact on soil properties is largely unknown and the control of biochar in soil is hindered because of the limited methods for its detection and monitoring. Spectral induced polarization (SIP) has potential for such detection and monitoring due to its sensitivity to porous media properties and the presence of electrically conductive inclusions, as well as the ability for field applications. Considering the complexity of the physical and chemical properties of biochar, more research is needed to understand the SIP response of biochar. Therefore, the overall aim of this thesis was to investigate how the SIP response of soil with biochar depends on both biochar and soil properties. To address this aim, three sub-objectives were formulated.

The first sub-objective was to determine the sensitivity of SIP to the presence of different types of disseminated biochar in saturated sand. To address this sub-objective, Chapter 4 presents systematic SIP measurements on four types of biochar in saturated sandy media. The measured SIP data were evaluated by Debye decomposition to obtain values for the peak relaxation time τ_{peak}, the total chargeability M, and the normalised total chargeability M_n. The sensitivity of the SIP response to various types of biochar, mass fraction, particle size of biochar, and electrolyte concentration were investigated. It was found that SIP showed a clear and differentiated response to the presence of all four types of biochars. Two types of biochar derived from gasification and pyrolysis of pine wood, PW700 and PW800, showed significantly stronger polarization. They exhibited a larger imaginary part $\sigma''(\omega)$ and phase $\varphi(\omega)$ of the measured complex electrical conductivity compared with sand and the other two types of biochar derived from beech wood by pyrolysis (BW550) and from miscanthus through hydrothermal carbonisation (HTC). The M was found to be proportional to the mass fraction of biochar, although relationships varied for each type of biochar. The τ_{peak} increased with increasing particle size of the biochar. Increased electrolyte concentration enhanced the normalized chargeability M_n for all biochars, although again the specific response was different for each type of biochar. In addition, an increase of electrolyte concentration decreased the peak relaxation time τ_{peak} for samples containing the biochars PW700, PW800, and BW550. It was concluded that the SIP response of biochars derived from the gasification and pyrolysis of wood (PW700, PW800 and BW550) resembled the response of porous media with disseminated conductors or semi-conductors, whereas the SIP response of the biochar HTC more closely resembled the SIP response of clay. Overall, SIP showed considerable sensitivity to biochar and its physical properties in soil.

The second sub-objective was to investigate whether available mechanistic models of induced polarization can be used to understand the relationship between biochar properties and the SIP response. In a first step, available models to describe the SIP response of porous media were reviewed in Chapter 2. It was highlighted that the polarizing processes for conductive and nonconductive materials are fundamentally different in the low-frequency range. In a next step, Chapter 5 explored the use of these mechanistic models to describe the SIP response of samples with amendments of the two types of biochar that showed a strong polarization in Chapter 4 (PW700 and PW800). Additional measurements on mixtures with PW700 were also presented in this chapter to investigate the importance of the type of electrolyte and possible redox reactions at the biochar surface. It was found that the Wong model was able to provide an adequate fit for samples with biochar PW700, which showed a stronger polarization that was attributed to a presumably larger electrical conductivity of the biochar. A slight influence of redox reactions on the SIP spectra was observed, and these changes were described to some extent by the Wong model. The Cole-Cole model was able to fit the SIP spectra of both types of biochar well. Using the parameters derived from fitting a Cole-Cole model, the Revil model was able to provide reasonable predictions of the volume fraction of biochar in sand-biochar mixtures and the diffusion coefficient of the charge carriers inside the biochar particles. It was concluded that both models were partially able to describe the SIP responses of biochar, which suggests that the polarization mechanism of biochar with strong polarization is similar to the electrode polarization of conductive or semi-conductive particles, but more complicated because of the physical and chemical properties. The results presented in this chapter support the notion that the electrical properties of the selected biochar play a key role in understanding the SIP response. It is also clear that these electrical properties are highly dependent on the production process of the biochar. Redox reactions at the surface of biochar may have a slight effect on the SIP response, but do not seem to be a key factor to understand the SIP response of soils with biochar.

The third and final sub-objective was to investigate how the SIP response of soil with biochar depends on saturation. For this, both pressure drainage and evaporative drying combined with SIP measurements were used to desaturate sand-biochar mixtures. The multistep-outflow (MSO) approach was used for pressure drainage of a pure sand sample and two sand-biochar mixtures with 1 and 2 % PW800 biochar. Analysis of the water retention characteristics obtained with MSO showed that the PW800 biochar was highly porous and rich in micropores and was able to enhance the water retention ability of soil to some degree. The measured SIP spectra as a function of saturation were interpreted by fitting a Cole-Cole model to obtain the total chargeability M, relaxation time τ_0 and Cole-Cole exponent c_{cc}. It was found that the porous nature of the biochar particles strongly affected the SIP response of the partially saturated sand-biochar mixtures. Due to the high residual water content of biochar in a relatively dry background, the relationship between bulk electrical conductivity and water saturation was nonlinear in a log-log representation. The strength of the polarization of the sand-biochar mixtures indicated by the M showed a nonlinear decrease with desaturation. This was attributed to the polarization strength of the drying biochar particles that continuously decreased, while that for the sand background first increased and then decreased during drainage. It was found that the τ_0 increased and the c_{cc} decreased with decreasing saturation. For the experiments using evaporative drying, a biochar made from pyrolysis of paper mill sludge (PS) was used. Six pairs of pure sand samples and sand-biochar samples with different initial water saturation were prepared and allowed to evaporate while making time-lapse SIP measurements. It was found that the dependence of $\sigma'(\omega)$ on water saturation was consistent with Archie’s law, although the fitted model parameters have an apparent nature only because of changes in the pore water electrical conductivity due to evaporation. The dependence of $\sigma''(\omega)$ on water saturation was roughly linear. Both set of measurements showed that saturation has a strong effect on the SIP response of samples with biochar. However, the dependence of polarization of biochar on saturation is obviously different to that for pure sand. The results suggested that the electrical conductivity and the porous nature of biochar are the key factors for polarization of biochar under partially saturated conditions.

Overall, the work presented in this thesis demonstrates that it is possible to detect and characterise particles of biochar in a sand matrix by the SIP method. However, additional work is required to extend the presented results to successful field applications, which will be discussed in the thesis outlook together with other possible research avenues.

.

7.2 Outlook

The results presented in Chapter 4 and 6 generally confirm that there is a considerable contrast between the SIP response of sand and sand-biochar mixtures under saturated and unsaturated conditions. For biochars with relatively strong polarization such as PW700 and PW800, the maximum phase value for the 1% sand-biochar mixture is more than two times higher than for sand even at low water saturation. Revil et al. (2015b) concluded that the signals of conductive particles and a weakly polarizing background are additive. Therefore, it is expected that field SIP imaging of the complex conductivity distribution allows a qualitative distinction of soil with and without biochar. This may already be useful to evaluate depth and homogeneity of biochar application in field studies. For a more quantitative use of SIP measurements for assessing the spatial variability of biochar amendments, an important question is whether variations in biochar amount can be distinguished in the presence of variability in water saturation. In general, the water saturation of agricultural soils is in a range between 20 and 70%. The results in Chapter 6 showed that with applied amounts of 1 and 2% PW800 biochar, the sand-biochar mixtures had a stronger polarization in a large range of saturation even for a relatively low saturation of 25% compared with pure sand. In addition, the observed phase values for the unsaturated sand-biochar mixtures (i.e., above 15 and 20 mrad, respectively, even for relatively dry mixtures in the millihertz to hertz frequency range) were considerably higher than the phase values observed for unsaturated soils in other studies, which typically reported phase values below 10 mrad in this low frequency range (e.g. Ghorbani et al., 2008; Kelter et al., 2018). This provides confidence that biochar with similar properties as PW800 can also be detected in unsaturated soils at application rates of 20 to 50 t ha^{-1} (0.5-3 mass %, depending on the depth of mixing with soil) used in many field trials (Ding et al., 2016; Mukherjee and Lal, 2014). If the hydraulic and electrical properties of biochar can be characterized using laboratory investigations before the field application of biochar, it may also be possible to quantify the amount of biochar. For example, the sand-biochar mixtures investigated in this thesis showed a strong dependence of the relaxation time on the saturation but not on the amount of biochar, which potentially allows separation of these effects. This should be explored in more detail in future laboratory and field investigations.

As a next step, it seems prudent to perform laboratory measurements with more realistic soil materials, thus better mimicking field conditions. In this thesis, research was focused on sand-biochar mixtures. However, biochar amendments are used for a broader range of soil types. Therefore, future research should also focus on other soil materials, ideally from fields where biochar has been or will be applied. Although the results in this thesis indicate that the presence of biochar results in a significant SIP response when using a sandy host medium, this needs to be confirmed for more complex soil environments too. It would be interesting to conduct laboratory SIP measurements on soil-biochar mixtures using soil samples retrieved from farmland or forests where biochar was applied or naturally accumulated. Such measurements should then also be used to evaluate the performance of available model concepts to describe the SIP response of biochar in a more complex background with potentially stronger polarization than sand. The effect of saturation should also be investigated for these mixtures of biochar and soil.

Another obvious next step would be to perform field SIP measurement on agricultural sites with biochar amendments. Ideally, initial test sites should be selected where the type and amount of biochar application are known. At these sites, the investigation of the depth distribution of biochar would be interesting, also to investigate the possible migration of biochar in soil. To do this, measurements with different surface electrode arrangement or with electrode sticks can both be applied. To separate biochar and saturation effects on the SIP response, such experiments should be combined with real-time soil water content monitoring using in-situ sensors at selected locations.

To advance interpretation of the SIP response of samples with biochar, future studies should focus more on the determination of biochar properties. The results in this thesis highlighted that the dominant polarization mechanism varies with the physical and chemical properties of biochar, which in turn depend on the feedstock and production process. Electrode polarization was dominant for the investigated biochars with a significant electrical conductivity, while double layer polarization played a primary role for other types of biochar. To further support appropriate modelling of the SIP response of biochar, future research should consider an improved characterization of biochar properties, such the electrical conductivity, the specific capacity, and the surface functional groups which are all known to influence the SIP response of soil with biochar. However, this is associated with a range of challenges. For example, the direct measurement of the electrical conductivity of biochar particles is challenging due to high contact resistances associated with the rough surface of the particle. The inner porosity and the anisotropy of the skeletal structure of biochar should also be considered to determine the electrical conductivity. For the determination of the electrical conductivity of multi-particle biochar samples (e.g. a bulk of biochar powders), electrical conductivity measurements depend on the pressure that is exerted on the sample by the measuring electrode due to the changing arrangement of biochar particles with increasing pressure, which results in changes of the void space (porosity) as well the contact areas between particles and thus the conducting pathway. This change also depends on the particle shape and size distribution and may not be quantitatively comparable for different biochars. To address these problems for a single biochar particle, the method of Gabhi et al. (2017) may be promising. In this method, the resistance of several uniform cylindrical biochar samples of different length is determined. The electrical conductivity was obtained from the slope of the roughly linear length-resistance relationship, rather than from the direct measurement on a single piece. The anisotropy of the electrical properties due to the inner structure of the biochar should also be specifically investigated. In the case of multi-particle samples, Tomasik et al. (2019) used a compacted tablet of biochar powder to enable measurement of the electrical properties, which showed some advantages. Alternatively, it may be possible to predict the electrical conductivity of biochar from the type and properties of feedstock and the parameters of the production procedure. Ippolito et al. (2020) showed the possibility to predict nutrient availability of biochar by meta-data analysis. However, this method certainly needs a broad database of direct measurements on electrical properties of biochar, which should be established in future studies.

Finally, the results in this study phenomenologically illustrated the dependence of the complex electrical conductivity of sand and sand-biochar mixtures on saturation. However, there is still a lack of understanding concerning the mechanistic principles that determine the SIP response of unsaturated porous media, even in the absence of porous biochar particles. This has been an open question for the past decade, and urgently needs to be addressed to establish SIP as a tool for vadose zone investigations. Along the same lines, mechanistic models for the polarization of disseminated conductive particles also need to be improved, since available models are not adequate to quantitatively describe the polarization in the complex case of drainable biochar particles in a polarizing background medium. Pore network models such as those proposed by Maineult et al. (2018) may be a promising forward to address these challenges. However, this would require suitable models to describe the polarization of single pores in a conductive particle, which are currently not available. To support such theoretical developments, there is a clear need to increase the database of SIP measurements on partially saturated porous media with and without addition of biochar and conductive particles.

References

Aal, G. A., Atekwana, E. A., and Werkema, D. D., 2017, Complex conductivity response to silver nanoparticles in partially saturated sand columns: Journal of Applied Geophysics, v. 137, p. 73-81.

Abdulsamad, F., Florsch, N., and Camerlynck, C., 2017, Spectral induced polarization in a sandy medium containing semiconductor materials: experimental results and numerical modelling of the polarization mechanism: Near Surface Geophysics, v. 15, no. 6, p. 669-683.

Agegnehu, G., Srivastava, A. K., and Bird, M. I., 2017, The role of biochar and biochar-compost in improving soil quality and crop performance: a review: Applied Soil Ecology, v. 119, p. 156-170.

Alvarez, R., 1973, Complex dielectric permittivity in rocks: a method for its measurement and analysis: Geophysics, v. 38, no. 5, p. 920-940.

Amoakwah, E., Frimpong, K. A., Okae-Anti, D., and Arthur, E., 2017, Soil water retention, air flow and pore structure characteristics after corn cob biochar application to a tropical sandy loam: Geoderma, v. 307, no. Supplement C, p. 189-197.

Angoran, Y., 1977, Induced polarization: a preliminary study of its chemical basis: Geophysics, v. 42, p. 788-803.

Archie, G. E., 1942, The electrical resistivity log as an aid in determining some reservoir characteristics: Transactions of the American Institute of Mining and Metallurgical Engineers, v. 146, p. 54-62.

Arthur, E., and Ahmed, F., 2017, Rice straw biochar affects water retention and air movement in a sand-textured tropical soil: Archives of Agronomy and Soil Science, v. 63, no. 14, p. 2035-2047.

Attwa, M., and Guenther, T., 2013, Spectral induced polarization measurements for predicting the hydraulic conductivity in sandy aquifers: Hydrology and Earth System Sciences, v. 17, no. 10, p. 4079-4094.

Bücker, M., and Hördt, A., 2013a, Analytical modelling of membrane polarization with explicit parametrization of pore radii and the electrical double layer: Geophysical Journal International, v. 194, no. 2, p. 804-813.

Bücker, M., and Hördt, A., 2013b, Long and short narrow pore models for membrane polarization: Geophysics, v. 78, no. 6, p. E299-E314.

Bücker, M., Orozco, A. F., and Kemna, A., 2018, Electrochemical polarization around metallic particles — Part 1: The role of diffuse-layer and volume-diffusion relaxation: Geophysics, v. 83, no. 4, p. E203-E217.

Bücker, M., Undorf, S., Flores Orozco, A., and Kemna, A., 2019, Electrochemical polarization around metallic particles — Part 2: The role of diffuse surface charge: Geophysics, v. 84, p. E57.

Börner, F. D., Schopper, J. R., and Weller, A., 1996, Evaluation of transport and storage properties in the soil and groundwater zone from induced polarization measurements: Geophysical Prospecting, v. 44, no. 4, p. 583-601.

Bai, M., Wilske, B., Buegger, F., Bruun, E. W., Bach, M., Frede, H. G., and Breuer, L., 2014, Biodegradation measurements confirm the predictive value of the O:C-ratio for biochar recalcitrance: Journal of Plant Nutrition and Soil Science, v. 177, no. 4, p. 633-637.

Bechtold, M., Vanderborght, J., Weihermuller, L., Herbst, M., Günther, T., Ippisch, O., Kasteel, R., and Vereecken, H., 2012, Upward transport in a three-dimensional heterogeneous laboratory soil under evaporation conditions: Vadose Zone Journal, v. 11, no. 2, p. 21.

Beck, A. E., 1981, Physical principles of exploration methods, Macmillan International Higher Education.

Ben Ishai, P., Talary, M. S., Caduff, A., Levy, E., and Feldman, Y., 2013, Electrode polarization in dielectric measurements: a review: Measurement Science and Technology, v. 24, no. 10, p. 21.

Bikbulatova, S., Tahmasebi, A., Zhang, Z., Rish, S. K., and Yu, J., 2018, Understanding water retention behavior and mechanism in bio-char: Fuel Processing Technology, v. 169, no. Supplement C, p. 101-111.

Biniak, S., Świątkowski, A., and Pakula, M., 2001, Electrochemical studies of phenomena at active carbon-electrolyte solution interfaces, *in* Radovic, L. R., ed., Chemistry and Physics of Carbon, Vol 27, Volume 27: New York, Marcel Dekker, p. 125-225.

Binley, A., Kruschwitz, S., Lesmes, D., and Kettridge, N., 2010, Exploiting the temperature effects on low frequency electrical spectra of sandstone: a comparison of effective diffusion path lengths: Geophysics, v. 75, no. 6, p. A43-A46.

Binley, A., Slater, L. D., Fukes, M., and Cassiani, G., 2005, Relationship between spectral induced polarization and hydraulic properties of saturated and unsaturated sandstone: Water Resources Research, v. 41, no. 12, p. 13.

Bockris, J. O., and Reddy, A. k. N., 1973, Modern electrochemistry, Boston, MA, Springer.

Borchard, N., Ladd, B., Eschemann, S., Hegenberg, D., Moseler, B. M., and Amelung, W., 2014, Black carbon and soil properties at historical charcoal production sites in Germany: Geoderma, v. 232, p. 236-242.

Breede, K., Kemna, A., Esser, O., Zimmermann, E., Vereecken, H., and Huisman, J. A., 2011, Joint measurement setup for determining spectral induced polarization and soil hydraulic properties: Vadose Zone Journal, v. 10, no. 2, p. 716-726.

Breede, K., Kemna, A., Esser, O., Zimmermann, E., Vereecken, H., and Huisman, J. A., 2012, Spectral induced polarization measurements on variably saturated sand-clay mixtures: Near Surface Geophysics, v. 10, no. 6, p. 479-489.

Brewer, C. E., Chuang, V. J., Masiello, C. A., Gonnermann, H., Gao, X. D., Dugan, B., Driver, L. E., Panzacchi, P., Zygourakis, K., and Davies, C. A., 2014, New approaches to measuring biochar density and porosity: Biomass & Bioenergy, v. 66, p. 176-185.

Bruggeman, D. A. G., 1935, Berechnung verschiedener Konstanten von heterogenen Substanzen: I. Dielectrizitatskonstanten und Leifahigkeiten der Mischkorper aus isotropen Substanzen: Ann. Phys, v. 24, p. 636-679.

Butnan, S., Deenik, J. L., Toomsan, B., Antal, M. J., and Vityakon, P., 2015, Biochar characteristics and application rates affecting corn growth and properties of soils contrasting in texture and mineralogy: Geoderma, v. 237, p. 105-116.

Chan, K. Y., Van Zwieten, L., Meszaros, I., Downie, A., and Joseph, S., 2007, Agronomic values of greenwaste biochar as a soil amendment: Australian Journal of Soil Research, v. 45, no. 8, p. 629-634.

Chan, K. Y., Van Zwieten, L., Meszaros, I., Downie, A., and Joseph, S., 2008, Using poultry litter biochars as soil amendments: Australian Journal of Soil Research, v. 46, no. 5, p. 437-444.

Cheng, C. H., Lin, T. P., Lehmann, J., Fang, L. J., Yang, Y. W., Menyailo, O. V., Chang, K. H., and Lai, J. S., 2014, Sorption properties for black carbon (wood char) after long term exposure in soils: Organic Geochemistry, v. 70, p. 53-61.

Chew, W., and Sen, P., 1982, Dielectric enhancement due to electrochemical double layer: thin double layer approximation: The Journal of Chemical Physics, v. 77, no. 9, p. 4683-4693.

Cole, K. S., and Cole, R. H., 1941, Dispersion and absorption in dielectrics I. Alternating current characteristics: The Journal of Chemical Physics, v. 9, no. 4, p. 341-351.

de Lima, O. A. L., and Sharma, M. M., 1992, A generalized Maxwell-Wagner theory for membrane polarization in shaly sands: Geophysics, v. 57, no. 3, p. 431-440.

Debye, P., 1929, Polar molecules, Dover publications.

Debye, P., and Hückel, E., 1923, Zur theorie der Elektrolyte. I. Gefrierpunktserniedrigung und verwandte Erscheinungen (The theory of electrolytes: I. Lowering of freezing point and related phenomena): Phys. Z, v. 24, p. 185-206.

Demirbas, A., Pehlivan, E., and Altun, T., 2006, Potential evolution of Turkish agricultural residues as bio-gas, bio-char and bio-oil sources: International Journal of Hydrogen Energy, v. 31, no. 5, p. 613-620.

Deng, H., Yu, H. M., Chen, M., and Ge, C. J., 2014, Sorption of atrazine in tropical soil by biochar prepared from cassava waste: Bioresources, v. 9, no. 4, p. 6627-6643.

Ding, Y., Liu, Y., Liu, S., Li, Z., Tan, X., Huang, X., Zeng, G., Zhou, L., and Zheng, B., 2016, Biochar to improve soil fertility: a review: Agronomy for Sustainable

Development, v. 36, no. 2.

Dong, D., Yang, M., Wang, C., Wang, H. L., Li, Y., Luo, J. F., and Wu, W. X., 2013, Responses of methane emissions and rice yield to applications of biochar and straw in a paddy field: Journal of Soils and Sediments, v. 13, no. 8, p. 1450-1460.

Dukhin, S. S., Shilov, V. N., and Bikerman, J. J., 1974, Dielectric phenomena and double layer in disperse systems and polyelectrolytes: Journal of The Electrochemical Society, v. 121, no. 4, p. 154C.

Fang, X., Cai, Y., Liu, D., and Zhou, Y., 2018, A mercury intrusion porosimetry method for methane diffusivity and permeability evaluation in coals : A comparative analysis: Applied Sciences, v. 8, no. 6.

Fixman, M., 1980, Charged macromolecules in external fields. I. The sphere: Journal of Chemical Physics, v. 72, no. 9, p. 5177-5186.

Gabhi, R. S., Kirk, D. W., and Jia, C. Q., 2017, Preliminary investigation of electrical conductivity of monolithic biochar: Carbon, v. 116, p. 435-442.

Gaskin, J. W., Steiner, C., Harris, K., Das, K. C., and Bibens, B., 2008, Effect of low-temperature pyrolysis conditions on biochar for agricultural use: Transactions of the Asabe, v. 51, no. 6, p. 2061-2069.

Ghorbani, A., Cosenza, P., Ruy, S., Doussan, C., and Florsch, N., 2008, Non-invasive monitoring of water infiltration in a silty clay loam soil using spectral induced polarization: Water Resources Research, v. 44, no. 8, p. 18.

Głąb, T., Palmowska, J., Zaleski, T., and Gondek, K., 2016, Effect of biochar application on soil hydrological properties and physical quality of sandy soil: Geoderma, v. 281, p. 11-20.

Gouy, L. G., 1910, Sur la constitution de la charge électrique à la surface d'un électrolyte: Phys. Theor. Appl., v. 9, no. 1, p. 457-468.

Gouy, L. G., 1917, Sur la fonction électrocapillaire: Annales de Physique, v. 9, p. 129-184.

Gurin, G., Tarasov, A., Ilyin, Y., and Titov, K., 2013, Time domain spectral induced polarization of disseminated electronic conductors: Laboratory data analysis through the Debye decomposition approach: Journal of Applied Geophysics, v. 98, p. 44-53.

Gurin, G., Titov, K., Ilyin, Y., and Tarasov, A., 2015, Induced polarization of disseminated electronically conductive minerals: a semi-empirical model: Geophysical Journal International, v. 200, no. 3, p. 1555-1565.

Hördt, A., Bairlein, K., Bücker, M., and Stebner, H., 2017, Geometrical constraints for membrane polarization: Near Surface Geophysics, v. 15, no. 6, p. 579-592.

Hördt, A., Bairlein, K., Bielefeld, A., Bücker, M., Kuhn, E., Nordsiek, S., and Stebner, H., 2016, The dependence of induced polarization on fluid salinity and pH, studied with an extended model of membrane polarization: Journal of Applied Geophysics, v. 135, p. 408-417.

Hördt, A., Druiventak, A., Blaschek, R., Binot, F., Kemna, A., Kreye, P., and Zisser, N., 2009, Case histories of hydraulic conductivity estimation with induced polarization at the field scale: Near Surface Geophysics, v. 7, no. 5-6, p. 529-545.

Haegel, F.-H., Zimmermann, E., Jablonowski, N. D., Esser, O., Huisman, J. A., and Vereecken, H., Application of spectral induced polarization and electrical impedance tomography on mixtures of biochars and active carbons with sand, *in* Proceedings of the 25th symposium on the application of geophpysics to engineering and environmental problems, 2012, Volume 25, p. 586-597.

Haldar, S. K., 2018, Chapter 6 - exploration geophysics, Mineral exploration (second edition), Elsevier, p. 103-122.

Hanai, T., 1960, Theory of the dielectric dispersion due to the interfacial polarization and its application to emulsions: Kolloid-Zeitschrift, v. 171, no. 1, p. 23-31.

Helmholtz, H., 1853, On some laws of the distribution of electrical currents in material conductors with application to experiments in animal electricity: Poggend. Annals, v. 89, no. 211.

Hoffmann, V., Jung, D., Alhnidi, M. J., Mackle, L., and Kruse, A., 2020, Bio-based carbon materials from potato waste as electrode materials in supercapacitors: Energies, v. 13, no. 9, p. 2406.

Hoffmann, V., Rodriguez Correa, C., Sautter, D., Maringolo, E., and Kruse, A., 2019, Study of the electrical conductivity of biobased carbonaceous powder materials under moderate pressure for the application as electrode materials in energy storage technologies: Global Change Biology Bioenergy, v. 11, no. 1, p. 230-248.

Huisman, J. A., Zimmermann, E., Esser, O., Haegel, F. H., Treichel, A., and Vereecken, H., 2016, Evaluation of a novel correction procedure to remove electrode impedance effects from broadband SIP measurements: Journal of Applied Geophysics, v. 135, p. 466-473.

Huisman, J. A., Zimmermann, E., Haegel, F. H., Treichel, A., and Vereecken, H., Evaluation of a correction procedure to remove electrode contact impedance effects from broadband SIP measurements, *in* Proceedings 3. International workshop on induced polarization, 2014, Zentralinstitut für Elektronik.

Hunt, J., DuPonte, M., Sato, D., and Kawabata, A., 2010, The basics of biochar: A natural soil amendment: Soil Crop Management, v. 30, p. 1-6.

Hupfer, S., Martin, T., Weller, A., Günther, T., Kuhn, K., Ngninjio, V. D. N., and Noell, U., 2016, Polarization effects of unconsolidated sulphide-sand-mixtures: Journal of Applied Geophysics, v. 135, p. 456-465.

Inyang, M., Gao, B., Zimmerman, A., Zhou, Y., and Cao, X., 2015, Sorption and cosorption of lead and sulfapyridine on carbon nanotube-modified biochars: Environmental Science and Pollution Research, v. 22, no. 3, p. 1868-1876.

Ippolito, J. A., Cui, L., Kammann, C., Wrage-Mönnig, N., Estavillo, J. M., Fuertes-Mendizabal, T., Cayuela, M. L., Sigua, G., Novak, J., and Spokas, K., 2020, Feedstock choice, pyrolysis temperature and type influence biochar characteristics: A comprehensive meta-data analysis review: Biochar, v. 2, no. 4, p. 421-438.

Jiang, J. H., Zhang, L., Wang, X. Y., Holm, N., Rajagopalan, K., Chen, F. L., and Ma, S. G., 2013, Highly ordered macroporous woody biochar with ultra-high carbon content as supercapacitor electrodes: Electrochimica Acta, v. 113, p. 481-489.

Jindo, K., Mizumoto, H., Sawada, Y., Sanchez-Monedero, M. A., and Sonoki, T., 2014, Physical and chemical characterization of biochars derived from different agricultural residues: Biogeosciences, v. 11, no. 23, p. 6613-6621.

Jougnot, D., Ghorbani, A., Revil, A., Leroy, P., and Cosenza, P., 2010, Spectral induced polarization of partially saturated clay-rocks: a mechanistic approach: Geophysical Journal International, v. 180, no. 1, p. 210-224.

Joyce, R. A., Glaser, D. R., Werkema, D. D., and Atekwana, E. A., 2012, Spectral induced polarization response to nanoparticles in a saturated sand matrix: Journal of Applied Geophysics, v. 77, p. 63-71.

Kastening, B., Hahn, M., and Kremeskotter, J., 1994, The double-layer of activated carbon electrodes part 2. Charge-carries in the solid material: Journal of Electroanalytical Chemistry, v. 374, no. 1-2, p. 159-166.

Kastening, B., Hahn, M., Rabanus, B., Heins, M., and zumFelde, U., 1997, Electronic properties and double layer of activated carbon: Electrochimica Acta, v. 42, no. 18, p. 2789-2799.

Kastening, B., and Heins, M., 2005, Properties of electrolytes in the micropores of activated carbon: Electrochimica Acta, v. 50, no. 12, p. 2487-2498.

Kelter, M., Huisman, J. A., Zimmermann, E., Kemna, A., and Vereecken, H., 2015, Quantitative imaging of spectral electrical properties of variably saturated soil columns: Journal of Applied Geophysics, v. 123, p. 333-344.

Kelter, M., Huisman, J. A., Zimmermann, E., and Vereecken, H., 2018, Field evaluation of broadband spectral electrical imaging for soil and aquifer characterization: Journal of Applied Geophysics, v. 159, p. 484-496.

Kemna, A., Binley, A., Cassiani, G., Niederleithinger, E., Revil, A., Slater, L., Williams, K. H., Orozco, A. F., Haegel, F. H., Hordt, A., Kruschwitz, S., Leroux, V., Titov, K., and Zimmermann, E., 2012, An overview of the spectral induced polarization method for near-surface applications: Near Surface Geophysics, v. 10, no. 6, p. 453-468.

Kim, K. H., Kim, J. Y., Cho, T. S., and Choi, J. W., 2012, Influence of pyrolysis temperature on physicochemical properties of biochar obtained from the fast pyrolysis of pitch pine (pinus rigida): Bioresource Technology, v. 118, p. 158-162.

Klein, J. D., and Shuey, R. T., 1978, Nonlinear impedance of mineral-electrolyte interfaces: Part I, pyrite: Geophysics, v. 43, no. 6, p. 1222.

Kohlrausch, F., 1873, Ueber die elektromotorische Kraft sehr dünner Gasschichten auf Metallplatten: Annalen der Physik, v. 224, p. 143.

Kramers, H. A., La diffusion de la lumiere par les atomes, *in* Proceedings Atti Cong.

Intern. Fisica (Transactions of volta centenary congress) Como, 1927, Volume 2, p. 545-557.

Kronig, R. d. L., 1926, On the theory of dispersion of x-rays: Josa, v. 12, no. 6, p. 547-557.

Kuppusamy, S., Thavamani, P., Megharaj, M., Venkateswarlu, K., and Naidu, R., 2016, Agronomic and remedial benefits and risks of applying biochar to soil: Current knowledge and future research directions: Environment International, v. 87, p. 1-12.

Lehmann, J., Gaunt, J., and Rondon, M., 2006, Bio-char sequestration in terrestrial ecosystems – a review: Mitigation and Adaptation Strategies for Global Change, v. 11, no. 2, p. 403-427.

Lehmann, J., Rillig, M. C., Thies, J., Masiello, C. A., Hockaday, W. C., and Crowley, D., 2011, Biochar effects on soil biota - a review: Soil Biology and Biochemistry, v. 43, no. 9, p. 1812-1836.

Leroy, P., Li, S., Jougnot, D., Revil, A., and Wu, Y., 2017, Modelling the evolution of complex conductivity during calcite precipitation on glass beads: Geophysical Journal International, v. 209, no. 1, p. 123-140.

Leroy, P., and Revil, A., 2009, A mechanistic model for the spectral induced polarization of clay materials: Journal of Geophysical Research: Solid Earth, v. 114, no. B10.

Leroy, P., Revil, A., Kemna, A., Cosenza, P., and Ghorbani, A., 2008, Complex conductivity of water-saturated packs of glass beads: Journal of Colloid and Interface Science, v. 321, no. 1, p. 103-117.

Lesmes, D., Sturrock, J., and Frye, K., A physiochemical interpretation of the Cole - Cole dielectric model, *in* Proceedings environment and engineering geophysical society, 2000, p. 533-543.

Lesmes, D. P., and Frye, K. M., 2001, Influence of pore fluid chemistry on the complex conductivity and induced polarization responses of Berea sandstone: Journal of Geophysical Research-Solid Earth, v. 106, no. B3, p. 4079-4090.

Lesmes, D. P., and Morgan, F. D., 2001, Dielectric spectroscopy of sedimentary rocks: Journal of Geophysical Research-Solid Earth, v. 106, no. B7, p. 13329-13346.

Linde, N., Binley, A., Tryggvason, A., Pedersen, L. B., and Revil, A., 2006, Improved hydrogeophysical characterization using joint inversion of cross-hole electrical resistance and ground-penetrating radar traveltime data: Water Resources Research, v. 42, no. 12.

Liu, C., Liu, F., Ravnskov, S., Rubaek, G. H., Sun, Z., and Andersen, M. N., 2017, Impact of wood biochar and its interactions with mycorrhizal fungi, phosphorus fertilization and irrigation strategies on potato growth: Journal of Agronomy and Crop Science, v. 203, no. 2, p. 131-145.

Lu, S., and Zong, Y., 2018, Pore structure and environmental serves of biochars derived from different feedstocks and pyrolysis conditions: Environmental Science and Pollution Research, v. 25, no. 30, p. 30401-30409.

Luo, Y., and Zhang, G., 1998, Theory and application of spectral induced polarization, Tulsa, OK, USA, Society of Exploration Geophysicists.

MacDonald, J. R., Advances in electrochemistry, *in* Proceedings of the Robert A. Welch Foundation Conferences on chemical research. XXX, Houston, TX: Robert A Welch Foundation, 1986, p. 7-87.

Macdonald, J. R., and Johnson, W. B., 1987, Fundamentals of impedance spectroscopy, impedance spectroscopy: Emphasizing Solid Materials and Systems, Wiley, p. 1-26.

Mahan, M. K., Redman, J. D., and Strangway, D. W., 1986, Complex resistivity of synthetic sulfide bearing rocks: Geophysical Prospecting, v. 34, no. 5, p. 743-768.

Maineult, A., Jougnot, D., and Revil, A., 2018, Variations of petrophysical properties and spectral induced polarization in response to drainage and imbibition: a study on a correlated random tube network: Geophysical Journal International, v. 212, p. 1398-1411.

Marshall, D. J., and Madden, T. R., 1959, Induced polarization, a study of its causes: Geophysics, v. 24, no. 4, p. 790-816.

Maxwell, J. C., 1873, A treatise on electricity and magnetism, Conduction through heterogeneous media, Volume 1: Oxford, Clarendon Press.

Mendez, A., Gomez, A., Paz-Ferreiro, J., and Gasco, G., 2012, Effects of sewage sludge biochar on plant metal availability after application to a Mediterranean soil: Chemosphere, v. 89, no. 11, p. 1354-1359.

Misra, S., Torres-Verdin, C., Revil, A., Rasmus, J., and Homan, D., 2016, Interfacial polarization of disseminated conductive minerals in absence of redox-active species - Part 1: Mechanistic model and validation: Geophysics, v. 81, no. 2, p. E139-E157.

Mohammadi, A., Cowie, A., Mai, T. L. A., de la Rosa, R. A., Kristiansen, P., Brandao, M., and Joseph, S., 2016, Biochar use for climate-change mitigation in rice cropping systems: Journal of Cleaner Production, v. 116, p. 61-70.

Mukherjee, A., and Lal, R., 2014, The biochar dilemma: Soil Research $V 52, no. 3, p. 217-230.

Nelson, P. H., and Van Voorhis, G. D., 1983, Estimation of sulfide content from induced polarization data: Geophysics, v. 48, p. 62.

Nemati, M. R., Simard, F., Fortin, J. P., and Beaudoin, J., 2015, Potential use of biochar in growing media: Vadose Zone Journal, v. 14, no. 6.

Nordsiek, S., and Weller, A., 2008, A new approach to fitting induced-polarization spectra: Geophysics, v. 73, no. 6, p. F235-F245.

O'Konski, C. T., 1960, Electric properties of macromolecules. V. Theory of ionic polarization in polyelectrolytes: Journal of Physical Chemistry, v. 64, p. 605-619.

Ogawa, M., and Okimori, Y., 2010, Pioneering works in biochar research, Japan: Australian Journal of Soil Research, v. 48, no. 6-7, p. 489-500.

Ogbonnaya, U., and Semple, K. T., 2013, Impact of biochar on organic contaminants in soil: a tool for mitigating risk?: Agronomy, v. 3, no. 2, p. 349-375.

Okay, G., Leroy, P., Ghorbani, A., Cosenza, P., Camerlynck, C., Cabrera, J., Florsch, N., and Revil, A., 2014, Spectral induced polarization of clay-sand mixtures: experiments and modeling: Geophysics, v. 79, no. 6, p. E353-E375.

Okimori, Y., Ogawa, M., and Takahashi, F., 2003, Potential of CO_2 emission reductions by carbonizing biomass waste from industrial tree plantation in South Sumatra, Indonesia: Mitigation and Adaptation Strategies for Global Change, v. 8, no. 3, p. 261-280.

Pandolfo, A., and Hollenkamp, A., 2006, Carbon properties and their role in supercapacitors: Journal of Power Sources, v. 157, no. 1, p. 11-27.

Pereira, R. C., Arbestain, M. C., Sueiro, M. V., and Maciá-Agulló, J., 2015, Assessment of the surface chemistry of wood-derived biochars using wet chemistry, Fourier transform infrared spectroscopy and X-ray photoelectron spectroscopy: Soil Research, v. 53, no. 7, p. 753-762.

Personna, Y. R., Ntarlagiannis, D., Slater, L., Yee, N., O'Brien, M., and Hubbard, S., 2008, Spectral induced polarization and electrodic potential monitoring of microbially mediated iron sulfide transformations: Journal of Geophysical Research-Biogeosciences, v. 113, no. G2, p. 13.

Placencia-Gomez, E., Parviainen, A., Slater, L., and Leveinen, J., 2015, Spectral induced polarization (SIP) response of mine tailings: Journal of Contaminant Hydrology, v. 173, p. 8-24.

Placencia-Gomez, E., Slater, L., Ntarlagiannis, D., and Binley, A., 2013, Laboratory SIP signatures associated with oxidation of disseminated metal sulfides: Journal of Contaminant Hydrology, v. 148, p. 25-38.

Placencia-Gomez, E., and Slater, L. D., 2014, Electrochemical spectral induced polarization modeling of artificial sulfide-sand mixtures: Geophysics, v. 79, no. 6, p. EN91-EN106.

Placencia-Gomez, E., and Slater, L. D., 2016, On the pore water chemistry effect on spectral induced polarization measurements in the presence of pyrite: Journal of Applied Geophysics, v. 135, p. 474-485.

Revil, A., Aal, G. Z. A., Atekwana, E. A., Mao, D. Q., and Florsch, N., 2015a, Induced polarization response of porous media with metallic particles - Part 2: Comparison with a broad database of experimental data: Geophysics, v. 80, no. 5, p. D539-D552.

Revil, A., and Cosenza, P., 2010, Comment on "Generalized effective-medium theory of induced polarization" (Michael Zhdanov, 2008, Geophysics, 73, F197-F211): Geophysics, v. 75, no. 2, p. X7-X9.

Revil, A., and Florsch, N., 2010, Determination of permeability from spectral induced polarization in granular media: Geophysical Journal International, v. 181, no. 3, p. 1480-1498.

Revil, A., Florsch, N., and Mao, D. Q., 2015b, Induced polarization response of porous media with metallic particles - Part 1: A theory for disseminated semiconductors: Geophysics, v. 80, no. 5, p. D525-D538.

Revil, A., Karaoulis, M., Johnson, T., and Kemna, A., 2012a, Review: Some low-frequency electrical methods for subsurface characterization and monitoring in hydrogeology: Hydrogeology Journal, v. 20, no. 4, p. 617-658.

Revil, A., Koch, K., and Holliger, K., 2012b, Is it the grain size or the characteristic pore size that controls the induced polarization relaxation time of clean sands and sandstones?: Water Resources Research, v. 48, no. 5.

Salitra, G., Soffer, A., Eliad, L., Cohen, Y., and Aurbach, D., 2000, Carbon electrodes for double-layer capacitors - I. Relations between ion and pore dimensions: Journal of the Electrochemical Society, v. 147, no. 7, p. 2486-2493.

Sanroman, M. A., Lee, D. J., Khanal, S., and Ok, Y. S., 2017, Special issue on biochar: production, characterization and applications – beyond soil applications: Bioresource Technology, v. 246, no. Supplement C, p. 1.

Schiesser, W. E., 2017, Poisson–Nernst–Planck equations, Spline collocation methods for partial differential equations, John Wiley & Sons, p. 261-286.

Schlumberger, C., 1915, Process for determining the nature of the subsoil by the aid of electricity: US., 1,163,468 (priority: January 2, 1913).

Schlumberger, C., 1920, Étude sur la prospection électrique du sous-sol (Study on Underground Electrical Prospecting), Paris, France, Gauthier-Villars et Cie.

Schurr, J. M., 1964, On the theory of the dielectric dispersion of spherical colloidal particles in electrolyte solution: The Journal of Physical Chemistry, v. 68, no. 9, p. 2407-2413.

Schwan, H. P., and Ferris, C. D., 1968, Four-electrode null techniques for impedance measurement with high resolution: Review of Scientific Instruments, v. 39, no. 4, p. 481-485.

Schwarz, G., 1962, A theory of the low-frequency dielectric dispersion of colloidal particles in electrolyte solution: Journal of Physical Chemistry, v. 66, no. 12, p. 2636-2642.

Seigel, H., Nabighian, M., Parasnis, D. S., and Vozoff, K., 2007, The early history of the induced polarization method: The Leading Edge, v. 26, no. 3, p. 312-321.

Sen, P. N., 1997, Resistivity of partially saturated carbonate rocks with microporosity: Geophysics, v. 62, no. 2, p. 415-425.

Sen, P. N., Scala, C., and Cohen, M. H., 1981, A self-similar model for sedimentary rocks with application to the dielectric constant of fused glass beads: Geophysics, v. 46, no. 5, p. 781-795.

Sigmund, G., Hüffer, T., Hofmann, T., and Kah, M., 2017, Biochar total surface area and total pore volume determined by N_2 and CO_2 physisorption are strongly influenced by degassing temperature: Science of the Total Environment, v. 580, p. 770-775.

Šimůnek, J., Jarvis, N. J., van Genuchten, M. T., and Gardenas, A., 2003, Review and comparison of models for describing non-equilibrium and preferential flow and transport in the vadose zone: Journal of Hydrology, v. 272, no. 1-4, p. 14-35.

Singh, B., Singh, B. P., and Cowie, A. L., 2010, Characterisation and evaluation of biochars for their application as a soil amendment: Australian Journal of Soil Research, v. 48, no. 6-7, p. 516-525.

Slater, L., Ntarlagiannis, D., and Wishart, D., 2006, On the relationship between induced polarization and surface area in metal-sand and clay-sand mixtures: Geophysics, v. 71, no. 2, p. A1-A5.

Slater, L. D., and Glaser, D. R., 2003, Controls on induced polarization in sandy unconsolidated sediments and application to aquifer characterization: Geophysics, v. 68, no. 5, p. 1547-1558.

Sohi, S., Lopez-Capel, E., Krull, E., Bol, R., 2009, Biochar, climate change and soil: A review to guide future research, CSIRO Land and Water Science Report, Volume 5, p. 17-31.

Sombroek, W., 1966, Amazon soils, Pudoc Wageningen.

Stebner, H., Halisch, M., and Hördt, A., 2017, Simulation of membrane polarization of porous media with impedance networks: Near Surface Geophysics, v. 15, no. 6, p. 563-578.

Stern, O., 1924, Zur Theorie der elektrolytischen Doppelschicht, Volume 30, p. 508-516.

Tarasov, A., and Titov, K., 2013, On the use of the Cole–Cole equations in spectral induced polarization: Geophysical Journal International, v. 195, no. 1, p. 352-356.

Titov, K., Kemna, A., Tarasov, A., and Vereecken, H., 2004, Induced polarization of unsaturated sands determined through time domain measurements: Vadose Zone Journal, v. 3, no. 4, p. 1160-1168.

Titov, K., Komarov, V., Tarasov, V., and Levitski, A., 2002, Theoretical and experimental study of time domain-induced polarization in water-saturated sands: Journal of Applied Geophysics, v. 50, no. 4, p. 417-433.

Toll, J. S., 1956, Causality and the dispersion relation - logical foundations: Physical Review, v. 104, no. 6, p. 1760-1770.

Tomasik, M., Knaga, J., Juliszewski, T., Lis, S., and Szul, T., Analysis of selected electrical properties of biochar obtained by pyrolysis from energy plants, *in* Proceedings 2019 applications of electromagnetics in modern engineering and medicine (PTZE), 2019, IEEE, p. 246-249.

Tryon, E. H., 1948, Effect of charcoal on certain physical, chemical, and biological properties of forest soils: Ecological Monographs, v. 18, no. 1, p. 81-115.

Ulrich, C., and Slater, L. D., 2004, Induced polarization measurements on unsaturated, unconsolidated sands: Geophysics, v. 69, no. 3, p. 762-771.

Van Genuchten, M. T., 1980, A closed-form equation for predicting the hydraulic conductivity of unsaturated soil: Soil Science Society of America Journal, v. 44, no. 5, p. 892-898.

Van Zwieten, L., Kimber, S., Morris, S., Chan, K. Y., Downie, A., Rust, J., Joseph, S., and Cowie, A., 2010, Effects of biochar from slow pyrolysis of papermill waste on agronomic performance and soil fertility: Plant and Soil, v. 327, no. 1-2, p. 235-246.

Vanhala, H., and Soininen, H., 1995, Laboratory technique for measurement of spectral induced polarization response of soil sampies 1: Geophysical prospecting, v. 43, no. 5, p. 655-676.

Vinegar, H. J., and Waxman, M. H., 1984, Induced polarization of shaly sands: Geophysics, v. 49, no. 8, p. 1267-1287.

Vithanage, M., Rajapaksha, A. U., Tang, X. Y., Thiele-Bruhn, S., Kim, K. H., Lee, S. E., and Ok, Y. S., 2014, Sorption and transport of sulfamethazine in agricultural soils amended with invasive-plant-derived biochar: Journal of Environmental Management, v. 141, p. 95-103.

Volkmann, J., and Klitzsch, N., 2010, Frequency-dependent electric properties of microscale rock models for frequencies from one millihertz to ten kilohertz: Vadose Zone Journal, v. 9, no. 4, p. 858-870.

Wagner, K. W., 1914, Erklärung der dielektrischen Nachwirkungsvorgänge auf Grund Maxwellscher Vorstellungen: Archiv für Elektrotechnik, v. 2, no. 9, p. 371-387.

Wait, J., 1959, The variable-frequency method, Overvoltage research and geophysical applications: London, Pergamon Press, p. 29-49.

Warburg, E., 1899, Ueber das Verhalten sogenannter unpolarisirbarer Elektroden gegen Wechselstrom: Annalen der Physik, v. 303, no. 3, p. 493-499.

Ward, S. H., Sternberg, B. K., LaBrecque, D. J., and Poulton, M. M., 1995, Recommendations for IP research: The Leading Edge, v. 14, no. 4, p. 243-247.

Weigand, M., and Kemna, A., 2016a, Debye decomposition of time-lapse spectral induced polarisation data: Computers & Geosciences, v. 86, p. 34-45.

Weigand, M., and Kemna, A., 2016b, Relationship between Cole-Cole model parameters and spectral decomposition parameters derived from SIP data: Geophysical Journal International, v. 205, no. 3, p. 1414-1419.

Weller, A., Breede, K., Slater, L., and Nordsiek, S., 2011, Effect of changing water salinity on complex conductivity spectra of sandstones: Geophysics, v. 76, no. 5, p. F315-F327.

Weller, A., Slater, L., Binley, A., Nordsiek, S., and Xu, S., 2015a, Permeability prediction based on induced polarization: Insights from measurements on sandstone and unconsolidated samples spanning a wide permeability range: Geophysics, v. 80, no. 2, p. D161-D173.

Weller, A., Slater, L., Huisman, J. A., Esser, O., and Haegel, F. H., 2015b, On the specific polarizability of sands and sand-clay mixtures: Geophysics, v. 80, no. 3, p. A57-A61.

Weller, A., Slater, L., Nordsiek, S., and Ntarlagiannis, D., 2010, On the estimation of specific surface per unit pore volume from induced polarization: A robust empirical relation fits multiple data sets: Geophysics, v. 75, no. 4, p. WA105-WA112.

Wong, J., 1979, Electrochemical model of the induced-polarization phenomenon in disseminated sulfide ores: Geophysics, v. 44, no. 7, p. 1245-1265.

Wong, J., and Strangway, D. W., 1981, Induced polarization in disseminated sulfide ores containing elongated mineralization: Geophysics, v. 46, no. 9, p. 1258-1268.

Woolf, D., Amonette, J. E., Street-Perrott, F. A., Lehmann, J., and Joseph, S., 2010, Sustainable biochar to mitigate global climate change: Nature Communications, v. 1, p. 9.

Xu, G., Lv, Y. C., Sun, J. N., Shao, H. B., and Wei, L. L., 2012, Recent advances in biochar applications in agricultural soils: benefits and environmental implications: Clean-Soil Air Water, v. 40, no. 10, p. 1093-1098.

Zhang, J., Chen, Q., and You, C. F., 2015, Numerical simulation of mass and heat transfer between biochar and sandy soil: International Journal of Heat and Mass Transfer, v. 91, p. 119-126.

Zhdanov, M., 2008, Generalized effective-medium theory of induced polarization: Geophysics, v. 73, no. 5, p. F197-F211.

Zheng, Q., and Wei, G.-W., 2011, Poisson–Boltzmann–Nernst–Planck model: The Journal of Chemical Physics, v. 134, no. 19, p. 194101.

Zimmermann, E., Kemna, A., Berwix, J., Glaas, W., Münch, H. M., and Huisman, J. A., 2008, A high-accuracy impedance spectrometer for measuring sediments with low polarizability: Measurement Science and Technology, v. 19, no. 10, p. 9.

Zisser, N., Kemna, A., and Nover, G., 2010, Relationship between low-frequency electrical properties and hydraulic permeability of low-permeability sandstones: Geophysics, v. 75, no. 3, p. E131-E141.

Band / Volume 581
Schlussbericht
Accelerating Low- carbon Industrial Growth through
CCUS (ALIGN-CCUS)
S. Weiske, S. Schemme, R. C. Samsun, R. Peters, S. Troy, S. Morgenthaler, D. Schumann, P. Zapp (2022), 216 pp
ISBN: 978-3-95806-632-8

Band / Volume 582
Closed Carbon Cycle Mobility –
Klimaneutrale Kraftstoffe für den Verkehr der Zukunft
F. Schorn, J. Häusler, J. L. Breuer, S. Weiske, J. Pasel, R. C. Samsun, R. Peters (2022), 220 pp
ISBN: 978-3-95806-636-6

Band / Volume 583
Machine learning for monitoring groundwater resources over Europe
Y. Ma (2022), viii, 125 pp
ISBN: 978-3-95806-638-0

Band / Volume 584
Mechanical properties of single and dual phase proton conducting membranes
W. Zhou (2022), IV, VI, 133 pp
ISBN: 978-3-95806-645-8

Band / Volume 585
Improvements to gravity wave physics from an observational perspective
M. Geldenhuys (2022), vii, 136 pp
ISBN: 978-3-95806-647-2

Band / Volume 586
Impact of severe convection on the water vapor mixing ratio in the extra-tropical stratosphere
D. Khordakova (2022), ii, 136 pp
ISBN: 978-3-95806-648-9

Band / Volume 587
Effects of salt precipitation during evaporation on porosity and permeability of porous media
J. Piotrowski (2022), xxvii, 139 pp
ISBN: 978-3-95806-650-2

Band / Volume 588
IEK-14 Report 2022
Forschung für die Energiewende und den Wandel im Rheinischen Revier
B. Emonts (Hrsg.) (2022)
ISBN: 978-3-95806-652-6

Band / Volume 589
Oxidation of monoterpenes studied in atmospheric simulation chambers
L. L. Hantschke (2022), 188 pp
ISBN: 978-3-95806-653-3

Band / Volume 590
NiFe Layered Double Hydroxide Catalysts for Oxygen Evolution Reaction in Alkaline Water Electrolysis
W. Jiang (2022), 165 pp
ISBN: 978-3-95806-658-8

Band / Volume 591
Optimizing Cross-linked Infrastructure for Future Energy Systems
L. Welder (2022), xxiii, 360 pp
ISBN: 978-3-95806-659-5

Band / Volume 592
Evaluation von Reaktorkonzepten für die CO_2-basierte Methanolsynthese aus Wasserstoff und Kohlendioxid mithilfe von CFD-Simulationen
S. Weiske (2022), x, 369 pp
ISBN: 978-3-95806-661-8

Band / Volume 593
Spectral Induced Polarization of Biochar in Soil
Z. Gao (2022), XXVI, 155 pp
ISBN: 978-3-95806-662-5

Weitere ***Schriften des Verlags im Forschungszentrum Jülich*** unter
http://wwwzb1.fz-juelich.de/verlagextern1/index.asp

Energie & Umwelt / Energy & Environment
Band / Volume 593
ISBN 978-3-95806-662-5

Mitglied der Helmholtz-Gemeinschaft

JÜLICH
Forschungszentrum